NNT : 2023AIXM0001

THÈSE DE DOCTORAT

Soutenue à Aix-Marseille Université
le 16 Septembre 2024 par

Ilias GOOVAERTS

The sources of cosmic reionisation : Evaluating the properties and contribution of faint star-forming galaxies

Discipline
Physique & Sciences de la Matière

Spécialité
Astrophysique et Cosmologie

École doctorale
Ecole Doctorale Physique et Sciences de la Matière ED352

Laboratoire/Partenaires de recherche
Laboratoire d'Astrophysique de Marseille (LAM)

Composition du jury

Françoise COMBES Observatoire de Paris	Rapportrice
Jarle BRINCHMANN Universidade do Porto	Rapporteur
Pascal OESCH Université de Genève	Examinateur
Laura PENTERICCI INAF	Examinatrice
Veronique BUAT LAM	Présidente du jury
Roser PELLO LAM	Directrice de thèse
Nicolas LAPORTE LAM	Invité
Denis BURGARELLA LAM	Invité

Affidavit

I, undersigned, Ilias Goovaerts, hereby declare that the work presented in this manuscript is my own work, carried out under the scientific supervision of Roser Pello, in accordance with the principles of honesty, integrity and responsibility inherent to the research mission. The research work and the writing of this manuscript have been carried out in compliance with both the french national charter for Research Integrity and the Aix-Marseille University charter on the fight against plagiarism.

This work has not been submitted previously either in this country or in another country in the same or in a similar version to any other examination body.

Marseille, 28/06/2023



This work is licensed under Creative Commons Attribution-NonCommercial-NoDerivatives 4.0 International Public License

List of publications and participation in conferences

List of publications :

1. *"Evolution of the Lyman-α-emitting fraction and UV properties of lensed star-forming galaxies in the range* $2.9 < z < 6.7$*"*, **Goovaerts, I.**, Pello, R., Thai, T. T., Tuan-Anh, P., Richard, J., Claeyssens, A., Carinos, E., de la Vieuville, G., Matthee, J. 2023, A&A, 678, A174

2. *"Galaxy main sequence and properties of low-mass Lyman-α emitters towards reionisation as viewed by VLT/MUSE and JWST/NIRCam"*, **Goovaerts, I.**, Pello, R., Burgarella, D., Thai, T. T., Richard, J., Claeyssens, A., Tuan-Anh, P., Arango-Toro, R. C., Boogaard, L., Contini, T., Guo, Y., Langan, I., Laporte, N., Maseda, M., 2024, A&A, 683, A184

3. *"Charting the Lyman-alpha escape fraction in the range 2.9<z<6.7 and consequences for the LAE reionisation contribution"*, **Goovaerts, I.**, Thai, T. T., Pello, R., Tuan-Anh, P., Laporte, N., Matthee, J., Nanayakkara, T., Pharo, J., 2024, A&A, 690, A302

4. *"Probing the faint-end luminosity function of Lyman-alpha emitters at* $3 < z < 7$ *behind 17 MUSE lensing clusters"*, Thai, T. T., Tuan-Anh, P., Pello, R., **Goovaerts, I.**, Richard, J., Claeyssens, A., Mahler, G., Lagattuta, D., de la Vieuville, G., Salvador-Solé, E., Garel, T., Bauer, F. E., Jeanneau, A., Clément, B., Matthee, J. 2023, A&A, 678, A139

5. *"Linking UV spectral properties of MUSE Lyα emitters at* $z \gtrsim 3$ *to Lyman continuum escape"*, Kramarenko, I. G., Kerutt, J., Verhamme, A., Oesch, P. A., Barrufet, L., Matthee, J., Kusakabe, H., **Goovaerts, I.**, Thai, T. T., 2024, MNRAS, 527, 9853

Participation in conferences and summer schools :

1. *"Characteristics of High Redshift Lensed Star Forming Galaxies, as seen by MUSE/VLT and HST"* (oral presentation)
   From Galaxies to Cosmology with Deep Spectroscopic Surveys
   Marseille, France | June 2022
2. **Euclid Summer School**
   Banyuls-sur-Mer, France | August 2022

3. *"Evolution of the Lyman-α emitting fraction and UV properties of lensed star-forming galaxies between* $2.9 < z < 6.7$*"* (oral presentation)
   Shedding new light on the first billion years of the Universe
   Marseille, France | June 2023
4. **IMPRS Summer School : Unraveling Galaxy evolution with JWST**
   Heidelberg, Germany | September 2023

5. *"Evolution of the Lyman-α emitting fraction and UV properties of lensed star-forming galaxies between* $2.9 < z < 6.7$*"* (oral presentation)
   SF2A 2023
   Strasbourg, France | June 2023
6. *"Faint star-forming galaxies towards the epoch of reionisation viewed with HST, JWST, and VLT/MUSE"* (oral presentation)
   Science with the Hubble and James Webb Space Telescopes VII : Stars, Gas & Dust in the Universe
   Porto, Portugal | May 2024
7. *"Faint star-forming galaxies towards the epoch of reionisation viewed with HST, JWST, and VLT/MUSE"* (oral presentation)
   SF2A 2024
   Marseille, France | June 2024

Résumé

La réionisation cosmique est la dernière transition de phase subie par l'Univers, entre $z \sim 12$ et $z \sim 6$, au cours de laquelle des photons UV ont ionisé l'hydrogène neutre dans le milieu intergalactique. L'exploration de l'évolution des galaxies à cette époque, rendue possible par le télescope spatial *Hubble* (HST), a été accélérée par l'arrivée sur le ciel du télescope spatial *James Webb* (JWST) en 2022. Le but de cette thèse est d'améliorer la caractérisation des galaxies intrinsèquement faibles, formant des étoiles, qui fournissent probablement la contribution dominante au processus de réionisation. La luminosité de ces galaxies faibles est bien au delà des limites d'observations des télescopes actuels, donc, pour leur détection et leur caractérisation, cette étude utilise la technique dite des télescopes gravitationnels, ainsi que des observations de la raie d'émission Lyman-α, la raie la plus brillante dans l'UV. Les observations VLT/MUSE des amas de galaxies sont combinées avec l'imagerie la plus profonde disponible du HST et du JWST pour créer des échantillons statistiquement significatifs d'émetteurs Lyman-α (LAE) et de galaxies sélectionnées dans l'UV. L'utilisation de l'IFU de MUSE permet la construction à l'aveugle d'échantillons de galaxies émettant la raie Lyman-α d'une part, et d'autre part de galaxies à cassure de Lyman, créant ainsi la vue la moins biaisée possible de ces populations. Les galaxies étudiées dans cette thèse ont des luminosités jusqu'à $L_{Ly\alpha} \sim 10^{39}$erg/s et des magnitudes UV jusqu'à $M_{UV} \sim -12$ dans la gamme de redshift $2.9 < z < 6.7$, sondant un régime très faible vers l'époque de la réionisation. Les propriétés de ces populations sont dérivées en utilisant la méthode d'ajustement de la Distribution Spectral en Energie (SED en anglais) et la raie Lyman-α, et comparées pour établir ce qui distingue la population sélectionnée par Lyman-α de la population générale sélectionnée en UV. Les taux de formation d'étoiles, les masses stellaires et les pentes UV sont dérivés et des corrélations sont établies avec les paramètres de la raie Lyman-α. La contribution de ces populations à la réionisation est également estimée de différentes manières, en commençant par l'estimation de la fraction de la population UV qui est sélectionnée comme LAE. L'évolution de cette quantité en fonction de l'intensité de l'émission Lyman-α et de la magnitude UV de la galaxie hôte est également explorée. La contribution de la population LAE à la réionisation est évaluée en utilisant les valeurs dérivées de la fraction d'échappement. Cette quantité est cruciale dans notre estimation des densités de taux de formation d'étoiles calculées à partir de la population LAE, ce qui nous permet d'obtenir une estimation éclairée de cette contribution. La contribution des LAE est nécessairement faible pour les petites valeurs de l'échappement des photons du Lyman continuum (<1%), mais potentiellement dominante pour les valeurs qui ont été observées dans les LAE à bas redshift et dans les analogues locaux à haut redshift (10%). De fortes hypothèses et incertitudes subsistent, soulignant le besoin d'observations supplémentaires de galaxies intrinsèquement faibles, observés derrière les amas de galaxies.

Mots-clés : Évolution des galaxies - Réionisation cosmique - Émetteurs Lyman-alpha - Lentillage gravitationnel : fort

Abstract

Cosmic reionisation is the last phase transition undergone by the Universe, between $z \sim 12$ and $z \sim 6$, at which time, energetic photons ionised the neutral hydrogen in the intergalactic medium. The exploration of galaxy evolution at this time, unlocked by the *Hubble* Space Telescope (HST) was thrust forward by the arrival on sky of the *James Webb* Space Telescope (JWST) in 2022.

The goal of this thesis is to improve the characterisation of the intrinsically faint, star-forming galaxies which likely provide the dominant contribution to the reionisation process. The luminosity of these galaxies is well beyond the reach of current instruments, therefore to detect and characterise them, this study makes use of gravitational telescopes as well as observations of the Lyman-α emission line, the brightest UV line. VLT/MUSE observations of lensing clusters are combined with the deepest available imaging from the HST and JWST to create statistically significant samples of Lyman-α Emitters (LAEs) and UV-selected galaxies. The use of MUSE's IFU enables the blind construction of samples of Lyman-α-emitting and UV-selected galaxies, creating the least biased view possible of these populations. The galaxies explored in this thesis have Lyman-α luminosities down to $L_{Ly\alpha} \sim 10^{39}$erg/s and UV magnitudes down to $M_{UV} \sim -12$ in the redshift range $2.9 < z < 6.7$, probing a very faint regime towards the epoch of reionisation.

The properties of these populations are derived using SED fitting and the Lyman-α line, and compared to establish what distinguishes the Lyman-α-selected population from the general, UV population. Star-formation rates, stellar masses and UV slopes are derived and correlations established with Lyman-α parameters, including luminosity, equivalent width, and escape fraction.

The contribution of these populations to reionisation is also estimated in a number of different ways, starting with tracing the fraction of the UV population that are selected as LAEs. The evolution of this quantity with the strength of Lyman-α emission and with UV magnitude of the host galaxy is also explored.

The contribution of the LAE population to reionisation is additionally assessed using the derived escape fraction values. This quantity is crucial in the assessment of the intrinsic star formation rate densities calculated from the LAE population, allowing us to derive an informed estimate of this contribution. The LAE contribution is found to be necessarily small for small values of the Lyman-continuum photon escape (<1%), but potentially dominant for values which have been observed in lower-redshift LAEs and local high-redshift analogues (10%). Strong assumptions and uncertainties remain, highlighting the need for further observations of lensed, intrinsically faint galaxies.

Keywords: Galaxy Evolution - Cosmic Reionisation - Lyman-alpha Emitters - Gravitational lensing: strong

Résumé Long

La réionisation cosmique est la deuxième (et dernière) phase de transition de l'Univers, qui débute lorsque les premières étoiles et galaxies ont commencé à réioniser le Milieu Intergalactique (IGM) neutre et se termine lorsque l'IGM est entièrement ionisé à un décalage spectral (ou *redshift* en anglais) de l'ordre de 6. Il est crucial d'étudier l'IGM et l'évolution des premières galaxies à cette époque, car c'est le point de départ de toute l'évolution des galaxies, aboutissant à l'Univers que nous connaissons aujourd'hui. L'observation des galaxies à cette époque est un défi et nécessite les télescopes spatiaux et terrestres les plus récents. À l'heure actuelle, la contribution exacte des sources ionisantes au processus de réionisation est encore débattue.
Cette thèse cherche à répondre à cette question, ainsi qu'à caractériser les galaxies formant des étoiles autour de l'Epoque de la Réionisation (EoR). Pour ce faire, elle se concentre sur les émetteurs Lyman-α (LAEs) ; des galaxies présentant la raie de recombinaison de l'hydrogène dans l'UV, intrinsèquement forte. En outre, ce travail tire parti des observations d'amas de galaxies jouant le rôle de lentilles gravitationnelles et, grâce à l'amplication de la lumière engendrée, cherche à étudier les populations de galaxies intrinsèquement faibles qui sont susceptibles d'avoir fourni la contribution dominante à la réionisation Finkelstein et al. (2015); Bouwens et al. (2015a).
Avec l'arrivée du télescope spatial *James Webb* en 2022, la recherche sur l'époque de la reionisation (EoR) s'est accélérée. La capacité du JWST à accéder au spectre infrarouge depuis l'espace, combinée à sa sensibilité et à sa résolution spatiale, a permis aux astronomes de détecter des galaxies à des redshifts extrêmement élevés, $z > 11$ (Harikane et al. 2023a; Robertson et al. 2023; Donnan et al. 2023; Curtis-Lake et al. 2023; Carniani et al. 2024), ainsi que l'émission optique dans le référentiel au repos des galaxies à redshift intermédiaire ($4 < z < 9$). Cela a facilité l'étude de la nature des galaxies à ces époques très précoces, ainsi que leur impact sur leur environnement. Les premières observations remettent en question nos modèles d'évolution cosmologique de l'Univers, nos hypothèses sur la formation des galaxies et des étoiles et sur la manière dont elles interagissent avec leur environnement (c'est-à-dire les milieux inter et circumgalactiques - IGM et CGM respectivement- voir Ferrara et al. 2023 et les références qui y figurent). Il est donc essentiel de poursuivre l'étude des galaxies précoces afin d'améliorer notre compréhension de la formation d'étoiles à cette époque ainsi que les modèles que nous utilisons pour comparer avec nos observations.
Cette thèse s'inscrit dans cette période dynamique pour l'astronomie à grand-redshift et a pour objectif de mieux comprendre la population des LAE, ainsi que la population générale des galaxies peu lumineuses, en train de former les étoiles, et leur impact sur la réionisation cosmique.
Pour atteindre ces objectifs, j'utilise des données provenant de trois observatoires : La spectroscopie IFU du Multi-Unit Spectroscopic Explorer (MUSE), au Very Large Teles-

cope (VLT) au Chili, ainsi que la photométrie des télescopes spatiaux : le *Hubble* Space Telescope (HST) et le JWST. La thèse se concentre sur les observations de galaxies situées derrière des amas de galaxies, afin de profiter de l'amplication de la lumière par la lentille pour accéder à des populations intrinsèquement faibles. Les amas de *Hubble* Frontier Fields (HFF, programme PI : J. Lotz, Lotz et al. 2017), bien étudiés, apparaissent donc comme des champs d'études idéaux, bénéficiant d'observations photométriques très profondes des télescopes spatiaux et d'une spectroscopie profonde de MUSE.
Cette thèse détaille trois travaux dans ce contexte, en commençant par une comparaison entre les LAE lentillés et les populations générales sélectionnées dans l'UV, y compris une analyse de la fraction LAE, $X_{\rm LAE}$, qui sonde la neutralité de l'IGM et, par conséquent, la progression de la réionisation. La deuxième étude se concentre sur la masse stellaire des LAEs, rendue accessible grâce aux données JWST/NIRCam, et compare une fois de plus la population LAE avec la population sélectionnée pour les UV afin d'évaluer leur contribution relative à la réionisation. La dernière partie de cette thèse se concentre sur la fraction d'échappement des photons Lyman-α, une quantité cruciale pour estimer leur impact sur l'IGM et la densité du taux de formation d'étoiles cosmiques (SFRD). La fraction d'échappement est dérivée pour un échantillon de LAEs individuels, et estimée de manière globale en comparant les deux fonctions de luminosité (LFs) de l'état de l'art, LAE et UV. Enfin, des perspectives sont proposées sur la base des travaux à venir et de l'état du domaine.
Les données utilisées pour ces études proviennent de l'instrument VLT/MUSE, un spectrographe à intégrale de champ, et de deux observatoires spatiaux, le HST et le JWST, qui fournissent la photométrie. L'utilisation de ces deux jeux de données nous permet de rechercher et d'étudier, pour la première fois, sans biais de sélection les populations de LAE et UV. La raie Lyman-α étant le plus souvent étendue, une partie de son flux n'est pas couvert par les spectrographes à fente standard. L'utilisation d'une unité de champ integral (IFU en anglais), telle que MUSE, nous permet de retrouver l'intégralité du flux de cette raie ainsi que son extension spatiale.
La spectroscopie MUSE utilisée dans cette thèse provient des observations GTO, en particulier du programme des amas de lentilles gravitationelles, présentés dans Richard et al. (2021) et Claeyssens et al. (2022), avec l'échantillon LAE décrit dans Claeyssens et al. (2022). MUSE peut détecter des LAE dans la gamme de redshift $2.9 < z < 6.7$. Il y a 17 amas de lentilles dans l'échantillon LLAMAS (Lensed Lyman-Alpha MUSE ARCS Sample en anglais) Claeyssens et al. (2022), dont quatre amas HFF sont utilisés dans les chapitres 3 et 4. Abell 2744 (A2744) est utilisé pour les estimations de masse stellaire dans le chapitre 3 et les estimations individuelles $f_{\rm esc,Ly\alpha}$ dans le chapitre 5. Finalement, les 17 amas sont utilisés pour l'étude de la fonction de luminosity (LF) des LAEs dans le chapitre 5. Dans A2744, il y a 121 LAE uniques, dans l'ensemble des amas HFF utilisés, il y en a 263 et dans l'échantillon complet de 17 amas, il y en a 600, tous avec des déterminations de redshift très fiables. La réduction des données MUSE est effectuée conformément à la prescription dans Weilbacher et al. (2020) et la détection des LAE suivie de l'extraction de leurs flux conformément aux descriptions dans Claeyssens et al. (2022) et Thai et al. (2023). Des systèmes d'images multiples sont identifiés et une image la plus représentative est choisie dans chaque cas, comme décrit dans Thai et al. (2023) et

Goovaerts et al. (2023).
La selection des galaxies UV dans les 17 amas utilisés est faite sur des images HST et JWST obtenues dans le cadre des programmes HFF et UNCOVER (Lotz et al. 2017; Bezanson et al. 2022). Les redshifts photométriques ont été calculés avec le package New-Hyperz (Bolzonella et al. 2000). Un ajustement SED plus détaillé, utilisé pour les estimations de la masse stellaire et de la formation stellaire corrigée de la poussière dans les chapitres 3 et 5 respectivement, a été réalisé à l'aide du package `CIGALE` (Boquien et al. 2019), en tirant parti des redshifts spectroscopiques disponibles pour les LAEs. Des modèles standards pour l'émission stellaire, l'atténuation de la poussière et l'histoire de la formation des étoiles sont utilisés (Calzetti et al. 2000; Bruzual &Charlot 2003; Theulé et al. 2024).
Ensuite, une fois la sélection en aveugle des deux populations effectuée, celles-ci ont été comparées et la meilleure image (la plus isolée, la moins contaminée) dans chaque système d'images multiples a été sélectionnée à l'aide du logiciel LENSTOOL Kneib et al. (1996); Jullo et al. (2007). Cette comparaison a permis de distinguer les propriétés des LAE parmi la population générale sélectionnée dans l'UV. La première section de cette thèse détaille cette analyse des propriétés relatives des deux populations, y compris les taux de formation d'étoiles (SFR), les pentes UV, les masses stellaires et leur corrélation avec la luminosité Lyman-α et la largeur équivalente ($\mathrm{EW_{Ly\alpha}}$). Cette sélection de populations révèle également des LAE détectés par MUSE qui ne sont pas détectés par HST. Ceci a déjà été remarqué par des études précédentes (Maseda et al. 2020a; de La Vieuville et al. 2020; Bacon et al. 2023). Ces objets sont difficiles à caractériser en raison du manque de données, mais des limites supérieures et inférieures sur les quantités physiques telles que la luminosité ou la masse stellaire sont fournies tout au long du travail lorsque cela est possible.
Les SFRs et les pentes UV sont dérivées de la photométrie HST des LAEs et des galaxies sélectionnées dans l'UV, et comparées aux paramètres Lyman-α tels que $\mathrm{EW_{Ly\alpha}}$. Grâce à plusieurs mesures, les résultats montrent que les LAEs faibles en UV permettent à une plus grande fraction de photons Lyman-α de s'échapper, probablement parce qu'il s'agit de galaxies de faible masse, jeunes, chimiquement non évoluées avec moins de poussière pour atténuer l'émission Lyman-α.
Les LAEs sont généralement distribués vers des SFR plus élevés et des pentes UV plus bleues, ce qui confirme la conclusion précédente sur la nature des LAEs par rapport à la population UV générale : ils ont tendance à être jeunes, à avoir des SFRs plus élevés et moins de poussière, bien que ces tendances soient observées avec une dispersion significative dans les objets individuels.

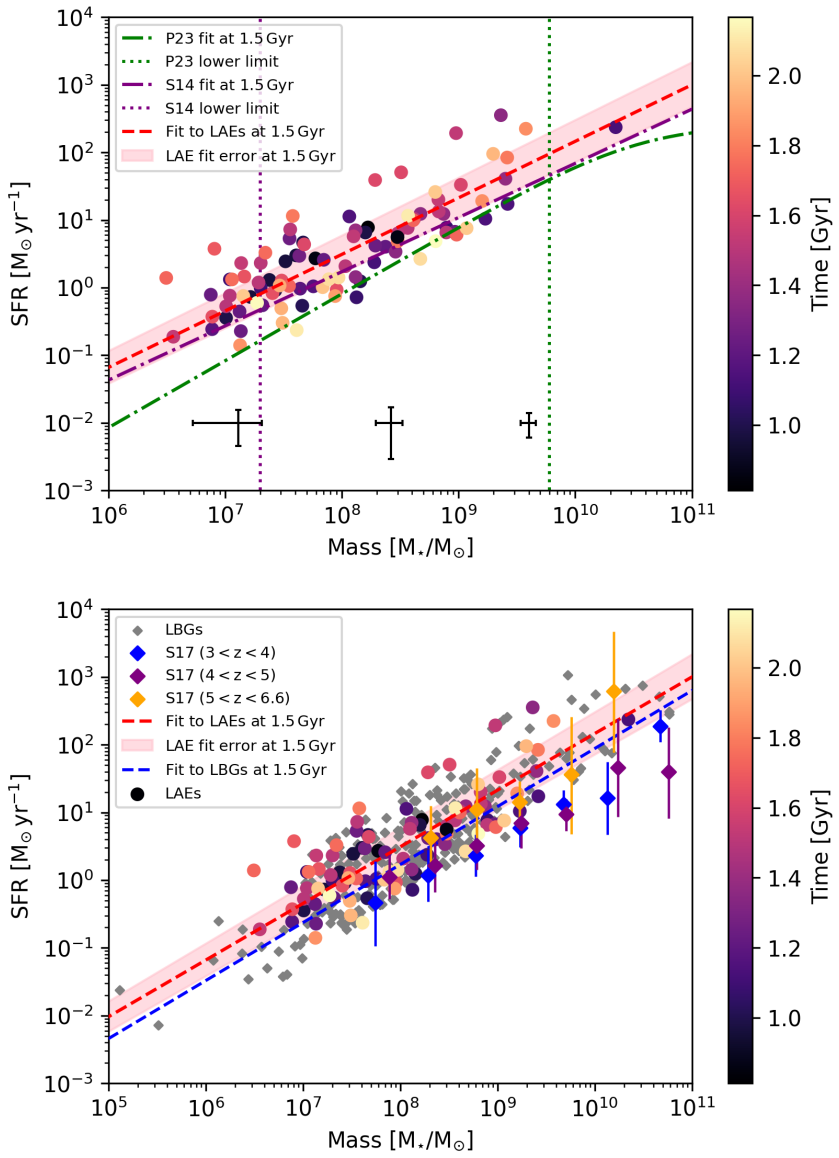

FIGURE 1 – Masse stellaire et SFR : la galaxie MS. *Panneau supérieur :* Les LAEs de notre échantillon final tracés sur la séquence principale des galaxies (MS) de formation d'étoiles, ainsi que les meilleurs ajustements aux données de Popesso et al. (2023), Speagle et al. (2014) et le meilleur ajustement aux LAEs. Les LAEs sont codés par une couleur en fonction du "Temps", en Gyr, qui est l'âge de l'Univers au redshift observé. La ligne violette en pointillés indique la limite de masse stellaire la plus faible de l'étude de Speagle et al. (2014) et la ligne verte en pointillés indique la limite de masse stellaire la plus faible de l'étude de Popesso et al. (2023).
Paneau inférieur : Les mêmes LAE avec le meilleur ajustement, comparés aux galaxies de même masse et de même redshift sélectionnées dans l'UV, avec le meilleur ajustement en bleu, et les résultats de Santini et al. (2017) regroupés par masse sous forme de diamants colorés avec des barres d'erreur.

Grâce à la photométrie du JWST/NIRCam et à l'étude UNCOVER dans l'amas de lentilles A2744 (Bezanson et al. 2022; Weaver et al. 2023), la partie optique au repos des LAEs peut, pour la première fois, être contrainte. Ceci nous permet de dériver des masses stellaires précises et de comparer ces résultats aux SFRs des galaxies. Les LAEs se situent au-dessus de la séquence principale de formation d'étoiles (MS) en utilisant des galaxies de masses plus élevées provenant de Speagle et al. (2014) et Popesso et al. (2023). La raison en est étudiée par comparaison avec des galaxies sélectionnées dans l'UV dans le même amas de lentilles aux mêmes redshifts et masses (voir les tracés supérieurs et inférieurs de la Fig. 1). Cela permet de déterminer si c'est la gamme de masse sondée par nos LAEs, ou la sélection par l'émission Lyman-α qui conduit à leur placement au-dessus des dérivations du MS provenant de la littérature. Il n'y a pas de différence statistique entre les LAEs et les LBGs, mais seulement entre les LAEs et les dérivations de la MS de la littérature, ce qui suggère que les galaxies de faible masse se situent généralement au-dessus de la MS, mais que les LAEs de faible masse ne se distinguent pas à cet égard. Ce résultat implique que si les galaxies de faible masse apportent probablement la contribution dominante à la réionisation, les LAEs ne sont pas plus importants que les LBGs dans ce processus.
Une faible corrélation de la masse stellaire avec la luminosité Lyman-α est également mise en évidence, et une corrélation plus forte avec la largeur équivalente de Lyman-α ($\mathrm{EW_{Ly\alpha}}$). Cela indique que les photons de Lyman-α ont plus de mal à s'échapper des galaxies de masse plus élevée, en accord avec les résultats obtenus en comparant la luminosité UV et l'$\mathrm{EW_{Ly\alpha}}$.
Dans le chapitre suivant, profitant du grand ensemble de données disponibles, non biaisées et sélectionnées en aveugle, j'évalue la progression de la réionisation en utilisant la fraction de galaxies sélectionnées dans l'UV qui sont également sélectionnées en tant que LAE, notée X_{LAE}. Cette quantité retrace la neutralité de l'IGM en utilisant l'atténuation de l'émission Lyman-α par l'hydrogène neutre au cours de la réionisation. Nous avons divisé notre échantillon en plusieurs populations : galaxies à cassure de Lyman (LBG : galaxies sélectionnées par leur cassure de Lyman dans l'UV) uniquement, LAE uniquement, LAE + LBG et LAE + continuum. L'échantillon LAE + continuum correspond aux LAEs pour lesquelles un continuum est observé, mais pour lesquelles ce continuum ne répond pas à nos critères de sélection pour notre échantillon LBG. La Fig. 2 montre les résultats tels qu'ils sont généralement présentés dans la littérature avec une limite $\mathrm{EW_{Ly\alpha}}$ de $25,\text{Å}$ et une limite de magnitude UV de $\mathrm{M_{UV}} > -20.25$. Les résultats dérivés dans ce travail sont en accord avec la littérature, malgré une dispersion significative à la fois dans ces résultats et dans d'autres, reflétant les différents types de relevés et les corrections d'incomplétude appliquées.
Ensuite, grâce à la taille de notre échantillon, il est possible d'étudier les différences entre les X_{LAE} dans les moitiés brillantes et faibles de notre échantillon, ainsi qu'avec et sans la limite de $\mathrm{EW_{Ly\alpha}}$. Avec la limite sur $\mathrm{EW_{Ly\alpha}}$ de $25,\text{Å}$, nous voyons peu de différence entre les moitiés brillantes et faibles de notre échantillon, mais, en rappelant que les LAEs brillants dans l'UV ont tendance à avoir des valeurs de $\mathrm{EW_{Ly\alpha}}$ plus petites, nous supprimons cette limite. Sans limite sur l'inclusion des LAEs dans l'échantillon, il y a une différence significative entre les échantillons lumineux et faibles. Nous observons des valeurs X_{LAE} plus importantes pour les objets brillants, particulièrement significatives dans les

tranches de redshift les plus élevées, vers l'époque de la réionisation. Cette population de galaxies brillantes dans l'UV, à faible $EW_{Ly\alpha}$, observée vers la réionisation, se reflète dans les premiers résultats des LAEs au sein de la réionisation du JWST (Witten et al. 2023; Witstok et al. 2023; Whitler et al. 2023b; Witstok et al. 2024). L'ensemble de ces résultats met en évidence une population de galaxies brillantes et massives qui ionisent des bulles de plus en plus importantes au fil du temps. Ces bulles ionisées permettent à l'émission Lyman-α de s'échapper, en se décalant vers le rouge hors de la résonance. Les galaxies faibles en UV n'auraient pas cette capacité, et c'est pourquoi cet échantillon présente une fraction plus faible de membres émettant du Lyman-α.
Le dernier chapitre de cette thèse se concentre sur la fraction d'échappement des photons Lyman-α, dénotée $f_{esc,Ly\alpha}$. Nous utilisons pour cela deux méthodes, une analyse de galaxies individuelles utilisant le SFR total dérivé de l'ajustement SED et une détermination globale utilisant les dernières fonctions de luminosité de Thai et al. (2023) (LAE) et de Bouwens et al. (2022) (UV).

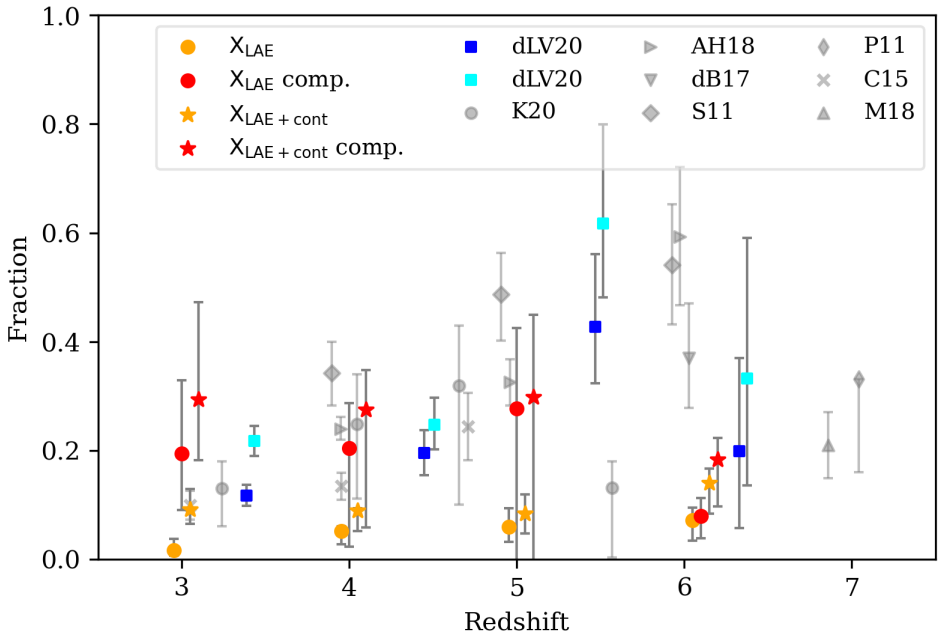

FIGURE 2 – Prévalence des LAEs dans la population de galaxies formant des étoiles, $X_{\rm LAE}$, sur un intervalle de redshift de 2.9 à 6, en considérant comme LAE les galaxies avec $EW_{Ly\alpha} > 25,$Å et $M_{1500} > -20,25$. Les cercles colorés représentent les $X_{\rm LAE}$ lorsque seuls les objets LAE+LBG sont considérés, et les étoiles colorées représentent le même calcul en incluant l'échantillon LAE+continuum. Les étoiles colorées indiquent ces valeurs $X_{\rm LAE}$ en incluant la correction de complétude LAE. Les résultats de la littérature sont inclus : Kusakabe et al. (2020), Arrabal Haro et al. (2018), De Barros et al. (2017), Stark et al. (2011), Pentericci et al. (2011), Cassata et al. (2015), et Mason et al. (2018b).

Notre analyse des galaxies individuelles est rendue possible par les nombreuses bandes photométriques fournies par le HST et le JWST dans l'amas de galaxies A2744. En utilisant l'ajustement de SED qui a déjà donné les estimations de masse stellaire montrées dans la Fig. 1, les SFRs corrigés pour l'extinction par la poussière sont dérivés et comparés au SFR calculé à partir de Lyman-α, ce qui donne $f_{esc,Ly\alpha}$.
Il n'y a pas d'évolution significative du redshift de $f_{esc,Ly\alpha}$ dans la gamme sondée par notre étude, bien que de meilleures statistiques puissent révéler une évolution vers $z \sim 6$. La médiane pour l'échantillon est 22.5%. D'autre part, une évolution plus significative est observée en fonction de la magnitude UV des galaxies. Nous avons ajusté cette évolution avec la relation $\log(f_{esc,Ly\alpha}) = (0.28 \pm 0.03)\, M_{UV} + (4.3 \pm 0.6)$. Ces résultats et l'ajustement sont présentés dans la Fig. 3. Cependant, il est probable que ces résultats soient affectés par l'incomplétude des données MUSE vers l'extrémité faible de notre échantillon, surtout pour $M_{UV} > -14$.

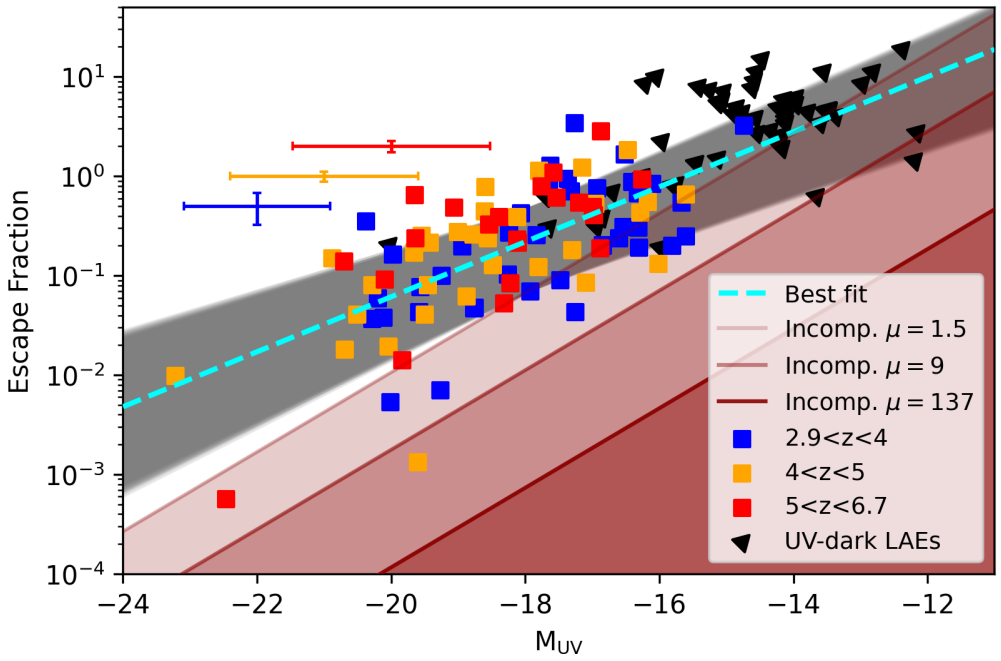

FIGURE 3 – L'évolution de $f_{esc,Ly\alpha}$ en fonction de la magnitude UV absolue M_{UV}. Les galaxies sont réparties en trois tranches de redshift pour souligner l'absence d'évolution dans ce sens, tandis que l'évolution avec M_{UV} est montrée par la relation en cyan. Les barres d'erreur médianes pour les trois tranches de redshift sont indiquées dans la couleur correspondante. Les valeurs des magnitudes absolues et leurs erreurs ont été corrigées de l'effet de lentillage gravitationnel. Les triangles noirs indiquent les LAEs dont le continuum n'est pas détecté. Les valeurs de M_{UV} pour ceux-ci sont des limites supérieures et les valeurs de la fraction d'échappement sont des limites inférieures. Ces objets sont exclus de l'ajustement. Les zones ombrées en rouge indiquent les régions incomplètes : une couleur plus foncée représente un effet croissant de magnification par la lentille gravitationnelle.

Le calcul de $f_{esc,Ly\alpha}$ à partir des fonctions de luminosités (LFs) LAE et UV nécessite la densité du taux de formation d'étoiles (SFRD), obtenue en intégrant les LFs. Nous prenons le rapport entre la SFRD provenant des LAE, dérivées dans Thai et al. (2023) et la SFRD calculé des LFs UV de Bouwens et al. (2022) avec les corrections de poussière de Bouwens et al. (2020). Une première comparaison avec les études précédentes de la littérature est effectuée, avec une limite d'intégration LF de $0.04L*$, où $L*$ est le paramètre de luminosité caractéristique de la fonction de Schechter. Cela nous permet de comparer aux échantillons plus lumineux provenant de la littérature et de faire la comparaison entre des limites d'intégration plus faibles et plus lumineuses. Dans les limites des incertitudes, on observe un bon accord avec les résultats des études précédentes utilisant la limite d'intégration plus lumineuse, cependant dans nos propres données nous voyons peu d'évolution entre $z = 3$ et $z = 5$ ($f_{esc,Ly\alpha} \approx 10\%$), et un saut à $z \sim 6$ ($f_{esc,Ly\alpha} \approx 30\%$).
Nous observons des fractions d'échappement plus élevées lorsque nous intégrons jusqu'à $0.0006L*$. À des redshifts entre 3 et 5, $f_{esc,Ly\alpha}$ est environ 15% et à $z = 6$, elle augmente jusqu'à environ 75%, et est cohérente à 1σ avec 100%. L'ajustement à toutes les données indique que $f_{esc,Ly\alpha}$ devient compatible avec 100% à $z \sim 8$. L'évolution d'$f_{esc,Ly\alpha}$ est plus significative lorsqu'elle est dérivée de cette manière, probablement en raison de la taille beaucoup plus importante de l'échantillon. De plus, $f_{esc,Ly\alpha}$ atteint des valeurs plus élevées que celles observées dans la littérature, ce qui est intéressant car ce sont les premiers résultats capables de sonder l'extrémité faible de la fonction de luminosité à laquelle nous intégrons ($0.0006L*$). Les résultats suggèrent que de grandes fractions de photons Lyman-α sont produites et s'échappent à des redshifts proches de la réionisation, probablement en raison de la forte formation d'étoiles et de la nature presque dépourvue de poussières de l'échantillon.
Ensuite, les valeurs dérivées de la fraction d'échappement sont utilisées pour calculer l'impact de la population de LAE sur la réionisation. Le nombre de photons ionisants calculé à l'aide de l'équation : $\dot{n}_{ion,Ly\alpha}(z) = \rho_{Ly\alpha}(z)\, \xi_{ion}^{Ly\alpha}\, f_{esc,LyC}$ est comparé au nombre total nécessaire à la réionisation de l'Univers à $z = 6$ (Bouwens et al. 2015b). $\rho_{Ly\alpha}(z)$ est le SFRD de la population des LAE, $\xi_{ion}^{Ly\alpha}$ est le facteur de conversion de la luminosité Lyman-α observée en nombre de photons ionisants et $f_{esc,LyC}$ est la fraction d'échappement au continuum de Lyman des LAE. Des scénarios différents en termes de $f_{esc,Ly\alpha}$ et $f_{esc,LyC}$ sont présentés. Lorsque $f_{esc,LyC}$ est petit ($< 1\%$), comme on le suppose pour la population générale des galaxies, la contribution des LAE à la réionisation doit être petite ($< 20\%$). Cependant, lorsque $f_{esc,LyC}$ est $\sim 10\%$, similaire aux valeurs qui ont été observées dans les LAE à faible redshift et dans les analogues à grand redshift, la contribution des LAE pourrait fournir tous les photons ionisants nécessaires pour maintenir la réionisation de l'Univers à $z = 6$.
En résumé, j'ai rassemblé le plus grand échantillon à ce jour de galaxies lentillées, sélectionnées dans l'UV et par la raie de Lyman-α, intrinsèquement faibles ($2.9 < z < 6.7$) afin d'évaluer leurs propriétés relatives, l'évolution de ces propriétés et leur impact sur la réionisation cosmique. J'ai étendu les tendances attendues pour la population LAE jusqu'aux luminosités très faibles, y compris l'anti-corrélation entre M_{UV}, la masse stellaire et $EW_{Ly\alpha}$. La localisation de l'échantillon de LAEs sur la séquence principale de formation stellaire a montré qu'il est probable qu'ils se situent au-dessus des dérivations typiques de

cette relation en raison de leur faible masse, plutôt que de leur sélection par l'émission $EW_{Ly\alpha}$. Enfin, j'ai étudié la fraction d'échappement des photons Lyman-α sur toute la gamme de redshifts couverts par MUSE, jusqu'à la fin de l'époque de la réionisation, et je n'ai pas trouvé d'évolution significative si l'on considère les galaxies individuellement. Cependant, une tendance à l'augmentation de $f_{esc,Ly\alpha}$ avec la diminution de M_{UV} était clairement présente dans les données. La comparaison des fonctions de luminosité pour dériver $f_{esc,Ly\alpha}$ montre une évolution avec le redshift, $f_{esc,Ly\alpha}$ devenant cohérente avec 100% autour de $z \sim 6$. Les conséquences pour la réionisation dépendent fortement de la valeur supposée de $f_{esc,LyC}$, les LAEs contribuant de manière mineure pour les petites valeurs ($f_{esc,LyC} < 1\%$) et de manière majeure pour les valeurs de $f_{esc,LyC}$ autour de 10%. La nécessité de poursuivre les observations dans les amas à lentille, en poussant à une plus grande statistique dans les régimes de masse les plus faibles, est soulignée. Le JWST nous offre l'opportunité de faire de grands progrès dans ce domaine dans les années à venir.

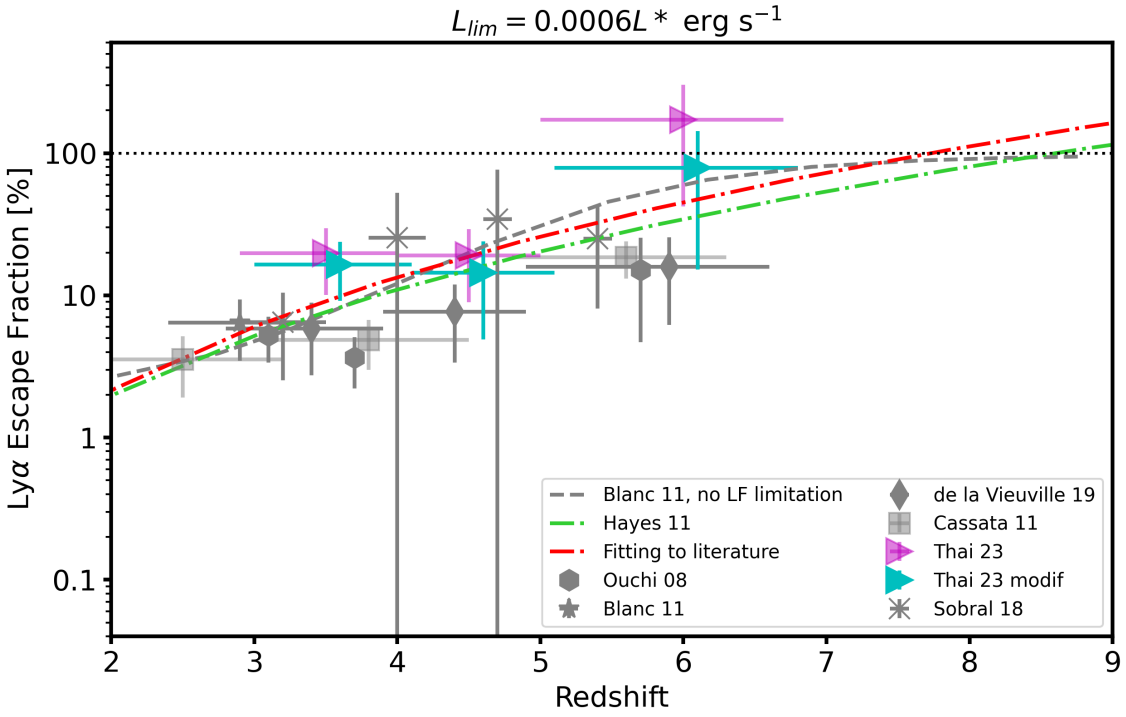

FIGURE 4 – Evolution globale avec le redshift de $f_{esc,Ly\alpha}$ avec une limite d'intégration sur les deux LF de $0.0006L*$. Les résultats de cette étude sont représentés par des points cyan (fonction de Schechter modifiée) et rose (fonction de Schechter générale). Les ajustements à la loi de puissance tirés de la littérature sont indiqués en gris et en vert ((B11), Hayes et al. (2011)) et l'ajustement équivalent à toutes les données est indiqué en rouge. L'ajustement de Hayes et al. (2011) est dérivé des résultats intégrés à $0,04L*$, et l'ajustement de B11 des résultats intégrés à 0.

Mots-clés : Évolution et formation des galaxies - Réionisation cosmique - Émetteurs Lyman-alpha - Lentillage gravitationnel : fort

Contents

Affidavit **2**

List of publications and participation in conferences **3**

Résumé **5**

Abstract **6**

Long résumé **7**

Contents **16**

List of Figures **18**

List of Tables **20**

1 Introduction **21**
1.1 Our Universe . . . 22
1.2 Reionisation and the first galaxies . . . 23
1.3 Galaxy evolution and observation . . . 26
1.4 Aside I : Lyman-α physics . . . 29
1.5 Aside II : Gravitational lensing . . . 35
1.6 Where are we now ? . . . 39

2 Data : VLT/MUSE, HST and JWST **42**
2.1 VLT/MUSE . . . 42
2.1.1 The LLAMA Sample . . . 42
2.2 HST photometry : HFF . . . 44
2.3 JWST photometry : UNCOVER . . . 46
2.4 Lens models and source magnifications . . . 47

3 Properties of high-redshift, gravitationally lensed, star-forming galaxies **49**
3.1 Introduction . . . 49
3.2 SED fitting and redshift estimation . . . 51
3.2.1 SED fitting with `CIGALE` . . . 55
3.3 Results : LAE properties . . . 59
3.3.1 Results : HST-derived properties . . . 59
3.3.2 Results : JWST-derived properties . . . 65
3.4 Discussion : implications for LAEs and reionisation . . . 71

4 Tracing reionisation with the Lyman-α-emitting fraction, X_{LAE} **73**
4.1 Introduction : X_{LAE} . . . 73
4.2 Evolution of X_{LAE} with redshift, $\mathrm{M_{UV}}$ and $\mathrm{EW_{Ly\alpha}}$ . . . 75
4.2.1 LAE Completeness . . . 75
4.2.2 Results : X_{LAE} . . . 76
4.3 Discussion : Implications for reionisation . . . 82

5 Charting the escape of Lyman-α photons in the range $2.9 < z < 6.7$ **85**
5.1 Introduction : Lyman-α escape . . . 85
5.2 Escape fraction of individual galaxies . . . 88
5.3 Global Escape fraction . . . 92
5.3.1 LAE and UV LFs . . . 93
5.3.2 Global Escape Fraction Results . . . 95
5.4 Discussion . . . 100
5.4.1 The global evolution of $\mathrm{f_{esc,Ly\alpha}}$ . . . 100
5.4.2 Comparison of the global and individual $\mathrm{f_{esc,Ly\alpha}}$ evolutions . . . 102
5.4.3 Overlap of the UV and LAE LFs . . . 104
5.4.4 The LAE contribution to reionisation . . . 106

6 Conclusions, prospects and the future of the field **111**
6.1 Summary and key results . . . 111
6.2 Perspectives and the near future . . . 113
6.2.1 UV-dark LAEs, observations and explanations . . . 115
6.2.2 CLASS and UV-morphology of LAEs . . . 120
6.3 Further in the future... . . . 121
6.4 Conclusions . . . 123

Acknowledgement **141**

List of Figures

1 SFR en fonctionne de masse stellaire . . . 10
2 Fraction des galaxies qui émettent du Lyman-α. . . . 12
3 L'évolution de $f_{esc,Ly\alpha}$ en fonction de la magnitude UV pour des LAEs . . 13
4 Evolution globale avec redshift de $f_{esc,Ly\alpha}$ avec une limite d'intégration sur les deux LF de $0.0006L*$ . . . 15

1.1 A lightcone from the Cosmic Dawn II (CoDa II) simulation . . . 25
1.2 A model of galaxy SED at $z = 7$. . . . 27
1.3 The diversity of the Lyman-α line shape. . . . 32
1.4 Gravitational lensing diagram . . . 35
1.5 Gravitational lensing schematic . . . 36
1.6 Critical curves and multiple images on the RXJ1347 lensing cluster. . . . 38

2.1 Redshift and magnitude distribution of 96 LAEs with JWST imaging. . . . 47

3.1 Photometric vs spectroscopic redshift comparison . . . 54
3.2 Redshift and M_{UV} distribution for the LAE and LBG samples . . . 54
3.3 SFH comparison in `CIGALE` fitting process . . . 57
3.4 `CIGALE` mock catalog galaxy parameter comparison. . . . 58
3.5 $EW_{Ly\alpha}$ distribution . . . 60
3.6 $EW_{Ly\alpha}$ vs M_{UV} . . . 61
3.7 UV slope vs $EW_{Ly\alpha}$ . . . 62
3.8 SFR comparison for LAE+LBG sample . . . 64
3.9 M_{UV} and SFR_{UV} vs UV slope . . . 65
3.10 Stellar mass vs Lyman-α parameters . . . 67
3.11 Stellar mass vs SFR : the galaxy MS . . . 70

4.1 M_{UV} and redshift distribution of LAE and LBG populations. . . . 76
4.2 LAE fraction . . . 79
4.3 LAE fraction with varying limits on M_{UV} and $EW_{Ly\alpha}$ . . . 81

5.1 Redshift evolution of $f_{esc,Ly\alpha}$ . . . 88
5.2 The evolution of $f_{esc,Ly\alpha}$ with absolute UV magnitude . . . 92
5.3 UV and LAE LFs on common scale of SFR. . . . 93
5.4 Global redshift evolution of $f_{esc,Ly\alpha}$ with an integration limit on both LFs of $0.04L*$. . . . 96
5.5 Global redshift evolution of $f_{esc,Ly\alpha}$ with an integration limit on both LFs of $0.0006L*$. . . . 97

5.6 Redshift and M_{UV} distribution of LAE and Lyman Break Galaxies (UV-selected galaxies, LBGs) from the sample in Goovaerts et al. (2023). . . . 104

6.1 1063z6 and 20744z4 shown on the $SFR_{Ly\alpha}$-SFR_{UV} plane. 117
6.2 Lyman-α contours of 1063z6 and 2744z4 on HST images. 118
6.3 HST, JWST/NIRCam and JWST/MIRI coverage. 119
6.4 Properties of the forthcoming MOSAIC instrument at the ELT 122

List of Tables

2.1 5σ limiting magnitudes of each filter for the four clusters. 45

3.1 Details of each lensing cluster used in this study. 52
3.2 Results for the galaxy MS from the literature and from this study. 71

5.1 UV SFRD used to calculate $f_{esc,Ly\alpha}$. 96
5.2 LAE luminosity density and its SFRD. 99
5.3 The LAE contribution to reionisation. 107

1 Introduction

I am fond of a quote from Zach Wienersmith, which hangs on a colleague's door : *"Aristotle said a bunch of stuff that was wrong. Galileo and Newton fixed things up. Then Einstein broke everything again. Now, we've basically got it all worked out, except for small stuff, big stuff, hot stuff, cold stuff, fast stuff, heavy stuff, dark stuff, turbulence, and the concept of time."*

— *Zach Wienersmith, Science : Abridged Beyond the Point of Usefulness*

Author's note on content : *This introduction is designed to situate readers in the context of my thesis work. I will begin at the beginning, naturally, and provide a whistle-stop tour of the history of the Universe from the Big Bang to the current day. I will then focus on the epoch of reionisation, what we know about it and what we can observe at these times. As we mainly trace this epoch using galaxies, I will describe what is known about galaxy evolution in and around reionisation, focusing on the main types of galaxies we observe, Lyman-α emitters and Lyman break galaxies. I include two specialised sections highly pertinent to the thesis work, the first on Lyman-α physics, transfer, escape and observables and the second on gravitational lensing, its formalism and why we use it to study the history of the Universe at this time. Finally I will address the state of the field, focusing on the open questions which inform and motivate the thesis work.*

Author's note on context : *During one's thesis, it is easy to develop tunnel vision. It is common to focus a great deal of attention of a small niche, and sometimes forget that said niche is part of a much bigger picture. Certainly, at points, this has been the case for me, so I thoroughly enjoyed reconnecting with the context of my work during the writing of this introduction. I hope readers find something they didn't know before, I certainly did, writing it. It's a good feeling.*

1.1 Our Universe

Our Universe began, by our best estimates, 13.8 billion years ago, with the Big Bang (Planck Collaboration et al. 2020). Shortly after (380,000 years after, which is short in the context of cosmology) the Universe cooled enough to undergo its first global phase transition, called recombination, when neutral hydrogen atoms first recombined from the primordial soup of protons, neutrons and electrons.
This phase transition heralded the start of what we commonly call the "Dark Ages", as there were no stars, or other sources of light. During this time the first dark matter haloes formed which later contained the first stars, and then the first galaxies. These stars formed at some time during the Dark Ages after the neutral hydrogen and trace other elements underwent gravitational collapse in the most overdense regions (at exactly which time this happened is the subject of ongoing investigation). These first stars and galaxies, the birth of which is called "Cosmic Dawn", then started to emit ionising radiation (photons with energy $> 13.6\,\mathrm{eV}$ and wavelength $\lambda < 912\,\text{Å}$), capable of reionising the neutral hydrogen in the Universe.
The Universe then underwent the last major phase transition in its history : reionisation. The neutral hydrogen in the inter-galactic medium (IGM : the material between all the galaxies) reionised, leaving ionised hydrogen (H^+) ; a process that was completed around $z = 6$, or 1 billion years after the Big Bang (Stark et al. 2010; McGreer et al. 2015; Planck Collaboration et al. 2020; Lu et al. 2022).
Galaxies have evolved and aged, and new stars and galaxies have been born, up until the present day. The density of the formation of these stars peaked at around $z = 2$, an epoch known as "Cosmic Noon" [1] (Madau et al. 1998; Madau &Dickinson 2014). The cosmic star formation rate density (SFRD) has declined since $z = 2$ until the present day.
Currently, we have observed more than a million galaxies spectroscopically [2] (Alam et al. 2015), from Andromeda, our closest galactic neighbour, to the furthest galaxy as yet observed at the time of writing : the galaxy with the catchy name JADES-GS-z13-0, which is at a spectroscopically confirmed redshift of 13.2 (Curtis-Lake et al. 2023; Robertson et al. 2023). I note that the use of as yet is important here, since the advent of the *James Webb* Space Telescope (JWST), the redshift record has been broken several times. When I was born, in 1998, the record was $z = 5.34$ (Dey et al. 1998). Today, most astronomers working on the early Universe would no longer even consider this to be high redshift. So, whether or not JADES-GS-z13-0 is still the highest redshift galaxy will likely entirely depend on when you are reading this.
In order to highlight a sense of the pace at which this area of physics is moving, I would like to stress that the previous paragraph was written in February of 2024, and the current paragraph in May of 2024, and the redshift record has just been broken once again with a claimed spectroscopic confirmation at $z = 14.3$, a galaxy named JADES-GS-z14-0. As of

1. I was once in a lecture by Alice Shapley, who suggested the use of "Cosmic Brunch", for the epoch around $z = 6$. I say why stop there, why not abbreviate to "Crunch". Certainly, I would find it satisfying to say : "It's Crunch time !"

2. We have observed many more with imaging. An exact number is at the same time difficult to estimate and not of much use. The reader should simply appreciate the amount and diversity of galaxies hitherto observed.

the time of writing, this has only been published on `arXiv` (Carniani et al. 2024).
We see all sorts of galaxies between Andromeda and JADES-GS-z13-0, spanning a great range of sizes, masses, ages and properties. We are still actively studying all these galaxies, at all redshifts, from regions in our own Milky Way and regions in nearby galaxies where we can resolve individual stars, to the furthest away galaxies, which we never see as more than a blob of pixels. All this forms part of an integrated and combined effort to further our understanding of galaxy evolution as a whole, starting from a galaxy's constituent parts, and ending with the galaxy population's impact on the Universe in a global sense.
In the next section we will zoom in on the focus of this thesis : galaxy evolution around the epoch of reionisation (EoR).

1.2 Reionisation and the first galaxies

We do not yet know when the first galaxies started to form during the Dark Ages. Our current best paradigm for the cosmological evolution of the Universe, the ΛCDM model[3], makes predictions for the evolution of the earliest galaxies (Planck Collaboration et al. 2016, 2020). However, this theory is being, and will continue to be, strongly tested by our ongoing observations with the JWST (Ferrara et al. 2023 provides a good review), but let us for now assume that a redshift of ~ 15 ($200 - 300$ Gyr after the Big Bang) (Donnan et al. 2024 provide tantalising clues that this may be the case) represents the starting point of galaxy evolution. The overdense regions of the Universe collapsed under their own gravitational pull, until the local density reached the point of nuclear fusion : hydrogen atoms fused to form helium, with energy as a by-product. The first stars formed in this way, and in the regions of great overdensity, groups of these stars together formed the first galaxies. We are not sure exactly what the properties of these first stars and galaxies were, as even with observations like that of JADES-GS-z14-0, we cannot surely say we are observing the very first galaxies. The hunt for a population of stars forming from pristine gas (hydrogen plus helium and traces of lithium and other light elements), called population III or pop-III stars, goes on (Schaerer &Pelló 2002; Schaerer 2007; Hartwig et al. 2018; Vanni et al. 2023; Zackrisson et al. 2023; Vanzella et al. 2023), but as yet no such populations have been confirmed, either in the local Universe, or in its furthest observable reaches.
So, what *do* we observe at these very early times ? What do these very early populations of galaxies look like ? What effect are they having on the Universe around them ? On reionisation ?
In general, galaxies at the earliest epochs are expected to be rare, poor in metals (due to having formed from pristine, or largely pristine, gas) and highly star-forming, due to large reserves of neutral hydrogen (Schaerer &de Barros 2010; Schaerer et al. 2022; Finkelstein et al. 2023; Robertson et al. 2023; Curti et al. 2023; Donnan et al. 2023; Morishita et al. 2024; Roberts-Borsani et al. 2024). Much of this is starting to see support by the deep

3. This is the standard model which has seen widespread success in the past few decades. Within it is contained information about the components of matter, dark and baryonic, a dark energy component (Λ) and information on the nature of dark matter (described as cold, in that it does not interract, with itself or with anything else other than gravitationally).

JWST surveys targeting the EoR : surveys such as JADES (Eisenstein et al. 2023, PI : D. Eisenstein,), CEERS (Finkelstein et al. 2022, PI : S. Finkelstein,), UNCOVER (Bezanson et al. 2022, PI : I. Labbé,) and GLASS (Treu et al. 2022, PI : T. Treu,).
With these surveys and others, we have started to enter a stage in astrophysics when we can probe the very first galaxies that formed in the Universe. Although this stage is still very new, many results have already come in from JWST, constraining the properties of galaxies at redshifts of 10 and above, which equates to times less than half a billion years after the Big Bang.
The initial results have pointed in many cases to an excess of galaxies at $z > 9$, particularly bright galaxies (see Ferrara et al. 2023 and references therein, as well as Donnan et al. 2023; Harikane et al. 2023a; Chemerynska et al. 2023; Harikane et al. 2024; Donnan et al. 2024). This overabundance of bright galaxies is especially troublesome when confronted with our models as bright, massive galaxies should take some significant time to build up, and therefore should not exist at these early times (in the numbers they are now being observed). Possible reasons for this discrepancy between observations and the ΛCDM model include differences in the initial mass function (IMF [4]) at these early times (Cameron et al. 2023; Lapi et al. 2024), overestimation of galaxy masses (Wang et al. 2024), feedback-free star formation (Dekel et al. 2023) very low dust content in these galaxies (Ferrara et al. 2023; Mauerhofer &Dayal 2023), stochastic star formation histories [5] (SFHs) (Whitler et al. 2023a; Ciesla et al. 2023; Mason et al. 2023) and a weaker UV background (which ionises and heats neutral hydrogen) (Harikane et al. 2023a). Contamination from lower-redshift interlopers could play a role (Arrabal Haro et al. 2023b; Fujimoto et al. 2023), but increasing numbers of these galaxies are being spectroscopically confirmed (e.g. Curtis-Lake et al. 2023; Arrabal Haro et al. 2023a; Atek et al. 2023) and we are noting that the agreement between the photometric predictions for these galaxies' redshifts and their eventual spectroscopic confirmations is strong in most cases. The contribution of AGN is still debated as well (Kokorev et al. 2023; Dayal et al. 2024), with their exact contribution and contamination in the results of the UV luminosity functions (LFs) as yet unclear.
Dust content of these galaxies is a critical unknown and could potentially resolve a significant part of the tension between observations and models. Despite the expectation that these early galaxies are all very dust-poor, a range of scenarios have been observed (Laporte et al. 2017; Reuter et al. 2020; Bouwens et al. 2022b) and the build up of heavy elements and dust in galaxies is not well understood within the EoR. Observations constraining dust content in the early universe (such as Naidu et al. 2022; Finkelstein et al. 2022; Atek et al. 2023) are of utmost importance going forward as if galaxies above $z = 11$ turn out to be essentially dust-free, this could go a long way towards reconciling the observations and theory Ferrara et al. (2023). What the reader should take away from this is that there are several potential avenues to alleviate this tension with the ΛCDM model to be closed off before we can say that the model is under question. The thesis has

4. The initial mass function describes the number of stars per mass that form at a galaxy's "birth", i.e. its first population of stars. This can make a significant difference in how we interpret galaxy properties (see Salpeter 1955; Kroupa 2001 and for example Popesso et al. 2023).

5. Stochastic star formation histories are a category of star formation histories that allow randomly distributed bursts of star formation.

developed in this exciting time when we can start to push the boundaries of cosmological models with astrophysical observations of the early universe.
Now that I have outlined a basic picture of what we know about the properties of the earliest galaxies, let us ask how these first galaxies impacted the neutral universe surrounding them ? The ionising radiation from the first stars started cosmic reionisation, changing the state of the IGM from neutral to ionised. Fig. 1.1 shows a lightcone from the Cosmic Dawn II (CoDa II) simulation (PI : P. Ocvirk), where light blue denotes ionised and dark denotes neutral regions of the Universe.

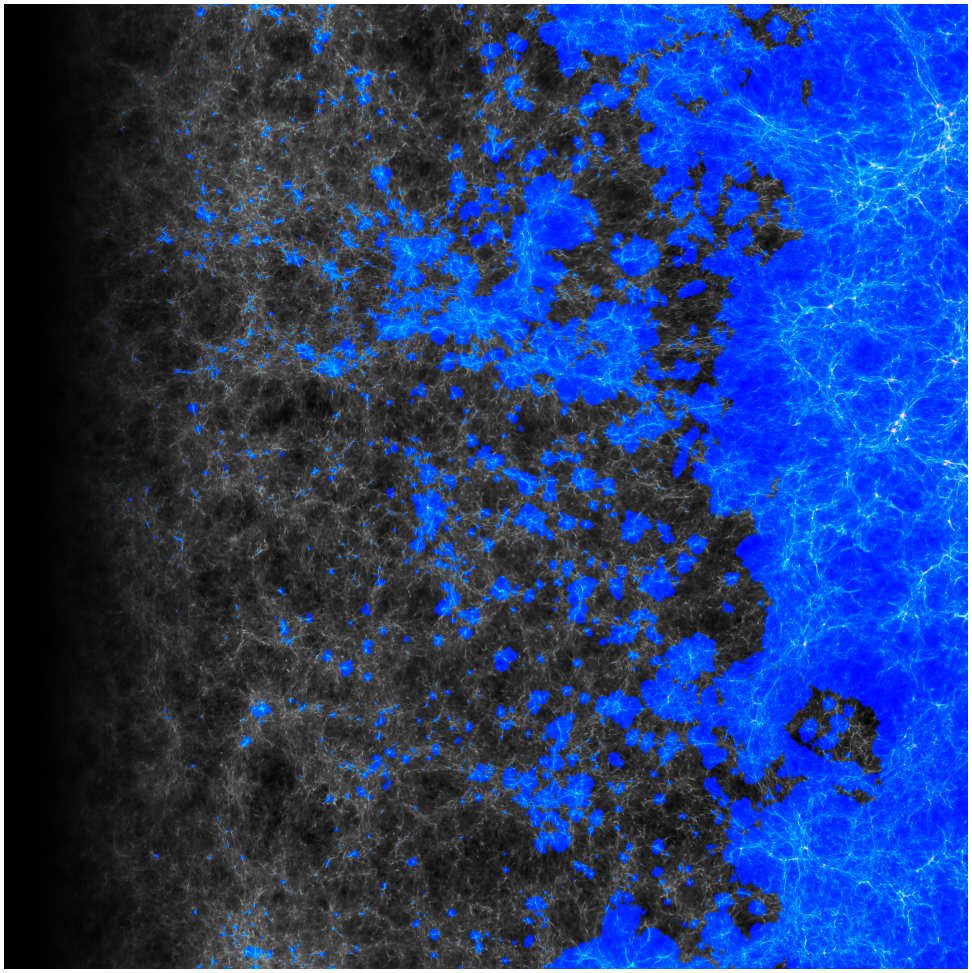

FIGURE 1.1 – A lightcone from the Cosmic Dawn simulation (Ocvirk et al. 2020). The blue colour shows ionised regions of the Universe and the white the large-scale structure. The figure shows the time evolution of the IGM (early times, high redshifts on the left).

The consensus, both from theory and from observations is that faint, star-forming galaxies ($M_{UV} \lesssim -18$) played the major role in this process (Finkelstein et al. 2015; Bouwens et al. 2015a,b; Livermore et al. 2017; Bouwens et al. 2021, 2022; Atek et al. 2024). This is due to the much greater number density of faint galaxies versus bright

galaxies. The relative contribution of bright galaxies and AGN is still discussed (Grazian et al. 2018; Naidu et al. 2020; Matthee et al. 2022; Grazian et al. 2022; Jiang et al. 2022; Kokorev et al. 2023; Harikane et al. 2023b; Dayal et al. 2024). These objects emit large quantities of ionising photons, but they are much rarer [6].
However, the first results from the JWST on galaxies within the EoR seem to suggest that large ionised bubbles form first in the neutral IGM around larger, brighter galaxies (Witstok et al. 2023; Witten et al. 2023; Goovaerts et al. 2023; Whitler et al. 2023b). These large ionised bubbles, driven by the most massive galaxies, as well as such galaxies situated in overdensities and undergoing mergers, clear an area around them in the IGM, and allow Lyman-α radiation to escape (see Section 1.4). This makes them easy to observe in the EoR, where Lyman-α radiation for many other galaxies is blocked.
As mentioned, the exact start of reionisation forms an ongoing search, but the end, from which the IGM remains fully ionised until the present day, is usually taken to be around $z = 6$, one billion years after the Big Bang (Stark et al. 2010, 2011; McGreer et al. 2015; Mason et al. 2018b; Planck Collaboration et al. 2020; Lu et al. 2022). There are studies which show that it may have ended later than this (Bosman et al. 2022; Zhu et al. 2022), as late as $z \sim 5.3$. In the context of this thesis, these results suffice to justify the interest in galaxies as late as $z = 5$ for the study of reionisation, particularly as the time elapsed between units of redshift becomes small at these times (only $200 - 250$ Myr between $z = 6$ and $z = 5$ and less at higher redshift).
The more detailed progression of reionisation, its topology and its exact start and end times are then still an open topic. The quest to better understand galaxy properties at these early times, which goes hand in hand with the study of reionisation, progresses also. The following section explains how we observe these galaxies and derive their properties, so that we may better understand galaxy evolution and reionisation.

1.3 Galaxy evolution and observation

The previous section summarises what we know about galaxy evolution in and around the EoR, but how do we know ? How were these galaxies observed and what techniques do we use to extract their properties ?
The typical way to detect high-redshift galaxies is from breaks in their spectral energy distributions (SEDs), observed with photometry. One sees flux from a galaxy in a certain band and all bands redwards, but nothing in the blueward bands (see Fig. 1.2). Based on the observed wavelength of this break and knowledge of its rest frame wavelength, the redshift of the observed galaxy can be computed using the well-known redshift equation :

$$z = \frac{\lambda_{obs} - \lambda_{rest}}{\lambda_{rest}} \tag{1.1}$$

There are several breaks in a galaxy SED which can create this kind of effect. The first is the Lyman break, which is caused by the absorption and scattering of all ionising

6. Certainly they are expected to be much rarer. The latest results are beginning to support this (Dayal et al. 2024).

photons ($\lambda < 912\,\text{Å}$) by neutral hydrogen in and around the galaxy. At higher redshifts, the Lyman forest absorbs the photons between 912 and 1216 Å, with efficiency increasing towards higher redshifts. The final result is a net break bluewards of 1216 Å that helps identifying high-redshift galaxies. Galaxies identified in this way are known as "Lyman Break Galaxies" (LBGs hereafter).
There is often (not always) a second break in a galaxy spectrum at 4000 Å. This break is caused by absorption in stellar atmospheres and a lack of young, hot blue stars. Close to this feature is a second break, or jump, called the Balmer break, found at 3646 Å. This wavelength corresponds to end of the Balmer series of hydrogen (i.e. the energy required to free an electron from the first excited state). This break is often seen in A-type stars, older and cooler than O and B-type stars. The strength of the these breaks tells us about the age of the dominant stellar population, and the balance between the old and young populations, where the young will be dominated by hotter stars.

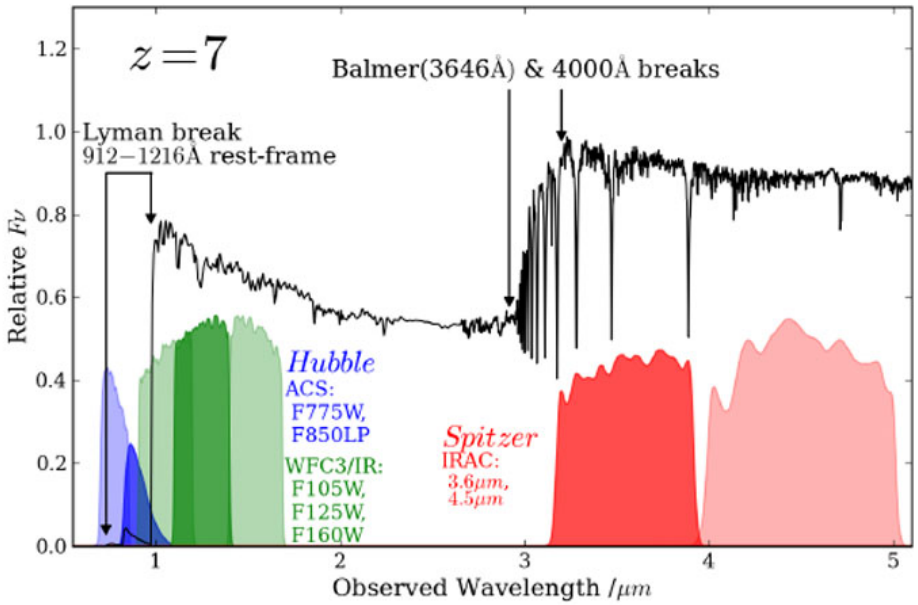

FIGURE 1.2 – A model of galaxy SED at $z = 7$. Selected Hubble Space Telescope filters are shown, as well as two Spitzer/IRAC filters. The Lyman break is clear and so is the 4000 Å/Balmer break. Taken from a series of lectures on observing the first galaxies by J. Dunlop (https://ned.ipac.caltech.edu/level5/Sept14/Dunlop/Dunlop3.html).

Care must be taken when observing these breaks in photometric data, as one break can sometimes be mistaken for another. Flux is expected bluewards of the Balmer/4000 Å breaks, but sometimes the sensitivity of the instrument is insufficient to detect it, and this feature can be mistaken for the Lyman break. Naturally this will cause a significant error in the redshift estimation of such a galaxy.
Additionally, strong emission lines, such as Hα or Lyman-α, may masquerade as one of these breaks and lead to erroneous conclusions about the properties of the galaxy.

On the other hand, when observing a galaxy spectroscopically, these features in the continuum of galaxies are often too faint to be detected, and we must rely on emission features to identify the galaxy's redshift and properties. Depending on its evolutionary phase and conditions in and around a galaxy, different emission (or absorption) features will be prominent in its spectrum.

A young galaxy which is actively forming stars will display lots of emission features, originating from atoms (mainly hydrogen, but also helium, carbon, oxygen, silicon, nitrogen and calcium, to name the most important) being ionised in stars and recombining to emit photons of specific and recognisable wavelengths. Galaxies such as this usually (although not always) contain little dust. Dust absorbs the radiation in the UV from stars and re-emits it in the infrared. The dust content of a galaxy and therefore its far-infrared luminosity, correlates well with its mass, anti-correlates with star-formation rate at a certain mass (up to $M_\star = 10^{10}\,M_\odot$) and correlates less well with the age of the stellar population (Garn &Best 2010; Zahid et al. 2013; Whitaker et al. 2017; Zimmerman et al. 2024).

An older, more passive galaxy would show little-to-no emission features, being dominated rather by absorption features, with a Balmer break possibly visible even in some spectra (when the galaxy is bright enough/the instrument is sensitive enough). These absorption features are caused by the same elements as the emission features of younger galaxies, but in older galaxies these elements are present in far greater quantities in the interstellar medium (ISM) and in the atmospheres of stars. As such, they absorb photons of a certain wavelength which results in absorption features in galaxy spectra. Note that absorption lines can originate from absorption in stars, the ISM, or some combination of the two. This makes them more difficult to interpret than emission lines.

These emission and absorption features allow us to calculate the redshift of a galaxy, as the rest frame wavelengths of these features are well-known. These redshifts are usually more reliable than photometric redshifts as identifying multiple emission and/or absorption features in a galaxy spectrum can make one very sure that they are correctly identified. Redshifts derived from photometry are more influenced by noise and misidentification of certain features (see Section 3.2). This covers the usual ways of identifying and finding the redshift of a galaxy, but subsequently there remain a great deal of more interesting properties to be estimated. To extract these properties from photometric data, we use SED fitting : we fit the fluxes in each filter observed to established models of galaxy spectra. These are built from stellar population spectra (e.g. Bruzual &Charlot 2003) where parameters of the galaxy, such as metallicity, age, stellar mass and star formation rate are allowed to vary. To this is added the effect of dust extinction and re-emission (e.g. Calzetti et al. 2000; Casey 2012).

Extracting physical properties from the spectra of galaxies proceeds in a different way. Each absorption and emission feature can be fit to extract the flux emitted or absorbed and used to derive properties of the galaxy. However, not only the flux of each line can be used to estimate galaxy properties. The width of lines can also be used to postulate that a galaxy contains an active galactic nucleus (AGN). This effect is due to broadening of emission lines by gas moving quickly around the accretion disk of an AGN (Gaskell 2009; Assef et al. 2012). The presence of emission lines caused by highly ionised species, such as

NV, is also a signature of AGN activity (Feltre et al. 2016).
The ratios between different lines also contain information, such as the gas-phase (as opposed to stellar) metallicity of the galaxy from the ratios such as the OIII/Hβ and NII/Hα [7] (among others, see, for example Nagao et al. 2006).
Absorption lines also contain information, particularly about the kinematics of galaxies, such as inflows and outflows in the ISM (Chen et al. 2010; Oh et al. 2011). However, as mentioned, they are more difficult to interpret than emission lines and require a detection of the galaxy's continuum, which is very rare in galaxies at higher redshifts (depending on the spectrograph used and exposure time of the observations in question). Therefore absorption features are rarely used to constrain the properties of galaxies at medium-to-high redshifts, such as those which will be the subject of this thesis.
Unique among emission lines in its power to inform us about a galaxy is the intrinsically strongest emission line : the first recombination line of hydrogen, called Lyman-α. This thesis has a strong focus on galaxies which exhibit this line, so the following section contains a review of the origin of this line and what it can tell us about the host galaxy.

1.4 Aside I : Lyman-α physics

Lyman-α radiation is the name given to the recombination of an electron in a hydrogen atom from the first excited state (principle quantum number $n = 2$) to the ground state ($n = 1$). This radiation is produced in galaxies when electrons in hydrogen atoms in the ISM are excited by ionising radiation ($\lambda < 912\,$Å) from young, hot, massive stars and fall back to the ground state (from the first excited state : there are a number of pathways which allow this : 68% of radiative cascades, see Dijkstra 2014), emitting a photon of a very characteristic wavelength as they do so : 1215.67 Å. In the spectra of galaxies, we can often see a peak at this wavelength due to this emission. Partridge &Peebles (1967) were the first to suggest the identification of galaxies (particularly those far away) using this line, due to its intrinsic strength.
A second method of producing Lyman-α photons in galaxies comes after from the cooling of hydrogen atoms following collisional excitation (Dijkstra 2014, 2016). However this likely accounts for only 10% of the Lyman-α emission produced by galaxies (Kerutt, J. et al. 2022), however, see also Dayal et al. (2010); Rosdahl &Blaizot (2012); Mitchell et al. (2021).
However, while certainly some Lyman-α photons are produced in every galaxy, not all galaxies produce enough for this line to be observable. Those that do, typically those that have an equivalent width of Lyman-α emission, henceforth $\mathrm{EW_{Ly\alpha}}$, greater than 25 Å, are called Lyman-α emitters, LAEs, although this is an arbitrary limit which in some cases should be ignored. I will return to this point in Chapter 4.
So, what makes a galaxy an LAE ? This question is far more subtle than the simple process of the emission of Lyman-α photons. The Lyman-α transition is resonant, which means it is re-absorbed, and re-emitted in a cloud of neutral hydrogen within a galaxy. Effectively

7. A word on notation for the reader new to the way emission and absorption lines are denoted in astrophysics (spectroscopic notation) : OIII denotes doubly ionised oxygen, so O^{2+}. HI denotes neutral atomic hydrogen. Hα, Hβ etc denote the Balmer series of hydrogen.

this scatters the Lyman-α photons, and in some cases, obscures them completely.
Lyman-α photons undergo a radiative transfer process on their way to escaping a galaxy, where they are randomly scattered by neutral hydrogen, or absorbed by dust grains. If the neutral hydrogen is moving, this can also change the frequency (a red or blue shift) of the photons, enhancing their chances of escape if they shift out of resonance.
As a result of such a complicated escape scenario, the Lyman-α emission that we observe from galaxies is influenced by many galaxy properties, such as neutral hydrogen content and distribution (Partridge &Peebles 1967; Dayal et al. 2011; Hayes 2015), dust content (Atek et al. 2008; Verhamme et al. 2008; Hayes et al. 2011, 2013; Runnholm et al. 2020) and geometry and viewing angle (Verhamme et al. 2012; Smith et al. 2022; Blaizot et al. 2023; Giovinazzo et al. 2024). At once then, Lyman-α emission contains a great deal of information about a galaxy, and is difficult to interpret.
With this in mind, what strategies do we use to observe the Lyman-α line and to extract a maximum of information from this important emission feature ? Two methods are generally employed ; targeting the Lyman-α line with spectrographs, or by searching for excess flux in narrow-band (NB) photometric observations. Both methods have advantages and challenges.
When trying to detect Lyman-α emission with spectroscopy, one can generally detect fainter LAEs, as well as obtaining information from the spectral shape of the line. However, due to the complicated escape scenarios for Lyman-α photons, and their high dependence on the distribution of neutral hydrogen in the galaxy, the Lyman-α emission is often extended or offset from the stellar (UV) emission (Shibuya et al. 2014; Hoag et al. 2019; Lemaux et al. 2021; Claeyssens et al. 2022). This creates problems when observing with a slit spectrograph or a multi-object spectrograph with small shutters such as NIRSpec's MSA mode. It is possible to observe only part of the Lyman-α flux, or indeed to miss it completely in these spectroscopic observations (Jiang et al. 2023). Needless to say, this can be problematic when trying to assess the global properties of a galaxy where one requires the total flux, such as the Lyman-α luminosity or the SFR derived from it. Moreover, spectroscopic searches are conducted on photometrically-preselected samples of galaxies, which can introduce biases, such as the targeting of only the UV-brightest galaxies.
The advantage of identifying Lyman-α emission from narrow-band photometric searches is the number of bright LAEs which are detectable due to the larger sky coverage, in addition to a search conducted without preselection. However the trade-off in this scenario is the possible presence of interlopers. As with photometry it is impossible to see the shape of the line, only the excess in a narrow-band filter is observed, it is much harder to distinguish Lyman-α emission and other strong spectral features. It is also difficult to reconstruct the Lyman-α flux from the filter (or filters, if the line lies in two adjacent filters) it is observed in. Finally, these NB searches result in LAEs identified only in a small and specific wavelength range, where the Lyman-α emission crosses the NB filter used for the identification.
A method which suffers few of these issues is LAE identification in integral field unit spectroscopy (with an integral field unit such as VLT/MUSE, see Chapter 2 for details on this instrument). With an integral field spectrograph, the resulting data is 3-dimensional. There are two spatial axes and one spectral, such that each pixel comes with an x and y

position, and a spectrum. This means the full spatial extent of the Lyman-α emission can be taken into account, there is no need for a photometric preselection and the search for LAEs can be extended over the wavelength range of the instrument. This method also enables the detection of LAEs (or line emitters in general) without continuum counterparts [8].

There are several useful observables of Lyman-α emission. Firstly, using any of the above methods, we can extract the flux of the emission line, which translates directly to a Lyman-α luminosity. Using this value and the intrinsic relative strengths of the Lyman-α and Hα line (Kennicutt 1998b; Schaerer 2000), one can derive the SFR from the Lyman-α flux. This is usually taken to be a lower limit on the intrinsic SFR, due to the escape of Lyman-α photons being non-unity (a scenario which almost certainly doesn't hold in all cases).

The equivalent width of Lyman-α emission (henceforth $\mathrm{EW}_{\mathrm{Ly}\alpha}$, in Å), denotes the strength of this emission line. It is calculated by dividing the Lyman-α flux by the continuum flux under the line (i.e. at 1215.67 Å). This quantity is often used to classify a galaxy as an LAE (if it has $\mathrm{EW}_{\mathrm{Ly}\alpha}$ greater than a certain value, usually taken to be 20 or 25Å). Any such classification is inherently arbitrary however and care should be taken over selection effects related to this (more on this point in Chapter 4).

The most interesting facet of observing the Lyman-α line however, is the shape of the line itself. This, of course, can only be observed with spectroscopy and is also dependent on the spectral resolution and sensitivity of the instrument used, and the conditions around the LAE. This last is due to the many effects on the propagation of Lyman-α photons and therefore impact on the shape of the resultant observed line (Verhamme et al. 2006, 2012; Dijkstra &Kramer 2012). As mentioned, the ISM, circum-galactic medium (CGM) and IGM conditions all effect this. Scattering within the ISM and CGM often gives the Lyman-α line a broader profile [9], and can result in features both redwards and bluewards of the line centre ($\sim$ 1216 Å) (double or multiple peaks).

A recent compilation (Blaizot et al. 2023) lists the zoo of Lyman-α line shapes that have been observed : single peaks, P-Cygni peaks, double peaks and multiple peaks. Some examples of these lines (matched to models from Blaizot et al. 2023) are shown in Fig. 1.3.

8. These curious objects are discussed in greater detail in the Chapters dealing with the results of this thesis.

9. This is due to the relative motion of these components of the galaxy.

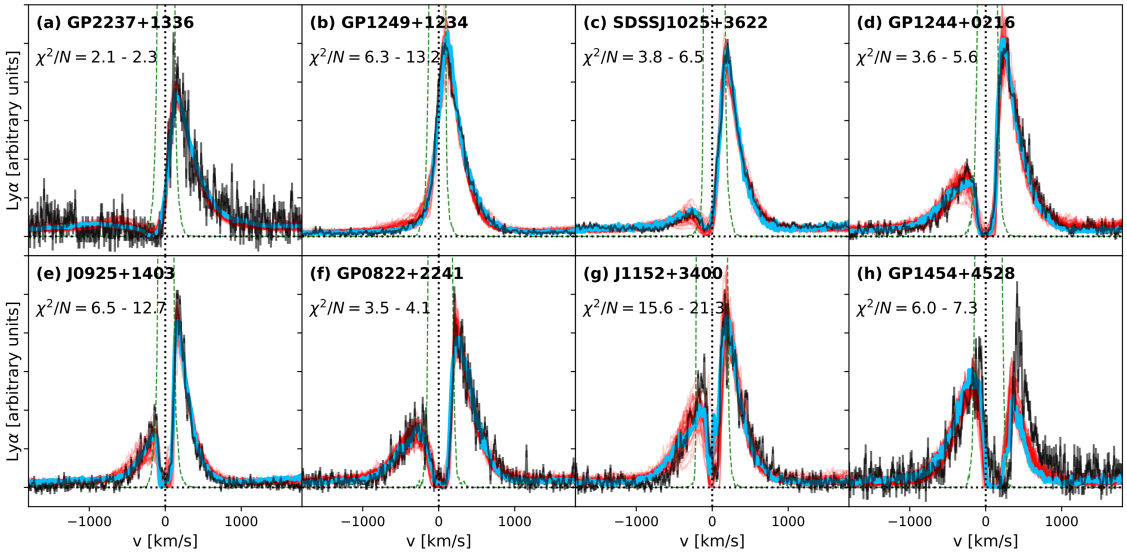

FIGURE 1.3 – The diversity of the Lyman-α line shape. A (non-exhaustive) figure of observed Lyman-α line shapes (forming part of the Lyman-Alpha Spectral Database (Runnholm et al. 2021) and fit to mock spectra by Blaizot et al. 2023).

Single peaks are peaks detected without an absorption trough, sometimes called a valley, bluewards of the line. Many peak shapes have been observed, and encode information about the distribution and conditions of the neutral hydrogen in and around the galaxy. The offset of the line from the systemic redshift of the galaxy (i.e. the offset from $1216\,\text{Å} \times (1+z)$) encodes the speed of any out or inflows from the galaxy.
P-Cygni profiles are single peaks with a single absorption feature bluewards of the line. These peaks are uncommon and are likely due to IGM absorption (Garel et al. 2021; Blaizot et al. 2023).
Double peaks are the most common of the Lyman-α line profiles, certainly at low redshift, where there is no significant IGM to absorb the blue part of the line (as it redshifts into resonance). There are many varieties of double-peaked Lyman-α lines. This phenomenon is often taken to be the signature of movement in the ISM and CGM, i.e. inflows and outflows, that red and blueshift the Lyman-α emission. The offset of the lines from the systemic velocity can tell us the speed of the inflows and outflows Hashimoto et al. (2015); Gronke et al. (2015), and the separation of the two lines has also been used as a tracer for Lyman continuum (LyC) photon escape (e.g. Verhamme et al. 2015, 2017; Choustikov et al. 2024a).
Multiple peak profiles, i.e. more than two peaks (and more than one valley), represent a low percentage of all observed Lyman-α lines. They can emerge from multiphase media undergoing outflows (Gronke &Dijkstra 2016; Blaizot et al. 2023).
Viewing angle has also been reported to shape the observed profile from an LAE Verhamme et al. (2012); Smith et al. (2022), although there is no general consensus on exactly how the inclination of the galaxy effects the profile.
Having now outlined what Lyman-α emission is, what we observe from LAEs and the

complications of the line, I will move on to describe what we know about the galaxies that emit this radiation.

LAEs are rare in the local universe, just 5% of local galaxies display Lyman-α emission (over 20 Å, Cowie et al. 2010; Hayes 2015), however, they become more numerous in the higher-redshift universe, up to $z = 6$ (Stark et al. 2010, 2011; Arrabal Haro et al. 2018; Caruana et al. 2014, 2018; de La Vieuville et al. 2020). After $z = 6$, the fraction of the galaxy population observed to be LAEs decreases (note here "observed to be LAEs" means $EW_{Ly\alpha} > 25$ Å, this point becomes very important in Chapter 4). This decrease has been taken to trace the increasing neutral fraction of the IGM during reionisation. The neutral hydrogen atoms in the IGM at this time absorb the Lyman-α photons. This can be helpful to track the timeline of reionisation and to uncover, in a more detailed way, the galaxies that were responsible for this process. This is a subject central to this thesis and is addressed in later chapters.

LAEs in general [10] are observed to be galaxies with high specific SFRs (sSFR) which tend to be young, low-metallicity, high-ionisation state galaxies (De Barros et al. 2017; Karman et al. 2017; Santos et al. 2020a; Matthee et al. 2021; Goovaerts et al. 2023; Iani et al. 2023; Goovaerts et al. 2024). This is to be expected as a galaxy needs hot, young, blue stars to create the ionising photons necessary to eventually create Lyman-α emission. It also needs a quantity of neutral hydrogen to be ionised and recombine. However, it is not exclusively young, dust-free galaxies that exhibit this emission ; dusty, older galaxies also sometimes display Lyman-α emission (see, for example, Atek et al. 2008; Verhamme et al. 2008; Hayes et al. 2013; Runnholm et al. 2020). Star formation events can be triggered in galaxies, for example by major or minor mergers, or galaxies can undergo highly stochastic star formation (i.e. with many individual bursts of star formation) (Ciesla et al. 2023), meaning that the ionising photons needed to produce Lyman-α radiation may be produced at times other than when a galaxy is young. However, the galaxies showing the strongest Lyman-α emission (in terms of $EW_{Ly\alpha}$), and highest escape fraction of Lyman-α photons (henceforth $f_{esc,Ly\alpha}$) have been observed to mainly be young and low-mass (Ando et al. 2006; Hayes et al. 2013, 2014; Hayes 2015; Maseda et al. 2020a; Santos et al. 2020a).

The properties of LAEs listed above and therefore the expected conditions for Lyman-α emission to be produced by a galaxy, do not, however, guarantee the escape of the Lyman-α photons from the galaxy (or from the neutral IGM at higher redshifts). Also for this reason, then, LAEs are expected to be dust-poor (at least the LAEs we observe, more on this in Chapter 6). Often this also means that we observe LAEs with significant outflows, as this creates channels in the neutral hydrogen for Lyman-α to escape (Matthee et al. 2021; Ferrara 2023; Tang et al. 2024). The stellar properties of LAEs listed above are not unique to LAEs, they are also often the properties of star-forming galaxies not selected as LAEs (i.e. the LBG population) at similar redshifts (see Ouchi et al. 2020 and references therein, as well as Goovaerts et al. 2023; Goovaerts et al. 2024). Therefore it seems clear that features of a galaxy other than the characteristics of the stellar population play a large role in whether this galaxy is observed as an LAE.

10. "In general" here has been used advisedly. As mentioned, due to the complicated nature of Lyman-α escape, there are a range of scenarios in which galaxies display Lyman-α emission. The properties of these galaxies are reported here as general trends among the population ; it is worth remembering there are significant exceptions, as well as significant scatter in the data.

Lyman-α haloes – the name given to the phenomenon of observing extended Lyman-α emission around a more compact UV source – are also common, both at low and high redshift (Hayes et al. 2014; Hayes 2015; Wisotzki et al. 2016), tracing the extent of neutral hydrogen around galaxies. Lyman-α emission is often more extended than the stellar emission observed in the UV part of the spectrum, and can be partially or wholly offset from it Jiang et al. (2013); Claeyssens et al. (2022); Jiang et al. (2023). Studying the morphology of Lyman-α emission (and in particular the relative morphology with respect to the stellar emission), helps us to trace the neutral hydrogen in a galaxy and therefore the conditions of the ISM and CGM.

In summary, we observe a huge variety of Lyman-α profiles from a range of different types of galaxies, including recently within the EoR (Witstok et al. 2023; Witten et al. 2023; Hayes &Scarlata 2023; Chen et al. 2023; Nakane et al. 2023), where it was once thought that the neutral IGM would make it too difficult for Lyman-α photons to escape. The study of LAEs as a galaxy population, as well as Lyman-α physics on a more "micro", which is to say galactic, scale, is an ongoing and active area of research. The strength of the line makes it attractive to use in galaxy detection, especially for intrinsically faint galaxies which may be difficult to observe without this line, and the amount of information we can gain from its study ensures plenty of continued interest.

1.5 Aside II : Gravitational lensing

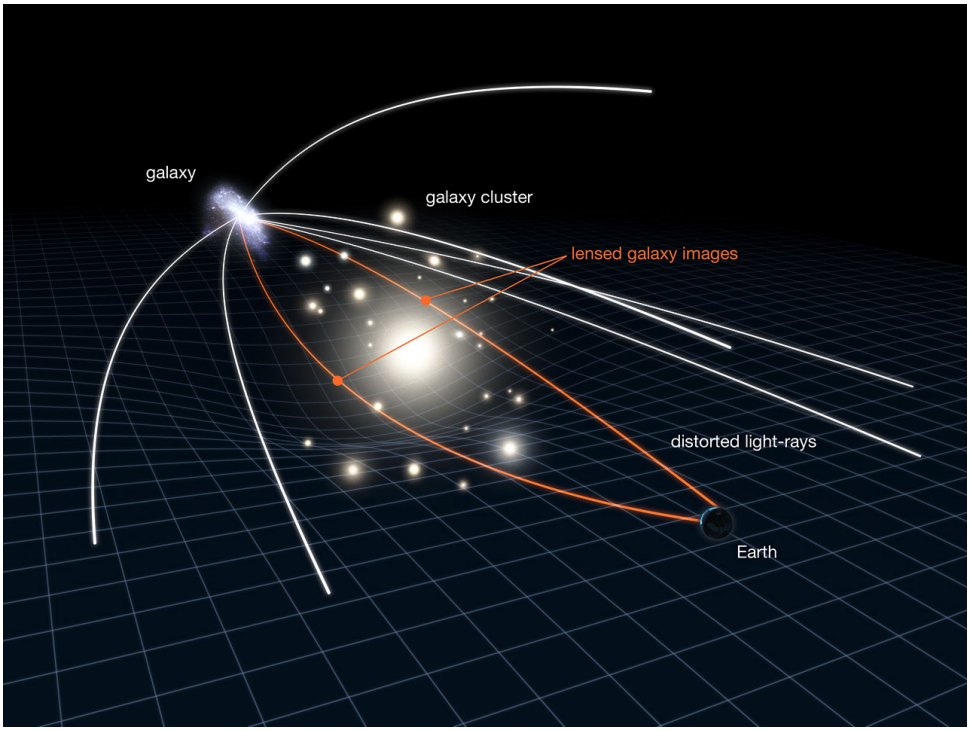

FIGURE 1.4 – A diagram of the effect of gravitational lensing of a background galaxy by a foreground cluster of galaxies (not to scale). Credit : ESA Hubble : https://esahubble.org/images/heic1106c/

To access certain, intrinsically faint populations of galaxies, those concerned by this thesis, and those of most interest as the main sources of cosmic reionisation, we need to use all the tools at our disposal. These galaxies are very difficult to image (or to obtain spectra for), due to their low luminosity, and often the only way to observe these systems is using gravitational telescopes, a technique used for the first time by the French community in the 1980s (Soucail et al. 1987, 1988; Pello-Descayre et al. 1988). The usage of this technique allows us to detect faint galaxies that are beyond the reach of currently available telescopes in non-lensed fields (blank fields). Gravitational lensing magnifies a background galaxy (in an analogous manner to a magnifying glass) by amplifying its size but conserving its surface brightness. This thesis focuses exclusively on gravitationally lensed galaxies, so I will describe in this section a brief mathematical formalism, some practical consequences for the data I used and how it has helped achieve the goals of this thesis. For a full formalism, I recommend Kneib et al. (1996, 2011); Kneib &Natarajan (2011).
Photons from far away galaxies, following geodesics, are deflected by large masses along the line of sight. This produces distortions in the images we observe of these background galaxies, and in extreme cases, multiple images of the same galaxy (see Fig. 1.4). According

to general relativity, the angle of deflection of these background galaxy photons is

$$\alpha = \frac{4GM}{c^2 b} \tag{1.2}$$

where M is the mass of the lens and b is the impact parameter (this equality is subject to the ratio M/b being small – this is always the case for gravitational lenses such as those we are considering). With this deflection angle α, we can calculate the source-plane position of an object we observe (here source plane means the plane of the object under consideration : high-redshift galaxies for the purpose of this thesis). Since these distant objects are very far away from us as observers relative to the size of the lens (in all directions), we approximate the lens as infinitely thin. The situation is then similar to that in Fig. 1.5. The relation between the observed angle to a background galaxy, θ, and true angle, β, can be written as (using the small-angle approximation) ;

$$\beta = \theta - \alpha(\theta), \tag{1.3}$$

In the simplest cases, this is used to calculate the position of a lensed object in the source plane, but when dealing with galaxy clusters, the situation is not the simplest case. There are many constituent members of clusters of galaxies, each playing a role in the total gravitational potential.

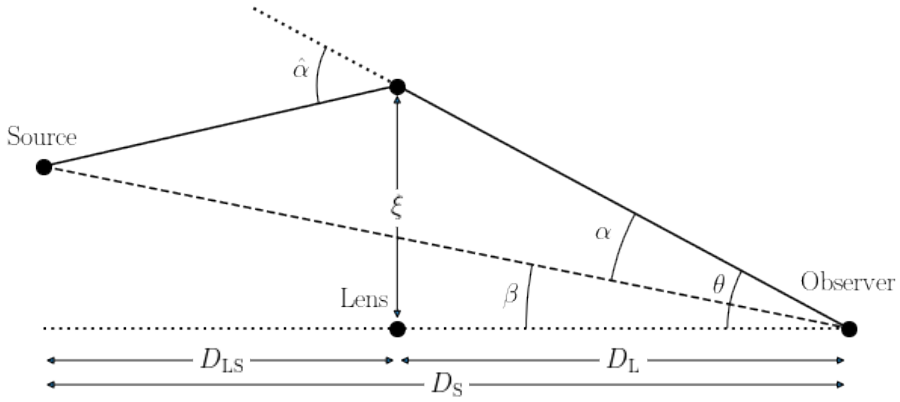

FIGURE 1.5 – A schematic diagram of the lensing situation. Credit : Jo Bovy, Dynamics and Astrophysics of Galaxies : https://galaxiesbook.org/chapters/III-04.-Gravitational-Lensing.html

The quantity of greatest interest for the observation of faint, distant galaxies is the magnification, μ, that is created by the lens, and is different for each multiple image. Here I simply state it, for a derivation, I find the LENSTOOL (Jullo &Kneib 2009; Kneib et al. 2011) manual written by Mike McCourt to be a good starting place [11], and a more

11. It can be found at : https://projets.lam.fr/projects/lenstool/wiki

thorough treatment is given in Schneider et al. (1992) and the references for the full lensing formalism (Kneib et al. 1996, 2011; Kneib &Natarajan 2011).
We have the surface mass density of the lens :

$$\kappa(\theta) \equiv \frac{\Sigma(D_l\theta)}{\Sigma_{cr}} \tag{1.4}$$

where

$$\Sigma_{cr} \equiv \frac{c^2}{4\pi G}\frac{D_s}{D_l D_{ls}} \tag{1.5}$$

is the critical density of the lens, above which multiple images can be produced. With these two quantities, as well as the lensing potential

$$\psi(\theta) \equiv \frac{1}{\pi}\iint_{R^2} \kappa(\theta)\ln|\theta - \theta'|d^2\theta' \tag{1.6}$$

where R is the radius from the centre of the lens and θ' is a small change in the angle θ (Fig. 1.5), we can write the magnification factor

$$\mu = \frac{1}{det\, A}, A = \begin{bmatrix} 1-\kappa-\gamma_1 & -\gamma_2 \\ -\gamma_2 & 1-\kappa+\gamma_1 \end{bmatrix} \tag{1.7}$$

where $\gamma_1 \equiv \frac{1}{2}(\psi_{,11} - \psi_{,22})$ and $\gamma_2 \equiv \psi_{,12}$. This magnification factor varies across the lensing area according to θ and rising to very high values in certain areas, formally becoming infinite at certain points. These points form a curve, called a critical line, such as the red line in Fig. 1.6. On the inside of these lines (the innermost curve in Fig. 1.6), the source becomes demagnified, i.e. the sign of the magnification flips and there is an inversion in the morphology of the image. This effect often helps to identify multiple image systems with two images either side of a critical line.
In a real-world scenario, figuring out the deflection experienced by the light from a background galaxy becomes the realm of modelling. Such a process starts by assuming a distribution of mass, usually based on the identification of the members of the cluster of galaxies, although there are various approaches one can take. Incorporating weak lensing can be useful, especially where a large area of the cluster (and surroundings) is covered by sufficiently deep imaging (Limousin et al. 2007). The information from the slight distortions in galaxy shapes caused by the weak lensing adds additional constraints on the resulting lens models.
The mass of the dark matter haloes in which these cluster members reside is necessary, and requires assumptions. Multiple images are identified behind the cluster, using their redshift and morphology. This is still a manual process, and experience identifying multiple images helps greatly.

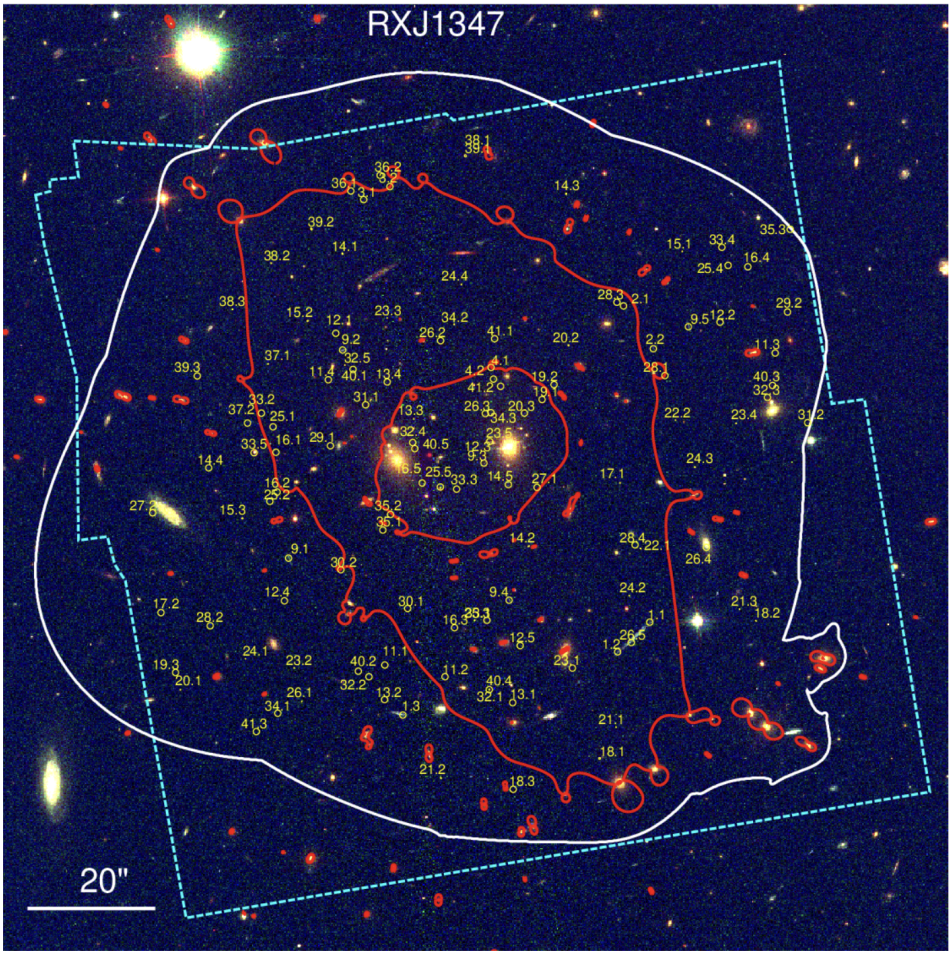

FIGURE 1.6 – VLT/MUSE image of the lensing cluster RXJ1347 from Richard et al. (2021). Multiple images are numbered in yellow, critical lines are traced in red and the strong lensing area, where multiple images are expected, is denoted by the white line.

Taking all these multiple image systems, the source positions of the galaxy are calculated using the mass distribution. How closely these positions coincide gives an idea of the quality of the mass model (i.e. all images of the same galaxy should end up in the same place in the source plane). Repeating the process in reverse does the same, if the model is good, the images should return to their observed positions. This process is used to iteratively improve the mass models for clusters, meaning the process is highly dependent on the number of correctly identified multiple image systems behind the cluster under consideration (I will return to this point later). `LENSTOOL` (Jullo et al. 2007; Jullo &Kneib 2009, see also Kneib et al. 1996, 2011) was the software used for this purpose during the course of my thesis. The specific lens models I used for the clusters concerned in this work are described in Sect. 2.4.
`LENSTOOL` uses a parametric approach to constructing mass models of galaxy clusters, where each component of the cluster contributes a sub-potential, summing to create the overall gravitational potential. These sub-potentials are parametrised by a position, shape

and density profile, which, for LENSTOOL, come from analytical profiles of dark matter haloes. The parameters associated with each halo are then optimised as aforementioned, by minimising the distance between the projected multiple images and the real, observed multiple images.
In the end, the best mass model is used to compute the magnification at each point in the image plane, therefore used to calculate the magnification of each lensed galaxy. These magnifications and the uncertainties thereon are subsequently used to correct the derived parameters of the studied galaxies, so, understandably, well constrained mass models and well understood uncertainties are essential when it comes to ultimately deriving the quantities of interest.
This can be problematic in the areas near the critical curves, as the magnification rapidly diverges (theoretically to infinity on the critical curves), and often different models do not agree on magnification values at any given point in these regions (Limousin et al. 2007). The use of lensing then, comes with huge benefits, i.e. magnifying intrinsically faint galaxies, such that they may be observed with our current telescopes, and even, in some cases, making it possible to resolve regions of galaxies at the 100s or even 10s of parsecs scale at $z > 2$ (Bouwens et al. 2022a; Claeyssens et al. 2023; Vanzella et al. 2023). This, at present, is the only way to resolve star-formation processes on these small scales at these higher redshifts (rather than in the local universe). There are even reports of a single star detected in a hugely magnified galaxy at $z = 6$ (Welch et al. 2022). However, using lensing comes equally with difficulties and compromises. The volume of surveys is smaller in lensing fields than in blank fields as when one calculates the magnified volume that is mapped from the source plane to the image plane, this is of course smaller than the equivalent area in a blank field. There are greater computational challenges to deal with, handling the aforementioned lens models and carefully calculating magnifications for each galaxy, as well as finding new multiple images. Finally there are additional errors from the uncertainty in the magnification to consider when one comes to estimating galaxy physical properties [12]. Regardless of these challenges, the use of lensing to access these faint populations is essential if we want to better understand the small progenitors of modern galaxies, as well as the faint galaxies that are likely to be the dominant contributors to reionisation.

1.6 Where are we now ?

Now that the relevant areas of astrophysics in the thesis have been covered in a general manner, I'll take some time to outline the state of the field at the commencement and during the course of the thesis.
The later stages of reionisation had already been explored with the capabilities of the HST (for an excellent review, see Dayal &Ferrara 2018, and the studies of the UV LFs by Bouwens et al. 2015a, 2021, 2022).
The launch of the JWST in December 2021 (three months after the start of the thesis) and

12. Note that magnification does not affect every property. Anything where a ratio of properties are taken, for example the equivalent width of an emission line, or any line flux ratios, are not affected by lensing magnification.

subsequent early release data and images in the summer of 2022 catapulted the field of early-universe galaxy evolution forward at breakneck pace. Many would contend, too fast. Results were reported with imperfect calibrations, days after data release, which turned out to be false (Adams et al. 2023). Once the initial burst faded and the community took stock, more robust detections of extremely high-redshift galaxies ($z > 11$), both photometric and spectroscopic did emerge. UV LFs were constructed up to $z = 15$ (Naidu et al. 2022; Donnan et al. 2023; Harikane et al. 2023a; Atek et al. 2023; Donnan et al. 2024; Adams et al. 2024) and more robust properties of high-redshift galaxies were reported (see Section 1.2).

So, where does the work developed as part of this thesis fit into this landscape ? A driving theme of the thesis has been the investigation into intrinsically faint star-forming galaxies, which are, as mentioned, likely the most important contributors to reionisation. The tools needed to investigate these objects have shaped the thesis equally : gravitational lensing and Lyman-α emission. The LAEs studied come from VLT/MUSE observations, which are described in the following chapter. The redshift range that the MUSE spectral coverage allows us to access is $2.9 < z < 6.7$, meaning the results of this thesis probe the end of the reionisation epoch all the way nearly to cosmic noon. The focus, however, has been firmly on the EoR, as the populations we have studied at $z > 5$ are exactly the galaxies responsible for the majority of cosmic reionisation. An added benefit of working at these redshifts has been access to large samples of galaxies, such that we can draw conclusions in a statistically meaningful manner. This is only beginning to be possible within the EoR, with the largest and most ambitious JWST programs, so the work in this thesis is essential to complement the smaller studies done at higher redshift.

More specifically, the properties of these galaxies (LAEs and continuum-selected galaxies) have taken centre stage, while keeping a constant eye on how these properties suggest the galaxies impacted on the IGM around them. Investigation of this kind has been an active field during the thesis, with the study of LAEs as current as ever. Great strides have been made during the thesis years into LAEs within reionisation, clearing ionised bubbles and thus becoming visible (Witten et al. 2023; Witstok et al. 2023; Whitler et al. 2023b), the connection between Lyman-α radiation and ionising LyC radiation (Hu et al. 2023; Liu et al. 2023b; Kerutt et al. 2024; Pahl et al. 2024; Choustikov et al. 2024a; Begley et al. 2024; Jaskot et al. 2024) and the properties of LAEs and the escape of Lyman-α photons (Iani et al. 2023; Lin et al. 2024; Tang et al. 2024; Napolitano et al. 2024). Many of the results of these works are discussed relative to the findings of this thesis in later chapters.

The outline of this thesis is as such : chapter 2 describes the data used to achieve the goals of the thesis : data from VLT/MUSE, HST and JWST. Chapter 3 is based on the results pertaining to galaxy properties from Goovaerts et al. (2023) and Goovaerts et al. (2024) while Chapter 4 covers the results on the Lyman-α-emitting fraction, which probes the global progression of reionisation (also from Goovaerts et al. 2023). Chapter 5 is based on the final paper of my thesis (Goovaerts, Thai et al., submitted), investigating the escape fraction of Lyman-α photons and the impact of LAEs on reionisation. Chapter 6 details ongoing and further enquiry as part of the framework built up in during the thesis, and offers conclusions and prospects based on this work and the state of the field.

Throughout this work I adopt a cosmology typical for works like this in the literature,

with a Hubble constant of $H_0 = 70\,\mathrm{km\,s^{-1}Mpc^{-1}}$, and $\Omega_\Lambda = 0.7$ and $\Omega_\mathrm{m} = 0.3$. The adopted IMF is that of Salpeter (1955) unless otherwise stated and explained. All galaxy properties are given corrected for lensing magnification, unless otherwise stated.

2 Data : VLT/MUSE, HST and JWST

"Astronomy compels the soul to look upward, and leads us from this world to another."

- Plato, The Republic

Author's note on content : *This section contains the details of the data I used to investigate the physics presented in this thesis. I cover IFU spectroscopy from VLT/MUSE, with which I detected LAEs, and the photometry from HST and JWST in the Hubble Frontier Fields with which I detected LBGs and derived galaxy properties from the continuum emission.*

Author's note on context : *I spend a great deal of time getting to grips with these data sets when I arrived in Marseille, my previous background was not at all related to spectroscopy, IFU data or rest frame UV/optical photometry. Soon however I began to see the power of combining these different datasets and this has formed a crucial part of the thesis as well as my interests and research goals for the future.*

2.1 VLT/MUSE

I will start by shortly describing the VLT/MUSE (Multi-Unit Spectroscopic Explorer) instrument, followed by how I used it for my goals when looking at lensing cluster data. MUSE is an integral field spectrograph (IFS), observing between 460 and 940 nm. Instruments such as MUSE observe a field and give a datacube containing a spatial dimension (for MUSE this field of view (FoV) is $1 \times 1\,\mathrm{arcmin}^2$) and a spectral dimension, such that one gets a full spectrum between 460 and 940 nm for each pixel observed. The spatial and spectral resolutions of MUSE are $0.2''$ and 1.25 Å respectively. For full details on the instrument, please refer to Bacon et al. (2010, 2015, 2023).

2.1.1 The LLAMA Sample

MUSE's spectral range means it can detect Lyman-α emission in the redshift range $2.9 < z < 6.7$. The science one can address with LAEs is wide-ranging and important across a variety of fields, therefore the study of LAEs was one of the primary science goals of MUSE and one which was addressed early in the instrument's lifetime (Drake et al.

2017; Leclercq et al. 2017; Hashimoto et al. 2017). The first lensing cluster observations (in the guaranteed time observations (GTO)) by MUSE were performed by Richard et al. (2015) and culminated in the atlas of MUSE lensing cluster observations presented in Richard et al. (2021). From this rich dataset, Claeyssens et al. (2022) constructed the Lensed Lyman-Alpha Muse Arcs Sample, or LLAMAS. This sample contains 963 images of 602 individual lensed LAEs, from 17 lensing clusters.
For this study, I used those lensing clusters in the LLAMA Sample which are also part of the Hubble Frontier Fields (HFF) (see Sect 2.2). These are Abell 2744, Abell 370, Abell S1063, and MACS 0416 (henceforth A2744, A370, AS1063, and M0416). These are among the best-studied lensing clusters, observed by many different observatories and even programs within the same observatory. MUSE integration times on these clusters vary between 2 and 14 hours, with different pointing configurations (see Fig. 1 of Richard et al. 2021). The clusters are all in the range $0.3 < z < 0.4$, providing magnifications useful to amplify sources at the redshifts where MUSE can detect Lyman-α emission. Details of the four clusters, together with how many galaxies were detected in each, are given in the following chapter (Table 3.1). Full details covering all 17 LLAMAS clusters can be found in Claeyssens et al. (2022) and Thai et al. (2023). The full data release described in Richard et al. (2021) and Claeyssens et al. (2022) : datacubes, lens models and catalogues, is available online [1].

2.1.1.1 Source detection and flux calculation

In order to detect line emission sources such as LAEs, Richard et al. (2021) follow the prescription laid out in Weilbacher et al. (2020), using the MUSELET software (Piqueras et al. 2019) [2], which is used on MUSE NB images. Subsequently, the Source Inspector package (Bacon et al. 2023) is used to identify sources and assign their redshifts. This package allows users to cycle through a list of sources with all the relevant information : spectra, NB images, HST counterparts, MUSELET results, and redshift suggestions. With this information, users can decide on a redshift for an object as well as assigning each source a redshift-confidence level from 1 to 3. A confidence level of 1 denotes a tentative redshift and a confidence level of 3 denotes a redshift with a high confidence. For this study I only used LAEs with confidence levels of 2 and 3, indicating secure redshifts. In the sample – A2744, A370, AS1063, M0416 – there are 263 such LAEs.
The Lyman-α flux was extracted using one of two different methods. The main method employed in the LLAMA Sample is the line profile fitting procedure described in Claeyssens et al. (2022). For the subsample used in this work (263 LAEs), all those behind A2744 and 20 behind the other three clusters (roughly half the subsample), a method involving SExtractor (Bertin &Arnouts 1996) was employed, following the procedure outlined in de La Vieuville et al. (2019). I give a brief description of both methods.
The line profile fitting method utilises three steps : spectral fitting, NB image construction and spectral extraction. The first step involves fitting an asymmetric Gaussian function to the Lyman-α peak with the EMCEE package from Foreman-Mackey et al. (2013),

1. https://cral-perso.univ-lyon1.fr/labo/perso/johan.richard/MUSE_data_release/
2. https://mpdaf.readthedocs.io/en/latest/muselet.html

using 8 walkers and 10,000 iterations (in double peaked cases, both peaks are considered separately and their fluxes combined after the extraction is complete). The peak position of the Lyman-α line, flux, full width at half maximum, and asymmetry of the source are all fitted. The second step takes the result for the peak position and creates a NB image around the LAE. The continuum around the LAE in redward and blueward bands of width 24 Å is subtracted from the Lyman-α flux. The NB bandwidth is optimised such that the S/N of the Lyman-α peak is maximised in an aperture of radius 0.″7. Finally, utilising this new NB image of the LAE, a new extraction is performed from the MUSE datacube, ensuring that as much of the Lyman-α emission from the galaxy and surrounding halo is extracted. The process is repeated twice more, each time using the latest NB image and extraction.

The second method was employed for A2744 and in the three other clusters for the cases where the first method failed to fit the Lyman-α flux. This happened in very low signal-to-noise cases or sources close to the edge of the datacube. This method uses SExtractor on NB images as described in de La Vieuville et al. (2019). The NB images in question are those in which each LAE is detected. Three sub-cubes are extracted from the main datacube, one encompassing the Lyman-α emission and two either side of it (spectrally) each of width 20 Å. These cubes are averaged to form a continuum image, which is subtracted pixel-by-pixel from an image formed by averaging the cube containing the Lyman-α emission. SExtractor is then run on this new continuum-subtracted image and the `FLUX_AUTO` parameter is used to estimate the fluxes of the LAEs. To deal with faint sources or those with an extended, low surface brightness, SExtractor can progressively loosen the detection conditions (using the `DETECT_THRESH` and `DETECT_MINAREA` parameters) so that a flux can also be extracted for these sources.

Figure 4 of Thai et al. (2023) shows the comparison between the two methods of extracting the Lyman-α flux. In general, the two methods agree well. In some cases, the line profile fitting method estimates a larger flux due to its enhanced appreciation of the line complexity.

Lyman-α luminosities are derived from the fluxes described above and also magnification-corrected. In terms of Lyman-α luminosity the sample probes roughly between $39.5 < \log_{10}(\mathrm{L_{Ly\alpha}}/\mathrm{erg\,s^{-1}}) < 42.5$, with decreased statistics near the faintest and brightest limits. This faint population can at present only be accessed with lensing clusters ; the typical limit in blank fields lies around $\log_{10}(\mathrm{L_{Ly\alpha}}) \sim 42$ (see, for example, Herenz et al. 2019), down to $\log_{10}(\mathrm{L_{Ly\alpha}}) \sim 41.5$ in the MUSE Ultra Deep Field (Drake et al. 2017).

2.2 HST photometry : HFF

The HST observations of the clusters used in this work are from the Hubble Frontier Fields programme (ID : 13495, P.I : J. Lotz, Lotz et al. 2017). In particular, I used the photometric catalogues of the HFF-DeepSpace programme (Shipley et al. 2018). As part of this programme, the authors collected homogeneous photometry across the HFF, including deep K_S-band imaging (2.2 μm) from the HAWK-I on the Very Large Telescope (VLT) and Keck-I MOSFIRE instruments (Brammer et al. 2016). Additionally included are all available data from the two *Spitzer*/IRAC channels at 3.6 μm and 4.5 μm. The two

TABLE 2.1 – 5σ limiting magnitudes of each filter for the four clusters.

Filter	**A2744**	**A370**	**AS1063**	**M0416**
F225W	–	–	24.0	24.4
F275W	26.0	25.7	25.9	25.7
F336W	26.7	26.2	26.3	26.2
F390W	–	–	25.4	25.7
F435W	27.5	27.2	27.3	27.5
F475W	–	26.6	25.8	26.2
F606W	27.7	27.3	27.5	27.7
F625W	–	25.6	25.5	25.9
F775W	–	–	25.5	25.6
F814W	27.8	27.5	27.7	27.9
F850LP	–	–	25.2	25.2
F105W	27.9	27.2	27.6	27.7
F110W	–	26.6	26.4	26.3
F125W	27.4	27.0	27.4	27.6
F140W	27.4	27.1	27.3	27.7
F160W	26.8	26.9	26.9	27.4
K_S	25.1	24.9	25.1	25.1
IRAC1	24.1	23.6	23.6	24.7
IRAC2	24.3	23.7	24.2	24.2

Notes. Values have been calculated from the properties of the sample and adopted for the SED fitting described in Sect.. 3.2. Dashes indicate missing filters for a particular cluster.

Spitzer/IRAC channels at 5.8 μm and 8 μm were judged to be too noisy and excluded from the spectral energy distribution (SED) fitting process (see Sect. 3.2). The details of the filters used, and their depths, for each cluster, can be found in Table 2.1. The bright cluster galaxies and intra-cluster light were subtracted by Shipley et al. (2018) for improved photometry of background sources in these very crowded fields. The detection image for each of these clusters was made up of a combination of the F814W, F105W, F125W, F140W and F160W bands (point-spread-function–matched to the F814W band), after the modelling out of the bright cluster galaxies.
The area that MUSE observed for each of these clusters is fully contained within the HST area, so I cut the HST area considered to that of the MUSE data. The resulting effective (lens-corrected) co-volume, derived from LENSTOOL source-plane projections, is 22910 Mpc^3 over the redshift range $2.9 < z < 6.7$.

2.3 JWST photometry : UNCOVER

Towards the end of the first year of my doctoral studies, in July 2022, the first data from the JWST was released, including the now-famous image of the SMACS0723 lensing cluster [3]. Shortly thereafter, the UNCOVER programme released their data for A2744 (Bezanson et al. 2022; Weaver et al. 2023), a lensing cluster already well studied by MUSE and included in the original sample from Goovaerts et al. (2023). This represented an opportunity to extend the analysis of the 121 individual LAEs in the A2744 lensing cluster, further than what was achievable with HST imaging. Here then, are the details of the JWST photometry used to derive further LAE properties for the LAEs in the A2744 lensing cluster (Goovaerts et al. 2024). I note that this sample of LAEs in A2744 is slightly different from the sample in Goovaerts et al. (2023) and which is described above, due to the demands of the photometry and the science I wanted to do with the data. The photometry used comes from the UNCOVER treasury survey (Bezanson et al. 2022). The photometric catalogs themselves are described in Weaver et al. (2023); Kokorev et al. (2022) [4]. This survey combines HST data from the F435W, F606W, F814W, F105W, F115W, F125W, F140W and F160W filters with NIRCam data from the F090W, F150W, F200W, F277W, F356W, F410M and F444W bands. This gives excellent coverage from 15 bands between 400 nm and 4.5 μm. I note that this region was previously covered by the data from the IRAC instrument on the Spitzer Space Telescope (as mentioned in the previous section), however the resolution and sensitivity of the JWST makes it vastly more powerful for the purpose of detecting and characterising high-redshift galaxies, especially in crowded fields such as lensing clusters.

Weaver et al. (2023) subtract the bright cluster galaxies (BCGs) and intra-cluster light (ICL) in order to better detect faint galaxies. The detection is then performed on a combination of the F277W, F356W, and F444W bands, PSF (point spread function)-matched to the F444W band. Two photometric catalogs are created with a 0.32″-aperture catalog being optimised for faint, compact sources.

Of the 154 images of MUSE LAEs in the MUSE field of view, 121 images were detected in the UNCOVER photometry, of 99 individual LAEs. Due to the extended nature of some lensed LAEs, they were identified as two continuum objects. In this case, I combined the fluxes of the continuum objects. This happened in seven cases. In two cases, I rejected the continuum associated to an LAE as it was clearly coming from a BCG. Ultimately, I chose a representative for each multiple image system with the least contamination possible. I removed one more object as it is extremely highly magnified (magnification factor 135 ± 1500), meaning that the uncertainty on the derived SFR and stellar mass would be too great. 96 individual LAEs remained in the sample. It is these 96 LAEs from which are derived the results presented in Section 3.3.2.

3. https://www.nasa.gov/image-article/nasas-webb-delivers-deepest-infrared-image-of-universe-yet/
4. https://jwst-uncover.github.io

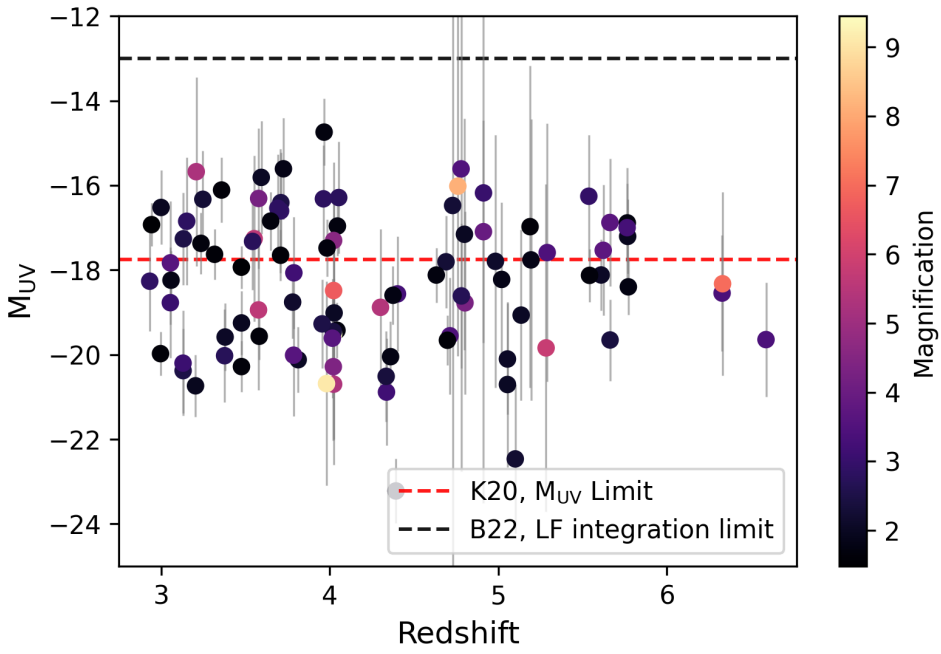

FIGURE 2.1 – The 96 individual LAEs with JWST imaging used in this study, distributed in redshift and absolute UV magnitude, colour-coded by lensing magnification. Redshifts quoted are spectroscopic, from MUSE, and magnitude values are derived from the filter that covers the rest frame 1500 Å emission. These are corrected for lensing magnification, as are the uncertainties. Horizontal dashed lines denote relevant limits : red denotes the M_{UV} limit in an equivalent blank field study (Kusakabe et al. 2020) and black denotes the integration limit used when calculating the star formation rate density from the UV luminosity function (LF) in the latest study (Bouwens et al. 2022).

2.4 Lens models and source magnifications

Magnifications of sources in the lensing clusters used in this work were assigned with the use of the parametric mass distribution models in Richard et al. (2021) (for A2744, A370 and M0416, for AS1063, the lens model comes from Beauchesne et al. 2024) and the LENSTOOL software (Kneib et al. 1996; Jullo et al. 2007; Jullo &Kneib 2009; Kneib et al. 2011). These models are well constrained by the large number of multiple images with secure spectroscopic redshifts in these clusters. Richard et al. (2021) estimated a typical statistical error of 1% of the mass profile of these clusters. The models in turn give the magnifications of the sources used in this study, which range from 0.8 (de-magnified) up to 137. Most sources have magnifications between 1.5 and 25. While these lensing models are well understood and benefit from many multiple image systems as constraints, small systematic uncertainties related to the lens model used can still persist due to the particular choice of mass distribution (see, for example, Meneghetti et al. 2017; Acebron et al. 2017, 2018; Furtak et al. 2021).

The LAEs in the A2744 lensing cluster, which benefit from NIRCam imaging, have a magnification factor range of 1.5 to 9.5 and a sample average magnification of 3. The resultant Lyman-α luminosities probed are in the range $40 < \log_{10}(L_{Ly\alpha}/\mathrm{erg\,s^{-1}}) < 43$. The UV-magnitude range is $-23 \lesssim M_{UV} \lesssim -14$, where this value was derived from the filter closest to the 1500 Å rest frame emission, in the same way as described in the previous section. The redshift and absolute magnitude distribution is displayed for the 96 LAEs in Fig. 2.1, colour-coded by the lensing magnification of each galaxy. We can see from this plot that the sample populates a large part of the M_{UV} space between a current blank field limit for a similar study of LAEs in the literature (Kusakabe et al. 2020) and the typical integration limit applied to the UV luminosity function when calculating the total star formation rate density : the operative quantity when considering whether a population can reionise the neutral IGM and hence of great relevance for this study (Bouwens et al. 2022).

3 Properties of high-redshift, gravitationally lensed, star-forming galaxies

Galaxies are made of stars.

— *My supervisor, Roser Pello, often.*

Author's note on content : *This chapter contains sections from my first and second paper pertaining to the properties of intrinsically faint LAEs and LBGs detected by MUSE (LAEs), HST and JWST (LAEs and LBGs). The first paper of my thesis, Goovaerts et al. (2023), had a large section covering these properties, despite not being the main idea behind my first project. We will return to this main idea, the LAE fraction, in the following chapter.*
The combination of these sections of my first paper with the entirety of my second paper (Goovaerts et al. 2024) is natural as this paper simply extends what we know about the properties of these objects with new JWST data.

Author's note on context : *The first project of my PhD, the result of which is Goovaerts et al. (2023), was pre-determined at the start of my PhD, and represented an extension of the earlier work of Roser's previous PhD student (de La Vieuville et al. 2020). I spent a great deal of time getting to grips with the many aspects of this work, going from never having handled UV and optical data, or spectroscopy, or studied (properly) the physics of galaxies, to using photometric redshift and SED fitting tools, gravitational lens modelling tools and interpreting the results in the context of galactic astrophysics. The time was well spent however, as the skills acquired and codes developed were used extensively for the next three years.*

3.1 Introduction

This chapter presents the results of Goovaerts et al. (2023) and Goovaerts et al. (2024) on the properties of high-redshift, lensed, LAEs derived from HST and JWST imaging. The particular goals were to assess what kinds of galaxies are producing Lyman-α radiation in these intrinsically faint regimes and therefore draw conclusions as to what effect these galaxies might have on reionisation.
As we saw in Chapter 1, LAEs are typically dust-poor, young, highly star-forming galaxies, with this being especially true of intrinsically faint, low-mass LAEs. However, continuing

to investigate these galaxies at fainter regimes, lower masses and higher redshifts is crucial for the continuing investigation into the contributors to cosmic reionisation.
In this work, therefore, I sought to derive physical properties for the LAE samples presented in the previous chapter and compare them to the UV-selected population : SFRs, UV slopes (denoted by β) and stellar masses. I compared these properties to the Lyman-α emission parameters for the LAEs and established trends.
It is important to use large samples of faint LAEs for this goal as there is significant variation in galaxy properties among the LAE population. General, well-informed trends however, can help us to understand not only what kind of galaxies are selected as LAEs but what the role of these particular galaxies is for reionisation. The strongest LAEs (i.e. those with the highest values of $EW_{Ly\alpha}$) are typically UV-faint, with blue UV slopes, indicating a lack of dust and a young stellar population (De Barros et al. 2017; Sobral et al. 2018; Runnholm et al. 2020; Matthee et al. 2021; Iani et al. 2023). Many ionising photons are produced by these highly star-forming systems, creating Lyman-α photons which then escape more easily than from older, dustier, more chemically evolved galaxies (Atek et al. 2008; Verhamme et al. 2008; Hayes et al. 2011; Matthee et al. 2016b; Sobral &Matthee 2019; Runnholm et al. 2020; Lin et al. 2024).
The stellar masses and SFRs of these galaxies, and hence their position on the main sequence of star formation (henceforth MS) is particularly interesting in the context of their impact on reionisation. The MS (at low masses) is a linear and typically tight ($\sim$ 0.3 dex) relation between the stellar mass and star formation rate of galaxies. The position of galaxies on the MS gives an indication of what kind of star formation a given galaxy is undergoing. A galaxy residing above the typical MS is a starburst galaxy and a galaxy residing below the typical MS is a quenched galaxy with little to no ongoing star formation.
Between $10^8 < M_\star/M_\odot < 10^{12}$ and $0 < z < 6$, the MS is well understood, even taking into account calibrations between different studies related to the selected initial mass function (IMF), cosmology, selection biases, and SFR indicator (see the reviews of Speagle et al. 2014 (S14) and Popesso et al. 2023 (P23) primarily, as well as Brinchmann et al. 2004; Daddi et al. 2007; Elbaz et al. 2007; Santini et al. 2009; Elbaz et al. 2011; Sobral et al. 2014; Steinhardt et al. 2014). In S14, a time (or, equivalently, redshift)-dependent form of the MS was suggested. The authors found that the normalisation and slope of the MS decrease with increasing time (decreasing redshift). This result was also found in the review of P23.
Previous studies have made it possible to study the low-mass end of the galaxy MS, using lensing, such as Santini et al. (2009, 2017) and at low redshift, such as Boogaard et al. (2018). However, such high-redshift studies have relied on *Spitzer/IRAC* for their coverage past 1600 Å. More recently, Looser et al. (2023), based on a sample of 200 galaxies observed with JWST/NIRSpec, included estimations of the MS relation down to a very low mass range ($\sim 10^6\,M_\odot$), in redshift ranges of $2 < z < 5$ and $5 < z < 11$. They found the galaxies to be located well above the best estimations of the MS at these redshifts and masses. This study, as well as those of Atek et al. (2023) and Maseda et al. (2023), clearly demonstrate the capability of JWST/NIRCam and JWST/NIRSpec to probe extremely low masses at these high redshifts (down to $\log(M_\star/M_\odot) \sim 5.9$ for Atek et al. 2023).

Section 3.2 describes the photometric redshift estimation and SED fitting of the HST data in the Hubble Frontier Fields. Section 3.2.1 covers the more in-depth SED fitting using `CIGALE` for those LAEs in the A2744 field with JWST/NIRCam data. Section 3.3.1 details the results derived from the HST data while Section 3.3.2 gives the results on the star-forming main sequence derived with JWST data. Finally, Section 3.4 provides a summary and a discussion of the results in the context of cosmic reionisation.

3.2 SED fitting and redshift estimation

I calculated photometric redshifts and probability distributions (hereafter $P(z)$) in order to perform the LBG selection. I used the package New-Hyperz (Bolzonella et al. 2000) to estimate redshifts and probability distributions. This package uses a standard χ^2 minimisation technique to fit template galaxy SEDs to photometric data points. It has been optimised for the redshift determination of high-redshift galaxies so is ideal for my purpose. I used a suite of template spectra to fit the photometric data : the four template spectra from Coleman et al. (1980), two Starburst99 models with nebular emission lines [1] (Leitherer et al. 1999) : a single burst model and a constant SFR model (where each spans five metallicities and 37 stellar population ages), and seven models adapted from Bruzual &Charlot (2003). Included in these seven were a star formation burst model, five exponentially decaying models with timescales between 1 and 30 Gyr and a constant star formation model. The redshift range I used in New-Hyperz is 0 to 8 with a step in redshift of 0.03. The Calzetti extinction law (Calzetti et al. 2000) was used to account for internal extinction with values of A_v allowed to vary between 0 and 1.5 magnitudes. No priors on galaxy luminosity were introduced during this process, avoiding any bias introduced by lensing magnification.

For a galaxy to be included in the LBG sample for this study, the criteria were as follows. The best solution for the photometric redshift must lie in the range $2.9 < z < 6.7$. I also accepted any candidates not in this range that had 1σ errors overlapping with it. In practice, this accounts for just 14 objects. To make sure the detection was real, I also demanded a 5σ detection in at least one HST filter. New-Hyperz provides a redshift probability distribution, P (z), which can have several peaks, in which case there are degenerated solutions for that particular galaxy. I accepted galaxies into the sample if only one of the peaks was in the required range, as long as 60% of the integrated $P(z)$ was also located in this range. It is subsequently important to assess the quality of this process by comparing the photometric redshift results for those objects also selected as LAEs to the spectroscopic redshift determined from the peak of the Lyman-α emission. Figure 3.1 shows this comparison. The dashed lines indicate regions constrained by $|z_{spec} - z_{phot}| < 0.15(1 + z_{spec})$ and $|z_{spec} - z_{phot}| < 0.05(1 + z_{spec})$. The apparent magnitude in the F125W filter is encoded in the colour bar to demonstrate that the instances in which New-Hyperz performs poorly (i.e. instances outside of the outer region specified above) tend to be fainter objects with magnitudes $\gtrsim 28$.

Finally, I manually inspected the LBG sample using the HST images, photometry, SED

1. Nebular emission lines except Lyman-α, as this is too difficult to model. I subtracted the Lyman-α fluxes from the filters that saw this emission to compensate.

TABLE 3.1 – Details of each lensing cluster used in this study.

Cluster	RA	Dec.	z	MUSE Exposure Time (Hrs)	Co-volume (Mpc^3)	LAE-only	LBG-only	LAE + LBG	LAE + continuum
A2744	00 :14 :20.702	-30 :24 :00.63	0.308	3.5-7	10500	24	294	47	50
A370	02 :29 :53.122	-01 :34 :56.14	0.375	1.5-8.5	5350	8	267	20	14
AS1063	22 :48 :43.975	-26 :05 :08.00	0.348	3.9	1970	6	159	7	8
M0416S	04 :16 :09.144	-24 :04 :02.95	0.397	11-15	1670	4	81	14	16
M0416N	04 :16 :09.144	-24 :04 :02.95	0.397	17	3420	13	71	12	20
Total					22910	55	872	100	108

Notes. Details of each lensing cluster used in this study, among which the number of each galaxy group identified in each cluster (see text). The different exposure times for three of the clusters come from the range of exposure times for different MUSE pointings for these clusters.

fitting from New-Hyperz and the LENSTOOL package with the lens models described in Sect. 2.4. This procedure was designed to identify multiple images in the LBG sample caused by the gravitational lensing, as well as to remove any obvious spurious detections ; regions of noise or contamination erroneously selected as LBGs. Multiple images were identified using a combination of LENSTOOL predictions, redshift determinations and SEDs from New-Hyperz, and visual inspection of the HST images. LENSTOOL predictions, redshift estimates and colours of objects had to match for those objects to be designated a multiple image system. The colours used were F814W − F606W, F105W − F814W, F140W − F105W, all of which had to match to within 2σ for the objects in question to be designated multiple images. From each system, a representative LBG image was chosen. This image was the least contaminated, or, in the case of a match with an LAE multiple image system, the image chosen to represent the LBG multiple system matched the selected LAE image.
Fig. 3.2 shows the properties of the LAE sample in red and UV-selected galaxies in blue. In order to have a similar derivation of M_{UV} for all the LAEs, regardless of detection in HST photometry, values of M_{UV} were calculated from the filter closest to the 1500 Å rest frame wavelength (where available, and the 2σ upper limit of the continuum taken from this filter where not), and corrected for magnification.
Having blindly selected the LAE and LBG samples, I compared them, using a matching radius of 0″.5, to see which objects are selected as both. The results are shown in Table 3.1. I selected a population labelled LAE+continuum, which denotes objects that are selected

as LAEs, for which a continuum was seen in the HST images, but where this continuum failed to meet the selection criteria for the LBG sample. Mostly, these galaxies failed on the S/N criteria, indicating a faint continuum or a noisy area in the HST images. Nevertheless, I kept these objects as, thanks to the detection of Lyman-α emission, there is likely to be a real galaxy at these positions. In the previous work of this nature solely on A2744, de La Vieuville et al. (2020) simply included these objects in the LAE+LBG sample, relaxing the signal-to-noise criterion for these objects, seeing as the presence of an object (as well as its redshift) was known thanks to the Lyman-α emission. In this study, however, I kept the distinction between these continuum detections with Lyman-α emission and the LBGs in the sample that fulfil all the criteria laid out in the previous subsection. Details on the inclusion of this sample in the analysis of the LAE fraction, X_{LAE}, are given in the following chapter where these results are addressed.

For the LAEs, a 'best' image was chosen, a process described fully in Thai et al. (2023). Representative images were chosen with minimal impact by neighbours and with high signal-to-noise and moderate magnification. As mentioned above, when selecting LBGs, I kept the image corresponding to the best LAE image selected by Thai et al. (2023) where possible. However, in some cases I chose another image, because that particular LAE image was selected as LBG rather than continuum only. I ensured that the image chosen was always of similar quality. A modification of this nature was rare and I imposed it in fewer than ten systems across the whole LAE sample. The original Lyman-α flux and magnification of the source, as given in the LLAMAS catalogues, was used for the analysis on the properties of these objects ; however, their designation as LAE+continuum or LAE+LBG changed based on this.

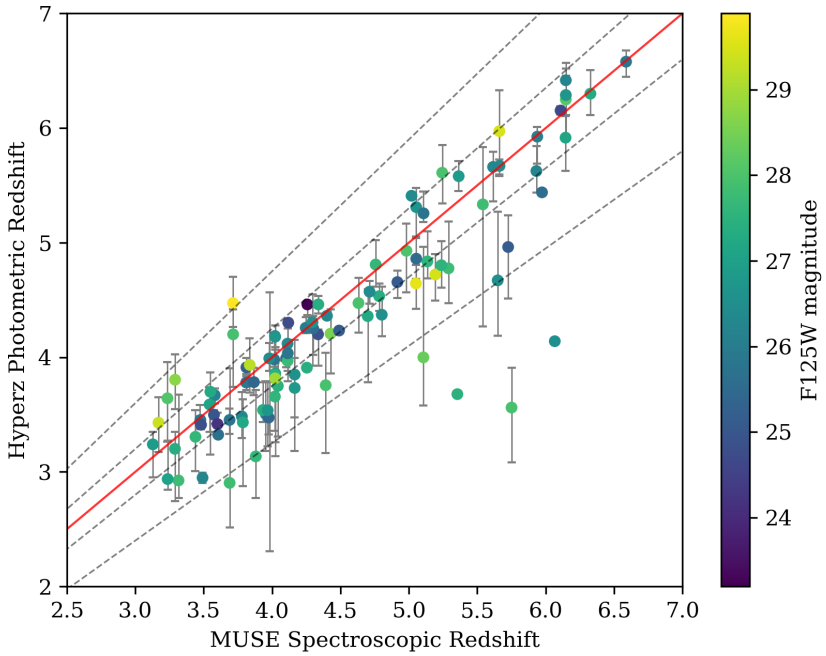

FIGURE 3.1 – Photometric vs spectroscopic redshift comparison of objects selected as both LAEs and LBGs. The red line indicates the one-to-one relation, and the dashed black lines indicate the typical error bounds of $|z_{spec} - z_{phot}| < 0.15(1 + z_{spec})$ and $|z_{spec} - z_{phot}| < 0.05(1 + z_{spec})$. Almost all of the photometric redshifts agree with their spectroscopic equivalents within the outer of these two bounds. Those that do not tend to be fainter objects, with magnitudes of 28 and above.

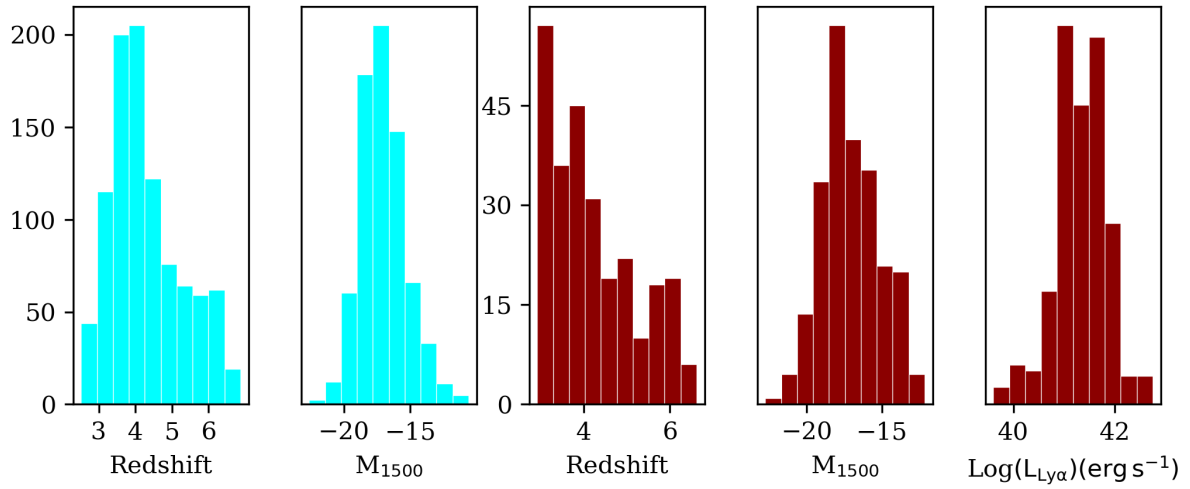

FIGURE 3.2 – Redshift and M_{UV} (and Lyman-α luminosity for the LAEs) distributions of the two samples used in this work. LBGs are shown in blue and LAEs in red.

3.2.1 SED fitting with CIGALE

For the 96 LAEs detected in the UNCOVER photometry from NIRCam, with which I sought to derive stellar masses, as the redshifts of these galaxies were precisely known, I chose to use the SED fitting code CIGALE in order to make use of the wide variety of star-formation histories (SFHs), models for dust absorption and stellar emission, as well as wide range of output parameters provided. The details of these models is are given below.

CIGALE (Code Investigating GALaxy Emission) (Boquien et al. 2019) is a python code [2] designed to extract galaxy properties from photometric and spectroscopic observations ranging between the far-UV to radio. It takes into account flexible star formation histories (SFHs), nebular emission and different dust attenuation models. I fit the observed photometry of all the JWST-detected LAE images in A2744 (121 out of 154). I took advantage of the accurately known, secure spectroscopic redshifts available for these LAEs, fixing these values in CIGALE. I also subtracted Lyman-α fluxes from the filters that see them so they do not contaminate the photometry.

I investigated two different star-formation histories (SFHs), a single exponentially decaying burst and a double burst model with an initial burst of star formation followed by a second, delayed burst (Małek et al. 2018; Boquien et al. 2019). A range of ages were taken into account in both models, from $10 - 700$ Myr. Mass fractions for the delayed burst ranged from 0.001 to 0.65. The best-fit of these two SFHs was carried forward for analysis. I used the stellar library of Bruzual &Charlot (2003) with five metallicities ranging between 0.0001 and 0.02. I took into account nebular emission as some high-redshift galaxies can exhibit strong nebular lines (Maseda et al. 2020b; Schaerer et al. 2022; Matthee et al. 2023; Brinchmann 2023). The nebular models used by CIGALE [3] (Theulé et al. 2024) were computed using the CLOUDY software Ferland et al. (2017). Gas metallicities used ranged between 0.0004 and 0.02. Dust attenuation was modelled based on the modified starburst attenuation curve from Calzetti et al. (2000).

CIGALE outputs the required physical parameters of each galaxy, in this case stellar mass, SFR, and the χ^2_ν statistic for each fit. In order to check the consistency of these results and the reliability of the CIGALE fitting, I used CIGALE's mock_flag function to generate mock results with simulated noise, to which I compared the actual results in order to assess how reliably this process estimated parameters such as the mass and SFR. In Goovaerts et al. (2024), these details were included as an appendix. Due to the prevalence of SED fitting among all the work on which I spent time, I include it here in the main body of text.

First, I depict in Fig. 3.3 the comparison (in terms of resulting age, stellar mass, SFR and χ^2_ν), between the two SFHs used in the CIGALE fitting. The best-fit SFH was chosen moving forward to the rest of the work. The graphs depicting stellar mass and SFR demonstrate how robust the SED fitting process is to changes in SFH. Particularly the stellar mass changes very little between SFHs. This has already been noted by Pozzetti et al. (2010); Bolzonella et al. (2010); Lee et al. (2010); Ciesla et al. (2017) among others, however, see also Buat et al. (2014). I note that the addition of NIRCam data into the near-infrared helps mass determination at these redshifts significantly compared to previously available

2. https://cigale.lam.fr
3. Once again, the Lyman-α emission line was not included.

data.
The SFR exhibits a higher dispersion when comparing the two SFHs, however, there is no significant offset. This greater dispersion in the SED-derived SFR is expected, see the above references, as well as Mercier et al. (2022). This comes from the lack of data in the rest frame mid and far infrared, which would be useful to constrain the dust content of these galaxies (although it is expected to be limited De Barros et al. 2017; Goovaerts et al. 2023).
A further check on the reliability of galaxy parameter estimation was performed using `CIGALE`'s mock catalog function. This is a self-consistency check on derived physical parameters, inbuilt within `CIGALE`, which uses the best-fit parameters as truth values, creating an artificial catalog to which noise, drawn from the observed uncertainties, is added. These artificial observations then undergo the same fitting process as the actual observations, and a comparison of the artificial and best-fit parameters gives an indication of how well the physical quantities are retrieved. This comparison is shown in Fig. 3.4.
Altogether, these tests show that `CIGALE` can reliably recover the relevant physical parameters of the LAEs for the estimation of the MS relation.

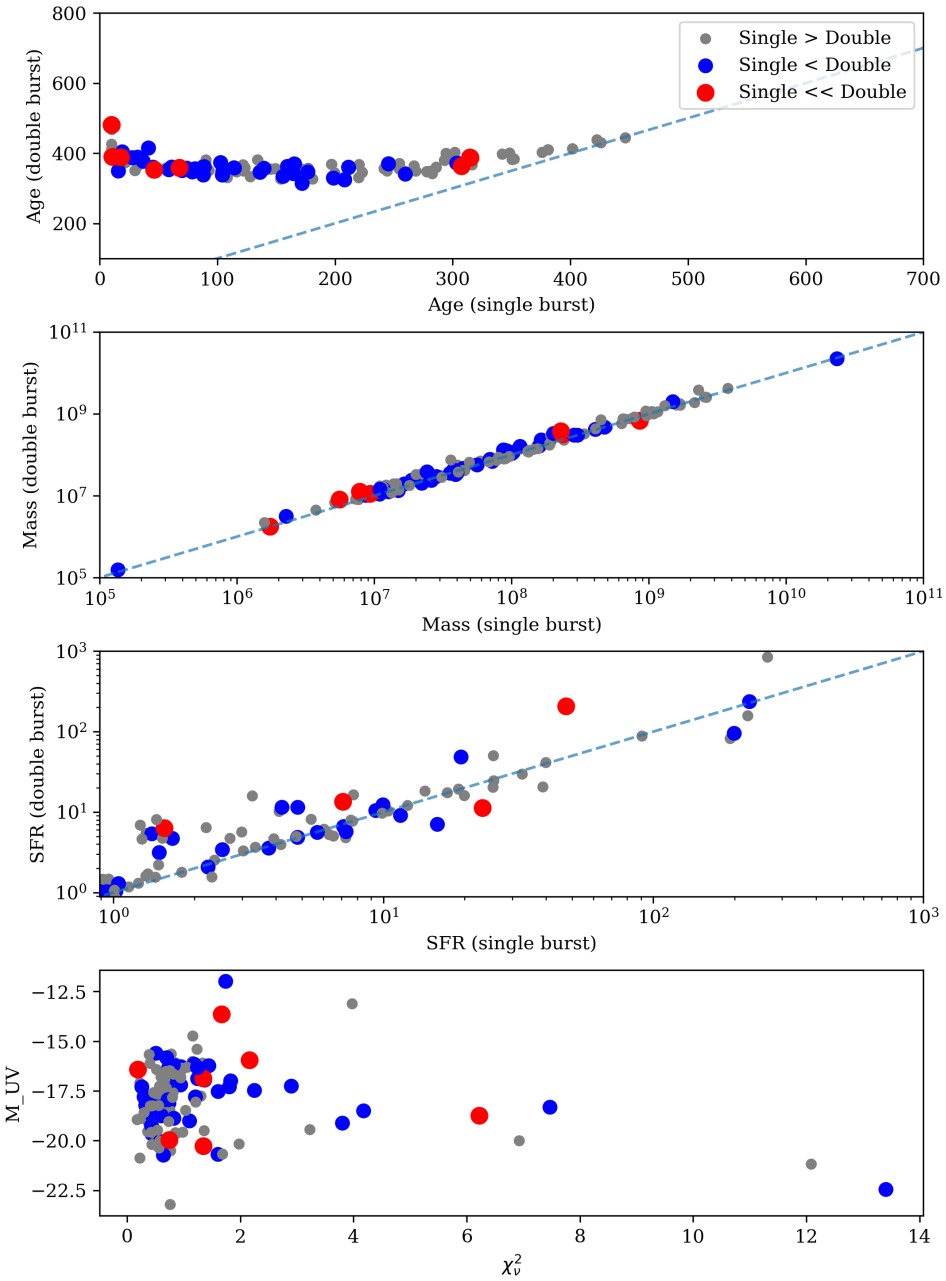

FIGURE 3.3 – Comparison of the two SFHs used in the `CIGALE` fitting process : the single burst model (x-axis) and the double burst model (y-axis). These graphs include the highly-magnified object described in the main text and removed from the MS fitting. In descending order, the graphs depict the comparison of the age of the main stellar population [4], the stellar mass, the SFR and the χ^2_ν statistic. Grey dots indicate galaxies for which the single burst model is a better fit and coloured dots indicate galaxies for which the double burst model is better. Red dots indicate galaxies for which the double burst model is significantly better than the single burst model. Error bars on these values are described in the caption of Fig. 3.11.

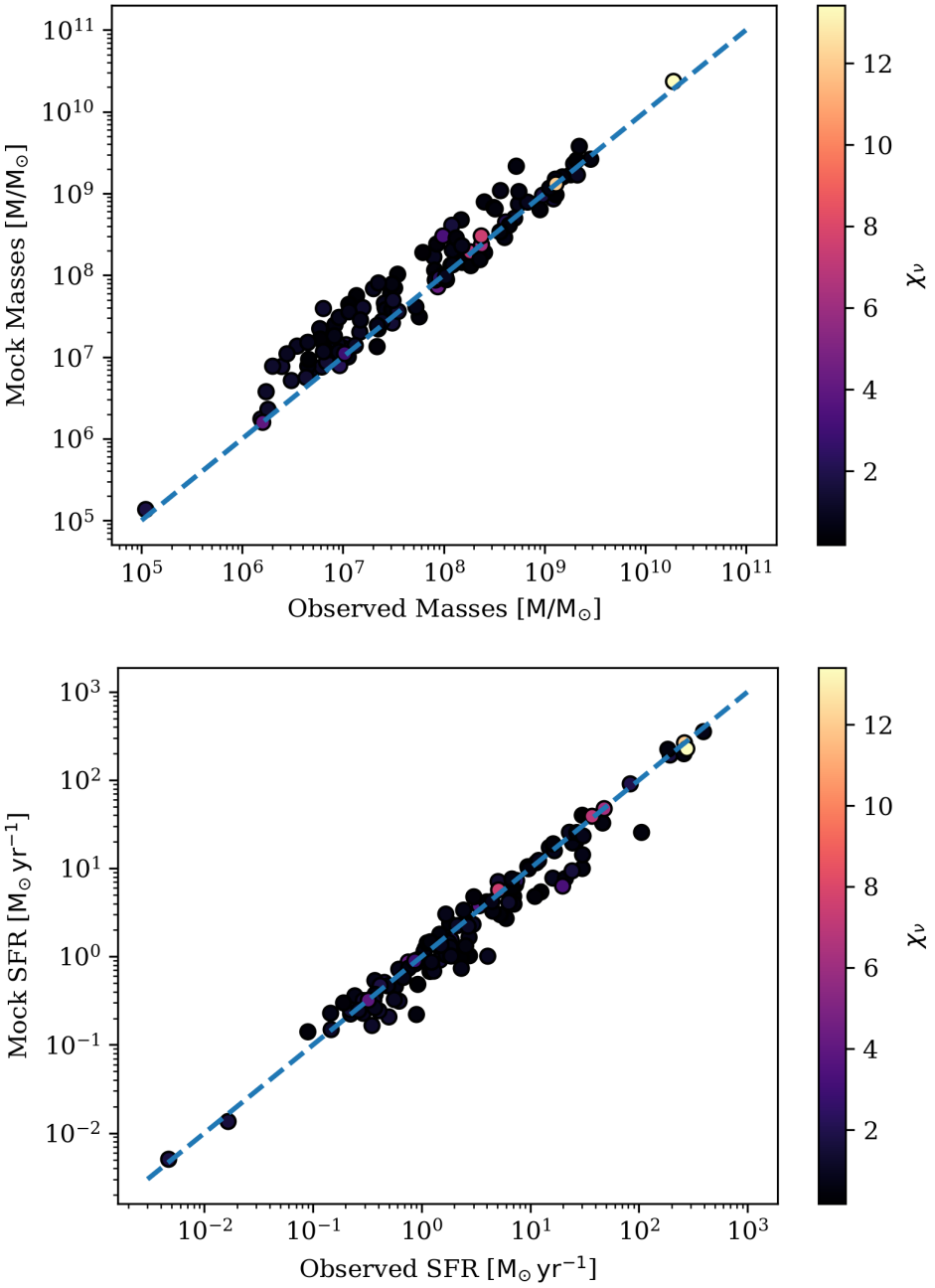

FIGURE 3.4 – The results of the mock catalog creation and fitting.
Upper : Comparison of observed and mock stellar masses, colour-coded by the χ^2_ν statistic of the original, observed fit.
Lower : Comparison of observed and mock SFRs, colour-coded by the χ^2_ν statistic of the original, observed fit.

3.3 Results : LAE properties

I now move on to describing the first of the results presented in this thesis. The following sections will provide the details of the properties I derived from HST and JWST photometry for the samples of high-redshift LAEs and LBGs.

3.3.1 Results : HST-derived properties

In order to ascertain the similarities and differences between the populations of high-redshift galaxies, it is useful to look at the physical properties I derived from the HST photometry and their relation to Lyman-α emission. This can also help disseminate how these properties tie in with the LAE fraction (see Sect. 4.2). Additionally, one can appraise any differences from the established trends for these high-redshift galaxies that may appear in this sample of faint, lensed galaxies.
To evaluate this relation to Lyman-α emission, the Lyman-α equivalent width, $\mathrm{EW}_{\mathrm{Ly}\alpha}$, is an important property to derive. This can then be compared to UV-derived properties. In order to calculate $\mathrm{EW}_{\mathrm{Ly}\alpha}$, first I derived UV slopes by fitting the photometric points starting above the location of the Lyman-α emission (irrespective of whether or not it is detected for a given galaxy) and including all the filters up to 2600 Å in the rest-frame, adapting the approach used in Castellano et al. (2012); Schenker et al. (2014); Bouwens et al. (2015a). I fitted a power law, $F_\lambda \propto \lambda^\beta$, where β is the UV slope, to the photometry. I chose this method as it does not rely on SED fitting with a set of templates that have specific allowed values of β (Austin et al. 2024 provide a nice discussion on the comparison of these methods).
Subsequently, by using this photometrically fitted UV slope for each object, I ascertained the continuum flux level beneath the Lyman-α emission. I then calculated $\mathrm{EW}_{\mathrm{Ly}\alpha}$ by dividing the Lyman-α flux by the continuum flux level, corrected to its rest-frame level. In this process I took into account the error on the UV slope resulting from the fitting process, as well as the error associated with the Lyman-α flux.
For the objects with no associated continuum, the upper limits of the continuum were taken from the filter closest to the 1500 Å rest-frame emission. For the objects with no associated Lyman-α emission, the detection limits of the Lyman-α emission were used.

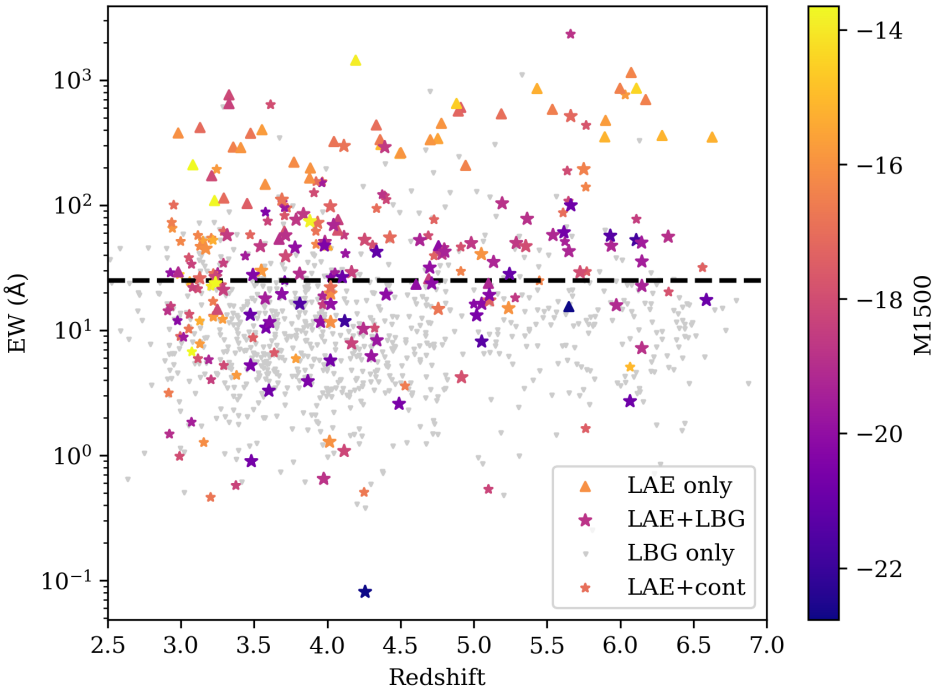

FIGURE 3.5 – Lyman-α EW ($EW_{Ly\alpha}$) distribution for all the galaxy samples. Objects selected as LAEs and LBGs are denoted by larger stars, LAE+continuum by smaller stars, LAE-only by upward pointing triangles, and LBG-only by downward pointing triangles. $EW_{Ly\alpha}$ values for the latter two populations were calculated using the upper limits of the continuum and Lyman-α flux, respectively. The objects are colour-coded by M_{UV}. The horizontal dashed line demarcates the 25 Å level, above which LAEs are included in the calculation of the LAE fraction. Error bars are omitted for clarity, but shown in Figs. 3.6 and 3.7.

The EW distribution with redshift for all the sample is shown in Fig. 3.5. The dashed black line denotes the typical EW inclusion limit for objects to the calculation of X_{LAE} (see Section 4.2). The percentage of objects above this limit is 44% and 50% for LAE+LBG objects and LAE+continuum objects, respectively. This is to be expected as the objects selected as continuum but not LBG are in general fainter, giving rise to higher values of $EW_{Ly\alpha}$.

Fig. 3.6 compares $EW_{Ly\alpha}$ to UV magnitude for the LAE+LBG sample. A rise is seen in $EW_{Ly\alpha}$ towards fainter M_{UV}, in agreement with results reported in Stark et al. (2010); De Barros et al. (2017); Kusakabe et al. (2020). I note that above $M_{UV} = -16$ this graph is populated by high EW, continuum-undetected LAEs (shown by orange triangles). I did not include these objects in the binned averages as they are not LBGs and the continuum values are estimated upper limits ; however, these objects indicate that this trend in EW likely increases to even fainter magnitudes than is populated by the current LBG selection. As the spatial extent of Lyman-α emission correlates with the size of the galaxy and hence M_{UV} (Wisotzki et al. 2016; Leclercq et al. 2017; Claeyssens et al. 2022) the trend in

Fig. 3.6 is often seen as a natural result.
I also compared $EW_{Ly\alpha}$ to the UV slope (Fig. 3.7). In general, high-EW LAEs are found to have bluer slopes (Stark et al. 2010; Schenker et al. 2014; De Barros et al. 2017). I report a slight increase ($< 1\sigma$) in average EW in bins between $\beta = -1.0$ and $\beta = -3.0$. However, similarly to De Barros et al. (2017), I found $EW_{Ly\alpha}$ values as high as ~ 100 Å across the sample.

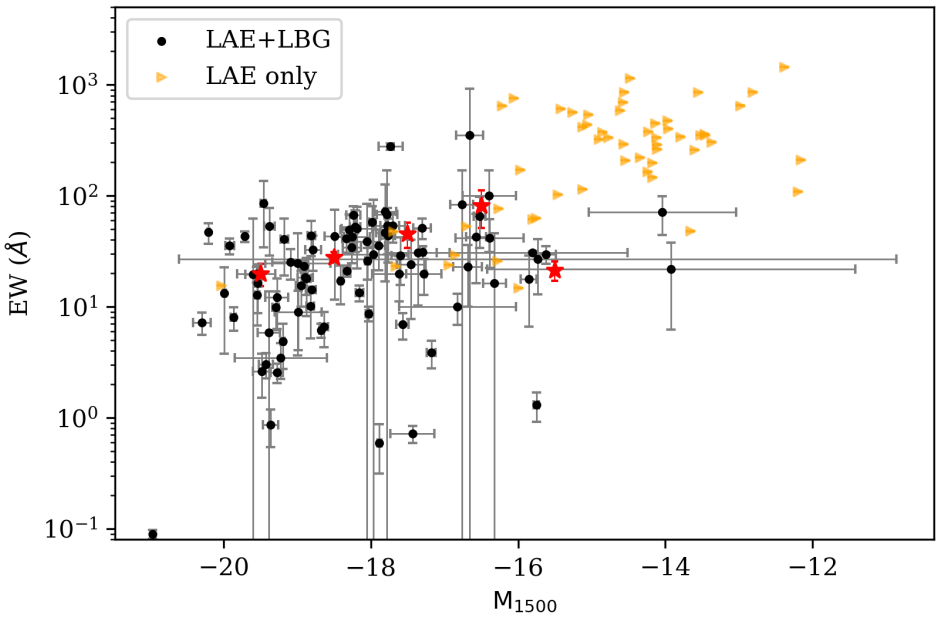

FIGURE 3.6 – $EW_{Ly\alpha}$ distribution over the range of UV absolute magnitude probed for the LAE+LBG sample. The red stars indicate the average in five equal-size bins between $M_{UV} = -20$ and $M_{UV} = -15$, the region that is well populated. De Barros et al. (2017) provide a similar plot (at $z = 6$) for a brighter sample with a similar rising average $EW_{Ly\alpha}$. This plot extends several magnitudes fainter ; this trend continues down to at least $M_{UV} = -16$. An idea of the region fainter than $M_{UV} = -15$ can be gained by including the LAE-only sample (orange triangles), the vast majority of which are very faint in UV magnitude, and high-$EW_{Ly\alpha}$ objects. For these objects, EW error bars, coming only from the error on the Lyman-α flux, are smaller than the size of the points. The continuum values used are 2σ upper limits estimated from the filter that would see the emission at 1500 Å rest frame.

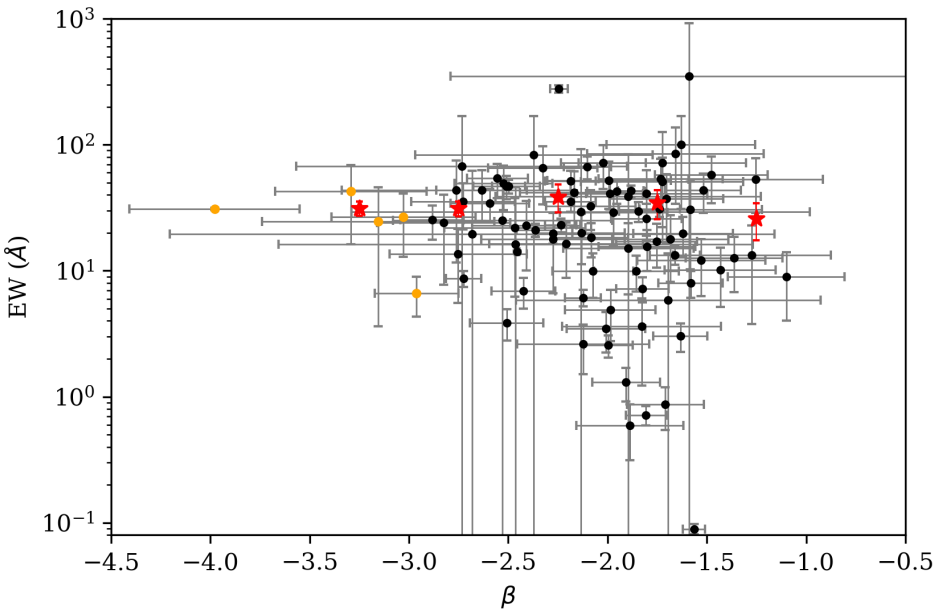

FIGURE 3.7 – UV slope plotted against $EW_{Ly\alpha}$ for the LAE+LBG sample. Orange dots represent UV slopes that, upon inspection, I found to be dubious : photometry that locally did not represent the slope well or had large errors. Red stars represent average values in equally sized bins between $\beta = -3.5$ and $\beta = -1.0$. The change in $EW_{Ly\alpha}$ across this range is not as significant as the change across the range of probed UV magnitudes (see Fig. 3.6) ; however, there is a lightly rising trend in $EW_{Ly\alpha}$ with bluer slopes down to $\beta = -2.5$.

I derived SFRs from Lyman-α ($SFR_{Ly\alpha}$) and from the UV continuum (SFR_{UV}), based on the relations given in Kennicutt (1998a) and the factor of 8.7 between L(Hα) and L(Lyα), assuming a Salpeter IMF (Salpeter 1955) and constant star formation. $SFR_{Ly\alpha}$ is a good lower limit on the intrinsic SFR as Lyman-α flux can be lost due to dust attenuation or a more or less opaque IGM (Zheng et al. 2010; Gronke et al. 2021). However, due to the use of an IFU in this study, slit losses have no impact on the Lyman-α flux.
I compared the two measures of SFR for the LAE+LBG sample in Fig. 3.8, plotting the lines of one to one ratio and the actual median ratio ($SFR_{Ly\alpha}/SFR_{UV}$) found in the sample. This median ratio (0.35), is well below the one to one ratio, indicating that in most cases the escape fraction of UV photons (the fraction of photons at 1500 Å rest frame that escape the galaxy), $f_{esc,UV}$ [5], exceeds that of Lyman-α photons (the fraction of Lyman-α photons that escape the galaxy), $f_{esc,Ly\alpha}$. This is less apparent in UV-fainter objects, where there is a greater fraction above the $f_{esc,UV} = f_{esc,Ly\alpha}$ line. This result is in line with previous findings in Ando et al. (2006); Schaerer et al. (2011) and de La Vieuville et al. (2020). The explanation offered previously by Ando et al. (2006) and de La Vieuville et al. (2020) relates to the likely difference between the UV-bright and UV-faint galaxies.

5. Not to be confused with the escape fraction of ionising photons, which I expand on later, and is denoted $f_{esc,LyC}$.

If the UV-bright galaxies have had more time to evolve than UV-fainter objects, it is likely that they are chemically more complex and have a larger amount of dust. This would decrease the escape of Lyman-α photons and hence result in a smaller measured $SFR_{Ly\alpha}$. I will return to this point having compared the LAE fraction for the UV-bright and UV-faint halves of the sample in Sect. 4.2. The escape fraction of Lyman-α photons is also extensively discussed in Chapter 5.
Subsequently, I compared M_{UV} and SFR_{UV} to the UV slopes of both samples (LBG and LAE+LBG) between $-3.0 < \beta < -1.0$: Fig. 3.9. In this graph, I calculated binned averages as in Figs. 3.6 and 3.7. However, for this plot the averages were computed for bins of equal population. For the LBG-only sample, there is a slight increase in SFR_{UV} with steeper UV slopes, this is to be expected as steeper values of β generally indicate populations that are more intensely star forming.
From the binned averages we can see that for the population also selected as LAEs, the galaxies are distributed towards higher values of SFR_{UV} and steeper UV slopes. This result supports previous findings (in various redshift ranges, as well as in simulations) that LAEs are in general dust-poor and are more intensely star forming than objects only selected as LBGs (Verhamme et al. 2008; Hayes et al. 2011, 2013; Sobral &Matthee 2019; Santos et al. 2020a).

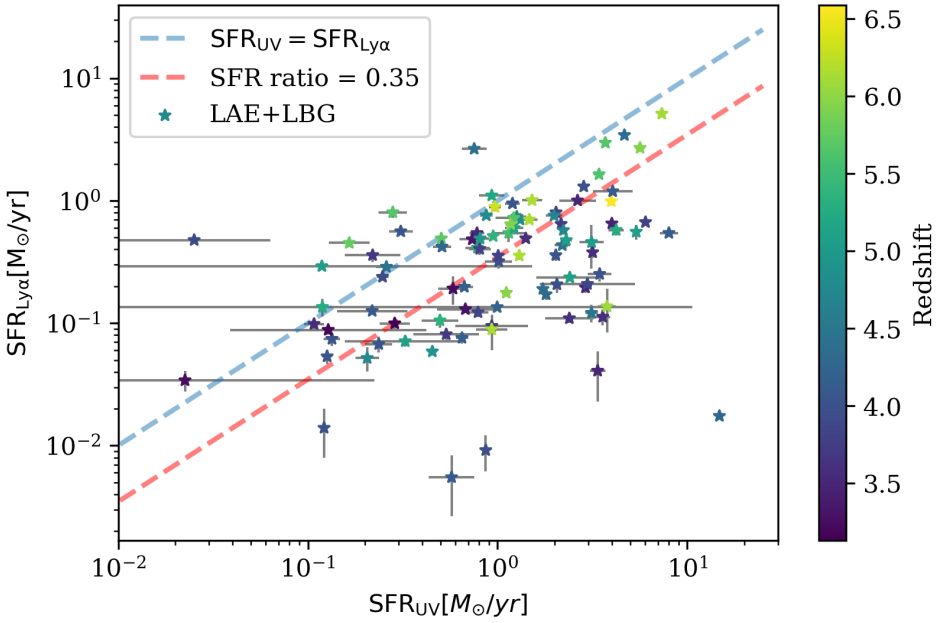

FIGURE 3.8 – Comparison of the derived SFRs for the LAE+LBG sample, colour-coded by redshift. The errors on the $SFR_{Ly\alpha}$ are smaller than the size of the points in most cases. The dashed blue line denotes a one-to-one SFR ratio, i.e. $SFR_{UV} = SFR_{Ly\alpha}$. Galaxies along this line also have equal escape fractions : $f_{esc,UV} = f_{esc,Ly\alpha}$. Most of the sample lies under this line, and the dashed red line denotes the median SFR ratio, 0.35. For fainter objects with $SFR_{UV} < 1\,M_\odot$/yr, a greater fraction lie above the line of equal SFR, a trend previously observed in Ando et al. (2006), Schaerer et al. (2011), and de La Vieuville et al. (2020).

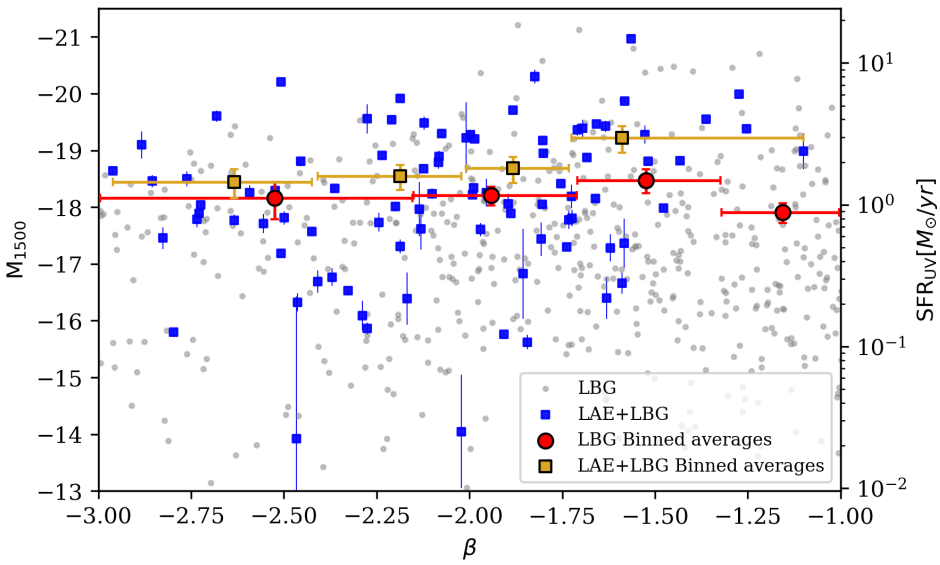

FIGURE 3.9 – M_{UV} and SFR_{UV} vs UV slope. The sample selected as LBG-only is shown in grey, and the LAE+LBG sample is shown in blue. Binned averages in SFR_{UV} for the LBG and LAE+LBG samples are shown with red circles and golden squares, respectively. Each bin contains an equal number of the respective samples, and the horizontal error bars show the width (in terms of β) of each bin. Errors on the LBG-only objects are omitted for readability, and I note that there are LBG-only objects (and four LAE+LBG objects ; see Fig. 3.7) that extend beyond the β limits of this graph ; however, they are objects for which the calculation of the UV slope is uncertain. There are LBG-only objects that extend beyond the M_{UV} limits of the graph, but these are taken into account when computing the binned averages.

3.3.2 Results : JWST-derived properties

With the extra wavelength coverage of the JWST vs the HST, the stellar mass of the LAEs in A2744 can be derived and compared to Lyman-α properties.
Following the analyses of Santos et al. (2020b, 2021) I also assessed the relationship between stellar mass and both Lyman-α luminosity and Lyman-α equivalent width ($EW_{Ly\alpha}$). This can help to evaluate the connection between the host galaxy and its Lyman-α emission. Due to the complicated nature of Lyman-α transfer and escape (Verhamme et al. 2008; Atek et al. 2008; Hayes et al. 2011; Hayes 2015; Leclercq et al. 2017; Gronke et al. 2021; Matthee et al. 2021; Blaizot et al. 2023), many aspects of this connection are still under much discussion. These relationships between stellar mass and Lyman-α parameters are shown in Fig. 3.10.
Fitting a linear relationship between Lyman-α luminosity and stellar mass for the 96 LAEs, I found $\log(M_\star/M_\odot) = (0.85 \pm 0.17)\log(L_{Ly\alpha}/\mathrm{ergs}^{-1}) - (27.8 \pm 6.4)$. This result has a large dispersion but is in rough agreement with that in Santos et al. (2021) (albeit with a lower slope and normalisation), which is especially interesting as the 4000 SC4K LAEs in that study are in a Lyman-α luminosity range of $42.5 \lesssim \log(L_{Ly\alpha})(\mathrm{erg\,s}^{-1}) \lesssim 44$;

therefore, they are far brighter than the sample I used. This result suggests that this relationship holds down to intrinsically faint LAEs : when a galaxy displays Lyman-α emission, the connection between the stellar mass of the galaxies and the amount of Lyman-α luminosity they emit remains roughly constant across all currently-accessible luminosities. However, there is significant scatter in the data, which is to be expected, and indicative of the wide variety of conditions within galaxies affecting Lyman-α escape. If a given galaxy lies far above this best-fit relation (blue dashed line in Fig. 3.10), it is emitting far less Lyman-α emission than expected for a galaxy of its mass. This likely indicates other factors at play, such as higher dust content or specific viewing angles (Verhamme et al. 2008; Atek et al. 2008; Hayes et al. 2013; Blaizot et al. 2023; Chen et al. 2023). Given the dispersion in the left panel of Fig. 3.10, these are clearly important effects. For example, the object at $L_{Ly\alpha} \sim 10^{40}\,\mathrm{erg\,s^{-1}}$ lies $\sim 3\sigma$ away from the best fit relation, indicating that some property of this galaxy prevents the escape of Lyman-α photons more than usual for LAEs at this redshift and mass range. Estimating the dust content and extinction from data taken at longer wavelengths could help to shed more light on this issue.

When comparing $EW_{Ly\alpha}$ with the stellar mass, I found a linear relationship that takes the following form : $\log(M_\star/M_\odot) = (-0.62 \pm 0.07)\log(EW_{Ly\alpha}) + (9.1 \pm 0.1)$. This is a tighter relationship than is seen for the luminosity, which is unsurprising as the UV magnitude used to calculate $EW_{Ly\alpha}$ is tightly correlated with the stellar mass (Duncan et al. 2014; Santini et al. 2023). This suggests that Lyman-α photons struggle more to escape galaxies of higher mass. This is likely due to the higher dust content in galaxies of higher masses (Zahid et al. 2013; Calura et al. 2017; Donevski et al. 2020). While this relation is tighter than that between stellar mass and luminosity, a dispersion is still evident around the best-fit relation. This indicates that for a given mass, a range of Lyman-α escape scenarios are possible. A more complete study on these relations requires larger samples of lensed galaxies which can be binned in terms of stellar mass.

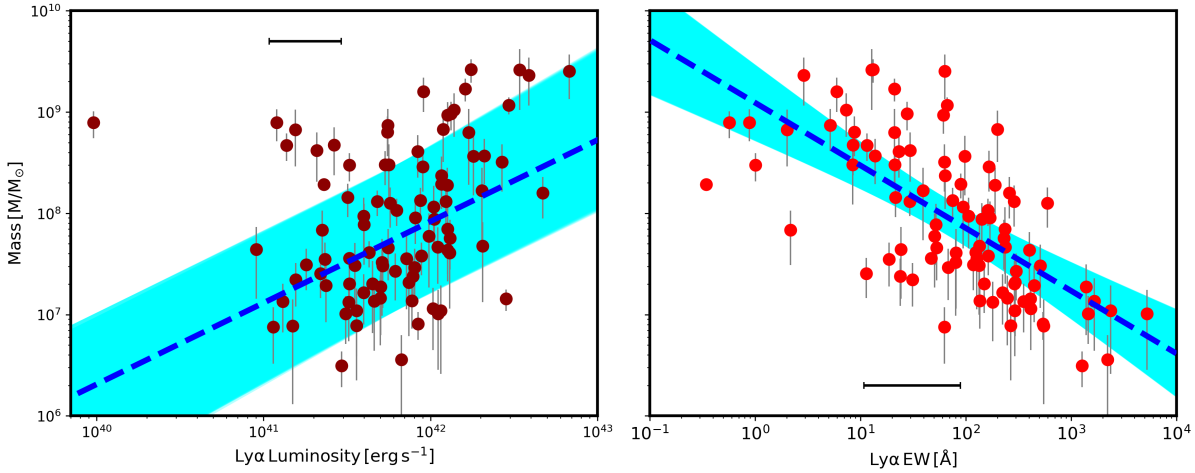

FIGURE 3.10 – Stellar mass vs Lyman-α parameters. *Left :* Stellar mass plotted against Lyman-α luminosity. *Right :* Stellar mass plotted against $\mathrm{EW}_{\mathrm{Ly}\alpha}$. Blue dashed lines indicate linear fits to the data and cyan shaded areas the 1σ uncertainties on the fits, details of which are given in the text. Median uncertainties on the Lyman-α parameters are shown by the horizontal black error bars.

Moving on to the star-forming main sequence, I plot the best-fit stellar masses and SFRs derived from `CIGALE` in Fig. 3.11. This was done for the first time for lensed LAEs of these masses at these redshifts. Therefore, in order to gain an understanding of how these galaxies compare to galaxies of higher mass and UV-selected samples, I incorporated the appropriate best fits from the reviews of S14 and P23, as well as data from S17, a similar study to this one (without the benefit of JWST data) using Lyman break-selected galaxies (LBGs) in the Hubble Frontier Fields (HFF). Additionally, I compared the 96 LAEs to the sample of LBGs selected behind A2744 from Section 3.2 (specifically, the LBG-only galaxies, which show no Lyman-α emission). For the LBGs, an identical fitting process was used to the LAEs, as detailed in Sect 3.2.1. I chose to adopt the time-dependent form of S14 to fit to the data. As the galaxies in this study do not probe the higher mass end of the MS, where its linearity breaks down (see P23 and references therein), this linear form for the MS is safe to adopt. This form of the MS is given as :

$$\log \mathrm{SFR} = (a - b \times t) \log \mathrm{M}_\star - (c - d \times t). \tag{3.1}$$

The values of the constants a, b, c, and d are given in Table 3.2, both for this work and for those I compare to. I adjusted the relations quoted in S14 and P23 to take into account the different IMFs used. I used the Salpeter IMF (Salpeter 1955) for the SED fitting, but the Kroupa IMF (Kroupa 2001) was used in both of the reviews which form the basis of the comparison. This necessitated a correction to the stellar masses, which I carried out following the prescription in both S14 and P23 (taken from Zahid et al. 2012) : $\mathrm{M}_{\star,\mathrm{K}} = 0.62\mathrm{M}_{\star,\mathrm{S}}$ where $\mathrm{M}_{\star,\mathrm{K}}$ and $\mathrm{M}_{\star,\mathrm{S}}$ are the stellar masses calculated using a Kroupa IMF and a Salpeter IMF, respectively. These corrections are incorporated in the dashed lines in Fig. 3.11, but the original quoted fit values are given in Table 3.2.

It is evident from the upper panel of Fig. 3.11 that the low-mass LAEs studied here lie above the fits to the MS calibrated at higher masses. A question thus arises as to why these low-mass LAEs lie above these MS relations, and whether this a result of the selection of these galaxies as LAEs or whether this is rather a result of their low mass. I sought to answer this through comparison to the aforementioned datasets. The most stark difference is seen when making a comparison to the fit of P23. The authors of this review fit to their data a relation of the form :

$$\log \mathrm{SFR} = a_0 + a_1 t - \log(1 + (\mathrm{M}_\star / 10^{a_2 + a_3 t})^{-a_4}), \tag{3.2}$$

with $a_0 = 2.693 \pm 0.012$, $a_1 = -0.186 \pm 0.009$, $a_2 = 10.85 \pm 0.05$, $a_3 = -0.0729 \pm 0.0024$, and $a_4 = 0.99 \pm 0.01$. This fit is designed to take into account the turnover of the MS at high masses ($\mathrm{M}_\star > 10^{10}$) ; however, it performs poorly when compared to the galaxies from this work, especially in the low-mass regime. There is a 0.43 dex difference at $10^7\,\mathrm{M}_\odot$ and a 0.19 dex difference at $10^{10}\,\mathrm{M}_\odot$. This difficulty in fitting the low-mass LAEs is unsurprising as the P23 relation was derived using galaxies down to a lower mass limit of $10^{8.5}\,\mathrm{M}_\odot$.
The fit from S14, which takes the form displayed in Eq. 3.1, fits the data better (noting the error of ~ 0.3 dex in their MS relation). There is a 0.13 dex difference at $10^7\,\mathrm{M}_\odot$ and a 0.17 dex difference at $10^{10}\,\mathrm{M}_\odot$, with S14's relation having been derived using galaxies of mass down to $10^{7.3}\,\mathrm{M}_\odot$. However only two studies with galaxies of mass below $10^8\,\mathrm{M}_\odot$ were included, and S14 did not incorporate the first two Gyr of galaxy evolution in their fit, limiting its usefulness as a comparative tool to this study. Nevertheless, this best-fit relation is consistent with ours within the respective errors.
The fit of the expression in Eq. 3.1 that I found for the LAEs is $\log \mathrm{SFR} = (0.88 \pm 0.07 - 0.030 \pm 0.027 \times t) \log \mathrm{M}_\star - (6.31 \pm 0.41 - 0.08 \pm 0.37 \times t)$. The $\pm 1\sigma$ error region is shaded in pink on both plots in Fig. 3.11. I stress that given the conclusions above, this relation and uncertainty likely do not hold for the lower (and higher) mass regions of this graph, which the data do not probe.
The best fit constants that are not time-dependent (a and c in Eq. 3.1) are consistent within their uncertainties with the best fit of S14, and there is a similar but less significant evolution with time (constants b and d in Eq. 3.1). This points to galaxies selected as LAEs across the redshift range $2.9 < z < 6.7$ as being consistently young and with a high rate of star formation. However, a less significant evolution may also be due in part to the sample in this work being smaller than that of S14. Details of the fitting for the LAEs and LBGs in this work, as well as comparisons to S14 and Santini et al. (2017) (henceforth, S17), are given in Table 3.2.
The discrepancy between my results and the collations of S14 and P23, as mentioned, likely comes from the difference in mass-range probed, but to further verify this, I made a comparison with two UV selected samples in the lower plot of Fig. 3.11 : that of S17, conducted on the HFF galaxy clusters and the selection of LBGs from Section 3.2, (294 galaxies), selected behind A2744 itself, in the same volume as the LAEs in this work. The fit to the LBGs (blue dashed line) is $(0.89 \pm 0.11 - 0.024 \pm 0.007 \times t) \log \mathrm{M}_\star - (6.75 \pm 0.78 - 0.09 \pm 0.59 \times t)$. This relation is consistent with that for the LAEs, further suggesting that it is the mass (and redshift) range probed, rather than the selection of the sample by Lyman-α emission that differentiates these galaxies from MS relations in the literature. A

small effect can be seen in the lower panel of Fig. 3.11 ; the LAE and LBG best fits show a better agreement in the higher mass range than the lower mass range, but this effect is at a low level of confidence ($< 1\sigma$) for this dataset.
The mass-binned data of S17 are in good agreement with the results from this work, particularly in the highest redshift bin ($5 < z < 6.6$). They also found a similar trend when considering earlier times (higher redshifts), namely : an increasing normalisation, but a similar slope compared to later times (lower redshifts). However this evolution is more dramatic in their data. This could be due to their larger sample size ; however uncertainties related to the lack of wavelength coverage past 400 nm above $z = 3$ may have an effect. This photometry can be especially problematic in crowded fields such as lensing clusters (Laporte et al. 2015; Goovaerts et al. 2023). The 2σ-clipping procedure used in S17 and the choice to calculate the MS according to $\log \mathrm{SFR} = \alpha \log (\mathrm{M}/\mathrm{M}_{9.7}) + \beta$ (where $M_{9.7} = 10^{9.7}\,\mathrm{M}_\odot$) may also play a role.
The role of stellar mass is additionally supported by very recent results from Nakane et al. (2023), who found that high-redshift ($z > 7$) LAEs (and LBGs) in a higher mass range than those covered in this study (most galaxies exhibit $\mathrm{M}_\star/\mathrm{M}_\odot > 10^8$) typically lie on the MS (the reference MS in this case is from S17) ; however, their results (similarly to this work) see a lot of scatter in individual data points. Additionally supporting the conclusions of this work, the authors made no significant distinction between the LAE and non-LAE populations in terms of their position on the MS. Even more recently, Liu et al. (2023a) found 10 low-mass LAEs at $z \sim 3.1$ lying above the MS.
Viewed together, these results indicate that, while the low-mass LAEs in this study reside above the typical MS estimates derived from higher mass samples, particularly that of P23 (derived for galaxies of much higher mass), they are likely similar to galaxies that are not LAEs, but are of similar mass at similar redshifts. This points to an enhanced specific SFR in these low-mass populations, but no special role for LAEs themselves. In the context of cosmic reionisation, this supports the conclusion that while low-mass galaxies play an important role, LAEs are likely not singular in their impact on this process.

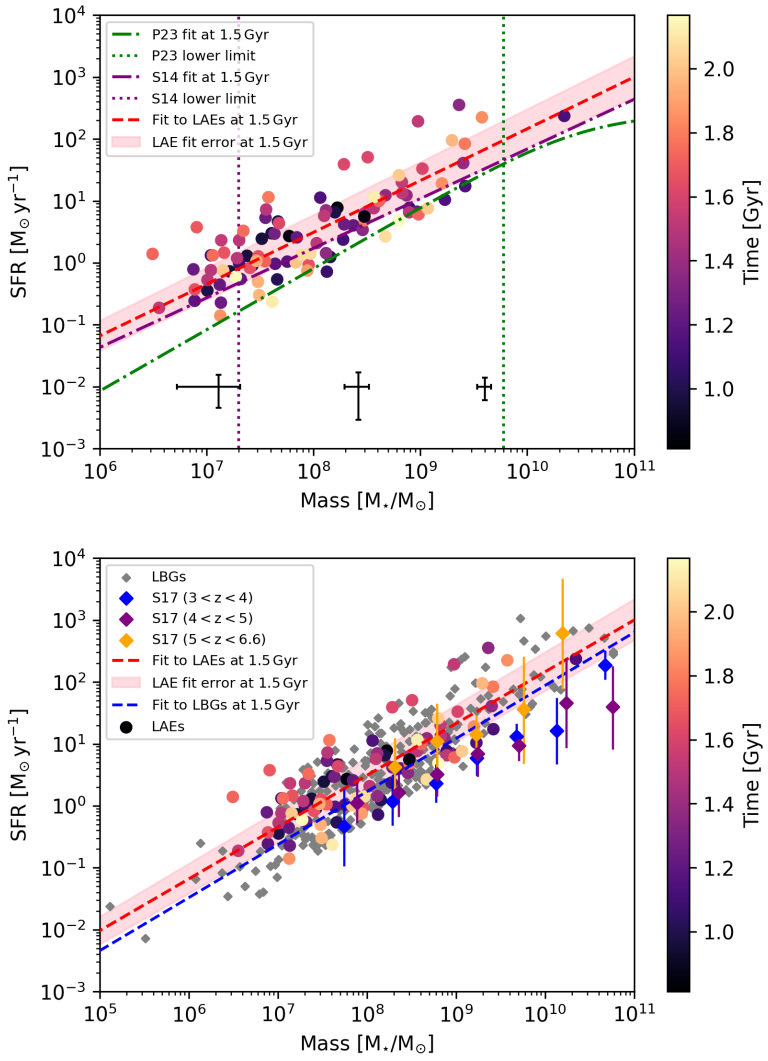

FIGURE 3.11 – Stellar mass vs SFR : the galaxy MS. *Upper panel :* 96 LAEs in the final sample plotted on the MS, together with the best fits to the data of Popesso et al. (2023), Speagle et al. (2014) and the best fit to the LAEs following Eq. 3.1. LAEs are colour-coded by 'Time', in Gyr, which is the age of the Universe at the observed redshift. The purple, dotted line indicates the lowest-stellar mass limit of Speagle et al. (2014)'s review ($2 \times 10^7\,M_\odot$) and the green, dotted line indicates the lowest-stellar mass limit of Popesso et al. (2023)'s review ($6 \times 10^9\,M_\odot$). The pink shaded area denotes the $\pm 1\sigma$ area for the best-fit MS relation at the sample mean age, ~ 1.48 Gyr. The mean error bars in three mass bins ($10^6 < M/M_\odot < 2.5 \times 10^7$, $2.5 \times 10^7 < M_\star/M_\odot < 5 \times 10^8$ and $5 \times 10^8 < M_\star/M_\odot < 10^{10}$) are shown in black at the bottom of the plot.
Lower : Same LAEs and best-fit relation, but compared this time to the results in the same mass range that have been UV-selected, namely : the LBGs from A2744 from Section 3.2 as grey diamonds, with a blue best-fit relation, and the mass-binned results from Santini et al. (2017) as coloured diamonds with error bars.

TABLE 3.2 – Results for the galaxy MS from the literature and from this study.

Study	Redshift	a	b	c	d
S14	$0 < z < 6$	0.84 ± 0.02	-0.026 ± 0.003	6.51 ± 0.24	-0.11 ± 0.03
S17	$3 < z < 4$	1.02 ± 0.04	–	8.52 ± 0.42	–
S17	$4 < z < 5$	0.94 ± 0.06	–	7.75 ± 0.63	–
S17	$5 < z < 6.6$	0.92 ± 0.15	–	6.93 ± 1.59	–
LAEs	$2.9 < z < 6.7$	0.88 ± 0.06	-0.030 ± 0.027	6.31 ± 0.41	-0.08 ± 0.37
LBGs	$2.9 < z < 6.7$	0.89 ± 0.11	-0.024 ± 0.007	6.75 ± 0.78	-0.09 ± 0.59

Notes. Constants a, b, c, and d refer to the constants from Eq. 3.1. In S17, a time dependence (constants b and d) was not quoted so these have been omitted. "LAEs" and "LBGs" denote the results found in this work for the respective populations.

3.4 Discussion : implications for LAEs and reionisation

Now that we have seen what galaxy properties we can derive using HST and JWST photometry, it is worth looking at what these imply about high-redshift LAEs and more globally about reionisation.

To summarise the results so far : in this large sample of intrinsically faint galaxies, I found similar trends to existing literature ; LBGs also selected as LAEs have on average higher SFR_{UV} and steeper UV slopes. High-$EW_{Ly\alpha}$ objects are on average fainter in absolute UV magnitude with steeper UV slopes, and those fainter in UV absolute magnitude tend to have $f_{esc,Ly\alpha}$ approaching $f_{esc,UV}$ or in some cases above, while this is not seen for UV-brighter LAEs. All these trends are seen with significant scatter, which is to be expected given the intrinsically faint nature of the sample, the limits of the photometry (although it is the deepest available[6]), and those objects that have a complex star formation history and physical structure, for which the assumption of constant star formation is less valid. Combined, these results reinforce the picture of high-redshift LAEs as UV-faint, intensely star forming, dust-poor galaxies and indicate that these trends likely hold for galaxies down to $M_{UV} \sim -12$.

The results concentrating on the stellar mass and galaxy MS derived from JWST/NIRCam photometry suggest while LAEs lie above derivations of the MS, the scatter inherent in the sample means that it is statistically similar to the higher mass samples and the sample of LBGs in A2744 from Goovaerts et al. (2023). This suggests that while low-mass galaxies likely play a dominant role in reionisation, LAEs do not distinguish themselves above the general (UV-selected) galaxy population in this regard.

Assessing the relationships between stellar mass and Lyman-α parameters, I found similar results to other previous studies which used LAEs of higher mass, indicating that the

6. A note on the statement "the deepest photometry" : here this means the deepest HST photometry in lensing clusters, across many filters. A JWST program (GLIMPSE, PI : H. Atek) is being observed during the writing of this thesis and will provide the deepest photometry ever performed on any field (120h of total exposure time).

relationship between the stellar mass of a galaxy and how much Lyman-α radiation it emits (and which escapes) remains roughly constant over most of the galaxy stellar mass-range. There is quite some dispersion in these relations, indicating that there are many different escape scenarios for Lyman-α photons from galaxies of all masses (this is investigated further in the following chapters). This is to be expected as there are many galaxy properties which affect Lyman-α escape, however we clearly see the effect in the $EW_{Ly\alpha}$–stellar mass relation, that Lyman-α photons find it harder to escape from higher mass galaxies.

There is significant debate in the literature about the relative contribution of LAEs to reionisation, and these results, as well as those presented in Chapter 5, address this question. This is made possible through comparisons of the LAE and UV LFs, which are integrated to get the SFRD of the respective populations. While authors acknowledge the dependence of the results on the assumed escape fraction of Lyman-α photons (exactly the assumption Chapter 5 attempts to put constraints on), indications of a greater or lesser LAE contribution to reionisation are reported.

An early attempt at assessing the contribution of faint LAEs to reionisation in Dressler et al. (2015) reports a contribution of $20-50\%$. More recently de La Vieuville et al. (2019) find that faint LAEs alone would be enough to reionise the Universe at $z \sim 6$ given an escape fraction of less than 50%. Thai et al. (2023) report similarly high values at $z \sim 6$ when looking at faint, lensed LAEs, higher than blank field studies such as Drake et al. (2017) and Cassata et al. (2011), which report significant, but not dominant contributions from LAEs.

Comparing the properties of LAEs compared to the UV-selected population, as presented in this chapter, will not give a specific fraction of contribution to reionisation, as comparing LFs will, however, the results suggest a similar contribution based on statistically similar properties for faint LAEs and LBGs.

There are several other ways of determining the impact of LAEs on reionisation, among which the method presented in the next chapter, based on what fraction of UV-selected galaxies display Lyman-α emission, which traces the neutrality of the IGM.

A treatment of the escape fraction of Lyman-α photons and how this can help us to assess the LAE contribution to reionisation follows in Chapter 5.

4 Tracing reionisation with the Lyman-α-emitting fraction, X_{LAE}

"Before I came here, I was confused about this subject. Having listened to your lecture, I am still confused – but on a higher level."

- Enrico Fermi

Author's note on content : *This chapter is based on the second goal of my first paper (Goovaerts et al. 2023), detailing the LAE fraction into the end of the epoch of reionisation. This fraction is highly relevant to the global progress of reionisation. Looking at this fraction and its dependencies in more detail, we can make more detailed conclusions about reionisation, its progression and sources.*

Author's note on context : *As noted at the beginning of the previous chapter, this work was listed as the main goal of the thesis at its inception. As there is a great deal of complexity within the LAE fraction, and as it is a facet of the thesis work pertinent to reionisation in a different way to the simple characterisation of the reionising sources, I have chosen to separate this from the results focusing on galaxy properties.*
This is a subject which occupied the first 18 months of my thesis, taking me from knowing very little about this mysterious quantity, X_{LAE}, to understanding far better exactly how complex it is. This complexity is to be expected as X_{LAE} is a "global" quantity which takes into account a great many constituent parts. I do my best to elucidate these parts in the chapter that follows.

4.1 Introduction : X_{LAE}

The goal of the LAE fraction, X_{LAE}, is to be able to track the progress of reionisation, in particular the neutrality of the IGM, by assuming that the intrinsic fraction of UV-selected galaxies that display Lyman-α emission (usually above a certain $\mathrm{EW_{Ly\alpha}}$ limit, mostly taken to be 25 Å) stays constant, so any change must be due to the intervening IGM changing state. A more neutral IGM obscures Lyman-α emission by absorbing and scattering Lyman-α photons. The informed reader will directly see the problem here : is the intrinsic fraction of UV-selected galaxies that display Lyman-α emission constant across different redshifts ? Across different values of $\mathrm{M_{UV}}$, stellar mass, dust content or age ? What about galaxies that display Lyman-α emission but with low (or high) $\mathrm{EW_{Ly\alpha}}$

values ?
This is a complex issue, made even more so as we don't understand exactly what makes a galaxy an LAE, certainly, our understanding is limited to certain situations and sweeping statements (if an example is required, one need look no further than the previous chapter where we manage to disentangle certain properties of LAEs and LBGs, but the scatter in the data is evident, and precludes us from definitively saying : "these are the properties of an LAE" and "these are the properties of a non-LAE").
This is to speak nothing of the different way in which galaxies are selected. There is no homogenisation at all in the way studies of $X_{\rm LAE}$ are conducted, neither the UV-selections nor the LAE selections. A common approach is to follow up UV-selected galaxies in a certain field and redshift range, with a spectrograph that can detect the Lyman-α emission from these galaxies. This is fraught with problems. Firstly, since one starts with a UV selection and can only follow up these objects, one completely misses any galaxies that are detected only by their Lyman-α emission [1]. Secondly, one generally only selects the brightest UV galaxies, ending up with a bias on the resulting sample (this is, of course, highly dependent on the instrument used and the depth of the observations, and whether one is observing in a lensing cluster). Thirdly, one runs into problems during the follow-up, as the Lyman-α emission is not always centred on the UV emission (Shibuya et al. 2014; Hoag et al. 2019; Lemaux et al. 2021; Claeyssens et al. 2022). This causes problems when the follow-up is performed with a slit spectrograph, and multi-object spectrographs such as JWST/NIRSpec's MSA mode are also not immune (Jiang et al. 2023; Napolitano et al. 2024). Observing in this way, one can miss either part of extended Lyman-α emission, or indeed all of it. Observing with an IFU, such as MUSE, immediately solves all these issues, as one can blindly select LAEs without first selecting a population from imaging. Of course, caution must still be exercised about biases in the population, such as targeting the brightest sources, but the situation is much improved.
Overall, these issues highlight the continuing importance of greater understanding in this field, even more than a decade after such a test of reionisation was proposed (Stark et al. 2010, with a large amount of preliminary work having been done even earlier). With the data available for this thesis, I constructed the least biased and largest (in terms of galaxies in the sample) test of $X_{\rm LAE}$ in intrinsically faint galaxies to date.
Typically, literature studies find a rise in $X_{\rm LAE}$ up to $z = 6$, followed by a decline at higher redshifts. This is attributed to the increasingly neutral IGM at higher redshifts (see, for example Stark et al. 2010, 2011; Pentericci et al. 2011; Caruana et al. 2014; De Barros et al. 2017; Mason et al. 2018b; Caruana et al. 2018; Pentericci et al. 2018; Mason et al. 2019; Fuller et al. 2020). Some variation and scatter is seen in results, such as Kusakabe et al. (2020) and Napolitano et al. (2024) whose results suggest a later end to reionisation, between $z = 5$ and $z = 6$, but on the whole, taking into account the different selection criteria and observation methods for the different samples in the literature, as well as the different completeness treatments adopted, good agreement is found across the board.
The variation of $X_{\rm LAE}$ with UV magnitude has also been investigated, i.e. whether brighter or fainter galaxies display greater values of $X_{\rm LAE}$. The general result found in the literature

1. for an extended discussion on these galaxies, I refer the reader to Section 6.2.1, as well as Bacon et al. (2015); Maseda et al. (2020a, 2023); Goovaerts et al. (2023).

is that faint galaxies display larger $X_{\rm LAE}$ values, however this is often dependent on the $\rm EW_{Ly\alpha}$ cut imposed (see Caruana et al. 2018; Kusakabe et al. 2020; Napolitano et al. 2024 and later in this chapter).
All in all, $X_{\rm LAE}$ can tell us about the progress of reionisation, both global, and more local, by studying the differential visibility of Lyman-α emission in different galaxy populations (bright, faint, high mass, low mass, high $\rm EW_{Ly\alpha}$, low $\rm EW_{Ly\alpha}$ etc). In this chapter, I seek to evaluate the redshift evolution $X_{\rm LAE}$ with the largest double-blindly selected sample of lensed, intrinsically faint LAEs and LBGs to date. I also remove the $\rm EW_{Ly\alpha}$ cut to assess the situation for LAEs with low $\rm EW_{Ly\alpha}$. Section 4.2 presents the results of this enquiry and Section 4.3 discusses the results and the implications for reionisation.

4.2 Evolution of $X_{\rm LAE}$ with redshift, $\rm M_{UV}$ and $\rm EW_{Ly\alpha}$

4.2.1 LAE Completeness

The completeness of the populations considered in such a study is very important. This correction to the number of sources detected aims to reflect the number of sources that are missed in the detection process and thus the number of sources actually present in the field of view. Naturally, this is an essential correction for any study wishing to treat total numbers of a population of galaxies and therefore I reinforce an appreciation of this effect when considering $X_{\rm LAE}$.
The completeness methods used for the LAEs in this work are described in Thai et al. (2023) and summarised here. Following the procedure first laid out in dLV19, sources were treated individually in this computation. The advantage of this approach is that each source's unique spatial and spectral shape is taken into account . Each source's Lyman-α brightness distribution profile, observed by MUSE, both in the spatial and spectral dimensions, was modelled and randomly injected 500 times into the NB layer of the original MUSE datacube where its Lyman-α emission reaches a maximum. This process was performed in the image plane, in order to recreate as closely as possible the actual process of detection with MUSELET. The completeness of the source is the number of times (out of 500) it is successfully detected and extracted, using the original source detection method described in Sect. 2.1.1.1.
Since it is the local noise that likely decides whether or not such an injected source is detected, to account for variations, Thai et al. (2023) changed the size of the NB image used to re-detect the simulated sources from 30 arcsec $\times$ 30 arcsec to 80 arcsec $\times$80 arcsec. This was found to improve the extraction of sources with close neighbours. The mean completeness value found for the sample used to calculate $X_{\rm LAE}$ in this work is 0.72 and the standard deviation is 0.34.
Finally, each source's contribution to the LAE fraction was corrected by a value $1/\rm C_i$, where $\rm C_i$ is the completeness value of that source. In effect, a source with a completeness value of 0.5 contributes two LAEs to the calculation of the LAE fraction.
When using the LAE LF from Thai et al. (2023) in Chapter 5, the same completeness procedure has been applied to all LAEs in each of the 17 clusters.

4.2.2 Results : X_{LAE}

Using the galaxies detected in the four HFF clusters : A2744, A370, AS1063 and M0416, I defined four samples : objects identified as LBG-only, objects identified as LAE-only, objects identified as both LAE and LBG (LAE + LBG), and objects identified as LAE that have a continuum detected in the photometry from HST that does not meet the criteria for the LBG sample (LAE+continuum). These samples have 872, 55, 100, and 108 members, respectively.

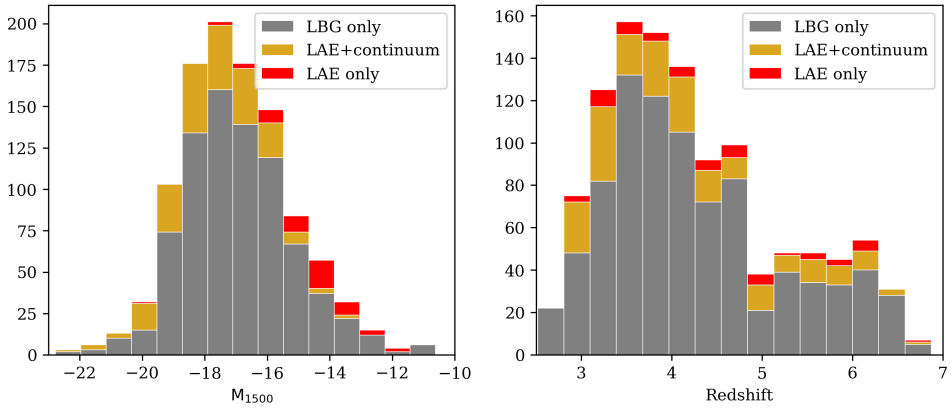

FIGURE 4.1 – $\mathrm{M_{UV}}$ distribution of the populations *(left)* and redshift distribution of the populations *(right)*. The sample labelled 'LAE+continuum' includes all LAEs matched with continuum objects and LBG-selected galaxies.

The sample is dominated by A2744, with 46% of the LAEs and 35% of the LBGs ; this is a large field of view with long MUSE exposures (see Richard et al. 2021; Claeyssens et al. 2022; Thai et al. 2023). However, as many fields of view as possible are valuable additions to the sample. The redshift distribution and the M_{UV} distribution of the sample are displayed in Fig. 4.1. I found the same result as de La Vieuville et al. (2020) when considering the relative importance of LAEs that are totally undetected in the continuum. Their increasing presence is clear when looking at the faint region of the $\mathrm{M_{UV}}$ distribution, even when using the deepest HST photometry. This is crucial to note for any study wishing to catalogue the contribution to reionisation of all star-forming objects at high redshifts. This effect is naturally expected to strengthen with decreasing depth of photometry.
Before discussing X_{LAE} and its relevance to reionisation, I first outline what is typically meant by X_{LAE}. The typical qualitative interpretation is 'the fraction of UV-selected LBGs that display Lyman–α emission'. This stems from the technique of spectroscopic follow-up on a photometric preselection of targets (e.g. Stark et al. 2010, 2011). In the case of this study, both LAE and LBG selections are performed blindly. With an IFU, we also detect LAEs that have no continuum counterpart, objects that would clearly be missed in the aforementioned type of study.
Additionally, limits are typically placed on the inclusion of objects when calculating X_{LAE}. The most common limits are $\mathrm{EW_{Ly\alpha}} > 25\,\text{Å}$ and $\mathrm{M_{UV}} > -20.25$ (Stark et al. 2011; Schenker et al. 2014; De Barros et al. 2017; Mason et al. 2018b; Pentericci et al. 2018;

Arrabal Haro et al. 2018 ; dLV20 among others) ; however, Caruana et al. (2014) use a limit of 75 Å. Other authors, such as Stark et al. (2010), Cassata et al. (2015), Caruana et al. (2018), Kusakabe et al. (2020), and Fuller et al. (2020), investigate different EW and M_{UV} or apparent magnitude ranges to assess the EW and UV magnitude evolution of X_{LAE}, with the exact ranges depending on the study, the depths available and whether or not lensing is involved. In blank fields, most commonly authors investigate the bright and the faint halves of their sample, split at $M_{UV} = -20.25$ (e.g. Cassata et al. 2015; De Barros et al. 2017; Arrabal Haro et al. 2018). Alternatively, where sample sizes allow, studies bin results in M_{UV} from -22 to -18 (e.g. Caruana et al. 2018; Kusakabe et al. 2020). These are important distinctions to be aware of when comparing results from the literature. This discrepancy between the exact inclusion limits studies use, as well as the observational differences (as covered in the introduction) is likely a significant factor in the ongoing debate over the exact evolution of X_{LAE} with redshift, $EW_{Ly\alpha}$ and M_{UV} (see Fig. 4.2).

In this work I provide a perspective based on blind selections of both populations with an IFU and deep photometry with which I can assess more fully the landscape of these high-redshift galaxies. I compare the inclusion of objects only selected as LBG as well as the LAE+continuum sample described in Sect. 3.2. Given that LAEs with no continuum counterpart are detected LAEs I also discuss the effect this has on X_{LAE}. I investigated different M_{UV} and $EW_{Ly\alpha}$ inclusion limits to provide context on the differing results in the literature. This last point is additionally motivated by the use of lensing fields in this study, meaning that it effectively probed a different population than blank field studies. It was therefore appropriate to investigate different regions of the $EW_{Ly\alpha}$ and M_{UV} space. In Fig. 4.2 I compare the results to results from the literature in the classical manner with inclusion limits of $M_{UV} > -20.25$ and $EW_{Ly\alpha} > 25$ Å. The redshift bins used are $2.5 < z < 3.5$, $3.5 < z < 4.5$, $4.5 < z < 5.5$ and $5.5 < z < 7.0$. For each bin, I include four values of X_{LAE} : the fraction of LAEs among LBGs (yellow dots), the fraction of LAEs among LBGs with the completeness corrections described in Sect. 4.2.1 (red dots) and the same two measurements including the LAE+continuum objects (yellow and red stars) (see Sect. 3.2).

Despite significant uncertainties, we see roughly the same trend as many results in the literature, with X_{LAE} decreasing around $z = 6$. The decrease of X_{LAE} shown in the data is quicker than many equivalent measurements in the literature. If one carries forward the assumption that X_{LAE} efficiently probes the neutral hydrogen content, this result suggests that the IGM quickly becomes neutral after $z = 6$.

The objects only detected as LAEs (making up $\sim 21\%$ of the LAE sample) would push these fractions higher, were they to be included. Considering that these objects are extremely faint in terms of UV magnitude and high in terms of $EW_{Ly\alpha}$, they would make an appreciable difference in the calculation of the fraction (in a similar way to the LAE+continuum sample shown by red and yellow stars in Fig. 4.2). There is little reason to suspect that with deeper photometry in the region that sees the rest frame UV emission, the continuum would remain undetected for these objects.

The high values of X_{LAE} that we see in the first (low-redshift) bin in Fig. 4.2 are likely due to the fact that the Lyman break is harder to detect at these redshifts given the

filters available. In order to check this, I performed a simulation, creating 100000 fake LBG sources using Starburst99 templates (Leitherer et al. 1999). I added realistic noise to the data and spread them equally throughout the redshift and UV magnitude space probed by the study. I then attempted to select LBGs following the original selection criteria laid out in Sect. 3.2. In the first redshift bin ($2.5 < z < 3.5$) the amount of LBGs selected versus the number of simulated LBGs is drastically lower than the other bins, at $< 10\%$. It is worth noting that this simulation was computed for AS1063 : a 'best-case scenario', given that AS1063 has the most filters available in the short wavelength range ($< 606\,\mathrm{nm}$). For sources at redshifts between 2.5 and 3, the break would appear between $\sim 320\,\mathrm{nm}$ and $\sim 365\,\mathrm{nm}$. The blue filters have a shallower depth (for AS1063, F225W, F275W, F336W, and F390W have 5σ limiting magnitudes $\sim 24.0, 25.9, 26.3$, and 25.4, respectively) than the redder HST filters and due to this and their scarcity (A2744 only has F275W and F336W), it is challenging to recover all the LBGs in this bin (for complete filter depth information, see Table 2.1). This can also explain why in Fig. 3.2 we can see a trough in the distribution at the lower end of the redshift range, why X_{LAE} is higher than many literature estimates in the lowest-redshift bin and forms part of the reason why we see little evolution between redshifts of 3 and 5. However, the results from this work are still in agreement with the literature results at 1σ. Effects like this are not unexpected considering the varying nature of LBG (and LAE) selection.

The errors on X_{LAE} as displayed in Figs. 4.2 and 4.3 contain several components. As mentioned, there is a big impact on sample inclusion from the $\mathrm{EW}_{\mathrm{Ly}\alpha}$ limits of 25 Å. Therefore, it is important to quantify an error based on this. I performed 1000 Monte Carlo trials of X_{LAE}, sorting the $\mathrm{EW}_{\mathrm{Ly}\alpha}$ values in their error bars, assumed to be Gaussian. I evolved an error estimate for X_{LAE} based on the 16th and 84th percentile of the resulting range of results for X_{LAE}.

Secondly, for the fractions to which I applied the LAE completeness correction, this correction comes with an uncertainty (see Sect. 4.2.1) that is propagated together with the error described above and the Poissonian error count on the number of LBGs and LAEs detected. This Poissonian error in X_{LAE} is given by : $\sigma_P = (N_{LAE}/N_{LBG}^2 + N_{LAE}^2/N_{LBG}^3)^{1/2}$.

The effect of the sample inclusion limits on $\mathrm{EW}_{\mathrm{Ly}\alpha}$ is clear in Fig. 4.2, particularly in the third redshift bin. I reinforce an appreciation of this as a key detail in the calculation of X_{LAE} and the interpretation of plots such as Fig. 4.2. For this study, this source of error means that it is not possible to describe a statistically significant evolution of X_{LAE} until the highest-redshift bin.

Similarly, the inclusion of the LAE+continuum objects in the calculation of X_{LAE} (denoted by red and yellow stars in Fig. 4.2) has an appreciable effect : an average absolute difference in X_{LAE} of 0.05 for points without completeness correction and 0.07 for those with completeness correction. This is a reflection of the impact of LBG selection in the final calculation of X_{LAE}, particularly the S/N criterion imposed in the selection.

Finally, we can see from Fig. 4.2 that the completeness correction applied to the number of LAEs plays an important role in the calculation of X_{LAE} (see the red points in Fig. 4.2). Without this correction, it is also difficult to address the redshift evolution of X_{LAE}.

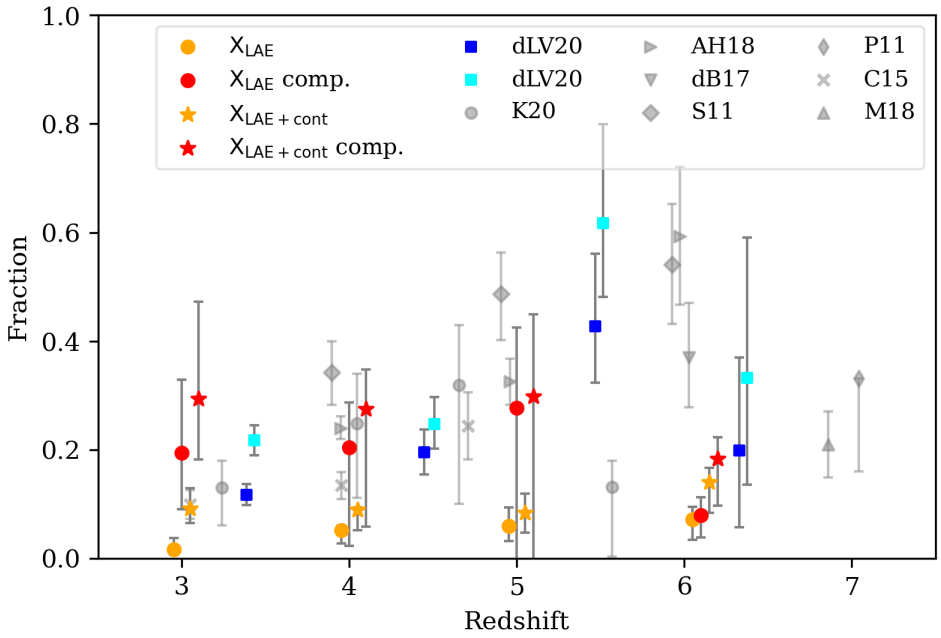

FIGURE 4.2 – LAE fraction, $X_{\rm LAE}$, over a redshift range of 2.9 to 6.7, using the typical literature limits of $\mathrm{EW}_{\mathrm{Ly}\alpha} > 25\,$Å and $\mathrm{M}_{\rm UV} > -20.25$. The coloured circles represent $X_{\rm LAE}$ when just LAE+LBG objects are taken into consideration, and the coloured stars represent the same calculation but including the LAE+continuum sample (see Sect. 3.2). Coloured stars indicate these $X_{\rm LAE}$ values including the completeness correction for the number of LAEs (see Sect. 4.2.1). Blue and cyan squares represent the results from dLV20, with cyan representing those with the completeness correction. Shorthand is used in the legend for the literature results, but I give the full list here (in the same order as the legend) : Kusakabe et al. (2020), Arrabal Haro et al. (2018), De Barros et al. (2017), Stark et al. (2011), Pentericci et al. (2011), Cassata et al. (2015), and Mason et al. (2018b). A small redshift offset is artificially applied to some points for clarity.

There is interesting and unsettled debate on the relative evolution of $X_{\rm LAE}$ between the UV-bright and UV-faint populations (see Stark et al. 2010; Oesch et al. 2015; De Barros et al. 2017; Stark et al. 2017; Kusakabe et al. 2020). In particular, this debate has consequences at higher redshifts, $z \gtrsim 6$, on what type of objects can be seen in Lyman-α emission despite an increasingly neutral IGM. Relations between the UV magnitude and Lyman-α emission at these redshifts may hold clues as to how the IGM is reionised and which objects are primarily responsible for this. In order to assess this, I split the sample in UV absolute magnitude at $\mathrm{M}_{\rm UV} = -18$ (as this limit splits the sample roughly in half) and recalculated $X_{\rm LAE}$ for the bright and faint portions. Figure 4.3 shows this comparison. It is worth noting that the $\mathrm{M}_{\rm UV}$ ranges into which the data is split differ from many similar comparisons in the literature due to the lensed nature of the sample used in this work. The data efficiently probe down to $\mathrm{M}_{\rm UV} \sim -12$, much fainter than studies conducted in blank fields. By contrast, there are few objects as bright as $\mathrm{M}_{\rm UV} = -22$.

In the upper panel of Fig. 4.3, there is no statistical difference between the bright and faint halves of the sample until the final redshift bin ($5.5 < z < 7.0$); however, there is a rising trend in the bright half and a decreasing trend in the faint half. In order to investigate this further I removed the $EW_{Ly\alpha}$ limit of 25 Å, resulting in the lower panel of Fig. 4.3. Based both on the result from Fig. 3.6 and indications from the literature (Curtis-Lake et al. 2012; Stark et al. 2017), it is likely that UV-bright galaxies exhibit Lyman-α with small EWs : close to or below the 25 Å limit, due to spectral and spatial dispersion of the Lyman-α photons from such systems (Mason et al. 2018b).
This is supported by the clear distinction we see in the lower panel of Fig. 4.3. This result suggests that, while UV-fainter objects generally have higher Lyman-α EWs, the LAE fraction is greater among UV-brighter objects, albeit with those objects exhibiting smaller $EW_{Ly\alpha}$.

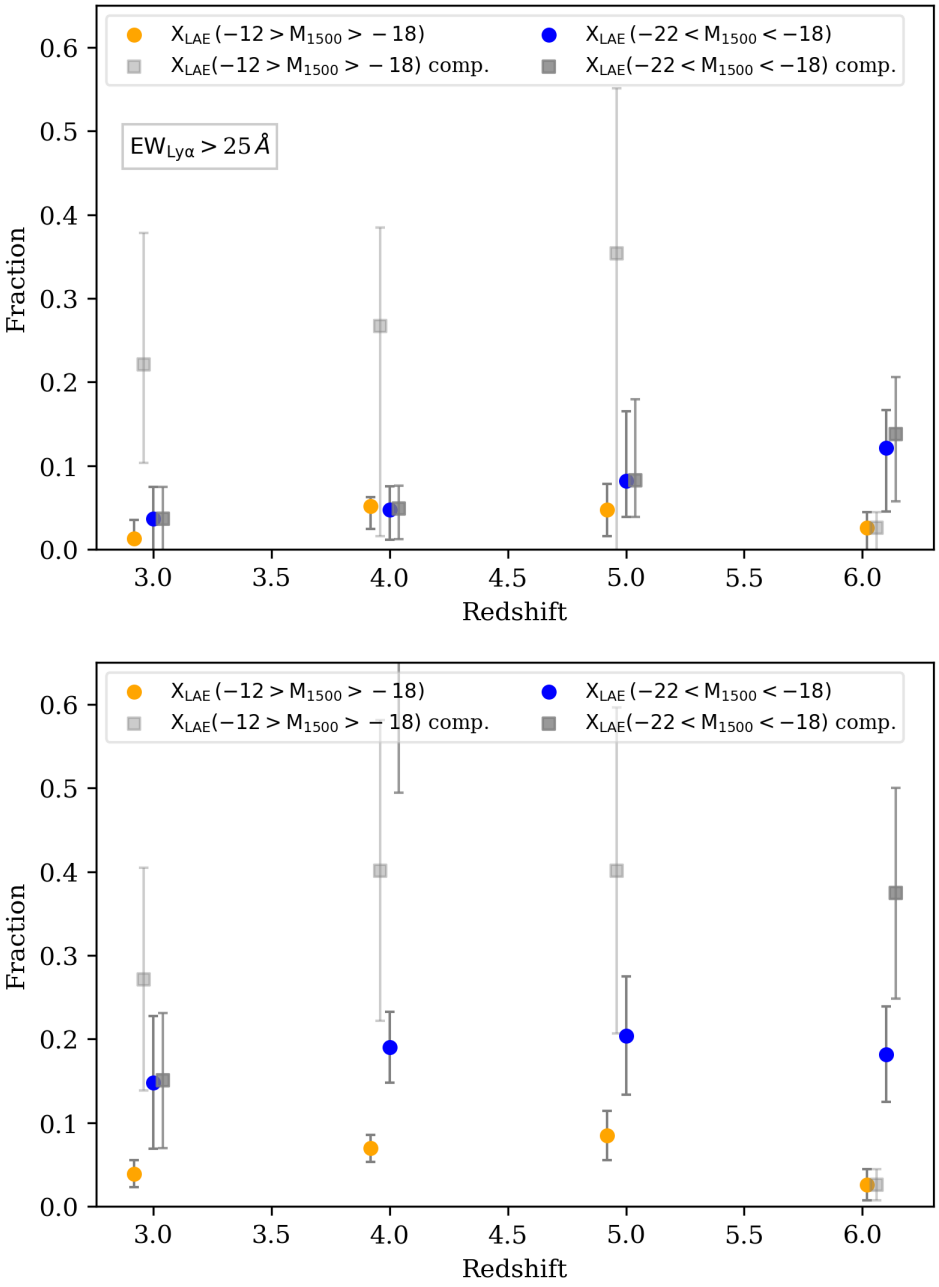

FIGURE 4.3 – Redshift evolution of $X_{\rm LAE}$ in the bright and faint populations, split at $M_{UV} = -18$. The bright and faint populations are shown in blue and orange, and the completeness corrections in grey scale with the bright population in darker grey. The top panel corresponds to LAEs with $EW_{Ly\alpha} > 25$ Å, while the lower panel shows the results when this limit is removed. The absence of the EW limit leads to a clearer separation between the two populations, suggesting that UV-bright LBGs exhibit a larger fraction of objects with Lyman-α emission when objects with small values of $EW_{Ly\alpha}$ are taken into account. In the lower panel the UV-bright completeness-corrected point at $z \sim 5$, omitted from the plot, is at 1.19 (see the main text).

4.3 Discussion : Implications for reionisation

The findings for the differences in X_{LAE} when removing this $\mathrm{EW}_{\mathrm{Ly}\alpha}$ limit and looking at the bright and faint halves of the sample are especially interesting in the context of the number of low $\mathrm{EW}_{\mathrm{Ly}\alpha}$, UV-bright objects reported towards and into the epoch of reionisation (Curtis-Lake et al. 2012; Oesch et al. 2015; Stark et al. 2017; Mason et al. 2018a,b, as well as most recently with JWST : Larson et al. 2022; Bunker et al. 2023; Witstok et al. 2023; Witten et al. 2023; Whitler et al. 2023b). This result is often taken as surprising given that the increasingly neutral IGM should block much of the Lyman-α emission at redshifts greater than 6. However, it is possible that with an increasingly neutral IGM, the more luminous galaxies ionise a surrounding bubble, making it easier for Lyman-α emission to escape. These galaxies are also more likely to be situated in reionised overdensities (Matthee et al. 2015; Mason et al. 2018a; Witten et al. 2023). Witten et al. (2023), cataloguing eight LAEs within the epoch of reionisation, most of which have small $\mathrm{EW}_{\mathrm{Ly}\alpha}$ ($< 25\,$Å), also suggested that mergers and tidal interactions with neighbours may be responsible for enhanced Lyman-α visibility during the epoch of reionisation. Reionised bubbles created by these processes and these bright galaxies would allow the Lyman-α photons to redshift out of resonance by the time they encounter significant neutral hydrogen, and hence would not be absorbed or scattered (see Dijkstra 2016 for a quantitative treatment of this effect).

More detailed, individual analysis of individual objects would be necessary to firmly support these conclusions for the high-redshift objects but the difference seen in the highest-redshift bins of the graphs in Fig. 4.3 broadly supports the enhanced visibility of UV-bright, low-$\mathrm{EW}_{\mathrm{Ly}\alpha}$ LAEs during the epoch of reionisation.

I caution the reader that a population of high-EW LAEs undetected in the continuum is detected by MUSE, and if these objects were to be detected with deeper photometry, they could modify this result as they would be UV-faint with high $\mathrm{EW}_{\mathrm{Ly}\alpha}$. However, they are roughly equally spread over the redshift range probed so may leave the trends in Fig. 4.3 unchanged.

I plot the completeness corrected results in Fig. 4.3 in grey scale, darker grey representing the UV-bright portion of the sample and lighter grey representing the UV-faint portion. Due to the smaller sample sizes in these magnitude-split bins, these corrections have large errors where one or a few LAEs with a small completeness values, accounting for many completeness-corrected LAEs, can dominate the determination of X_{LAE} for a given bin. The lower panel of Fig. 4.3 provides an example : X_{LAE} for the bright half of the sample in the bin $4.5 < z < 5.5$ is at 1.19 ; accounting for the completeness correction, there are more UV-bright LAEs than LBGs in this bin. Noting that this is caused by individual highly incomplete objects, I do not interpret this as meaningful in the context of X_{LAE} with respect to the evolution of the IGM and reionisation. On the other hand, I note that the completeness-corrected trends also broadly support the conclusions outlined earlier in this section, particularly in the highest-redshift bins, where the difference between the UV-bright and UV-faint portions of the sample is even more pronounced.

It is important to note that all the literature concerning X_{LAE} selects samples of LAEs and LBGs differently, with different instruments, selection functions and completeness treatments. With this in mind, we can regard the result and physical interpretation of

Fig. 4.2 as relatively robust. It is encouraging that despite the different methods of observation and selection, the trend in $X_{\rm LAE}$ points broadly to a decrease around $z \sim 6$. With that said, the discrepancies in $X_{\rm LAE}$ between different studies, particularly in different luminosity regimes, as well as different ranges in terms of $\rm EW_{Ly\alpha}$ highlight how much intrinsic scatter there is in the LAE population and how much caution must be exercised when making global conclusions. It is therefore crucial to push the limits of the parameter space we search, for example in terms of UV magnitude, reinforcing the importance of using observations in lensing clusters such as those in this thesis. Additionally, this thesis presents the largest and least biased sample through the use of lensing, several different fields, and an IFU. This means the observations do not suffer from potential flux losses from slits, or flux missed altogether (e.g. Jiang et al. 2023). Additionally, with MUSE, we can observe LAEs not detected in the continuum which is impossible with a UV preselection and spectroscopic follow-up. This allows the full range of LAEs with continuum counterparts to be assessed, no matter how faint or undetected the counterpart is. The use of lensing reduces the bias in terms of preferentially brighter objects being observed at higher redshifts (although does not altogether remove it) and the use of multiple fields reduces the impact of cosmic variance.

Returning to the split in the sample into UV-faint and UV-bright halves, this comparison revealed what I interpreted as a statistical signature at lower redshift of works emerging at a similar time looking at ionised bubbles around LAEs within the EoR ($z > 6$) (Witten et al. 2023; Witstok et al. 2023; Whitler et al. 2023b). These LAEs tend to have small values of $\rm EW_{Ly\alpha}$ ($\lesssim 25$ Å), to be expected as they are UV-bright (see Fig. 3.6), and would be missed in any analysis considering only the typical literature limit of $\rm EW_{Ly\alpha} > 25$ Å. How do we interpret this in the face of the evidence pointing to UV-faint galaxies being the main drivers of reionisation ? It seems that while this is still likely the case, UV-bright galaxies become visible more easily in the EoR, especially when looking at Lyman-α emission, because of the ionised bubbles that they manage to clear around themselves, which is more difficult for fainter galaxies emitting fewer ionising photons. While these UV-bright galaxies would likely never have been able to achieve reionisation on a global scale by themselves, these results suggest they were the first to create wholly reionised regions, from which Lyman-α emission could escape.

The detailed progression of reionisation is a question addressed from many angles, including hydrodynamical and radiative simulations (Ocvirk et al. 2020; Garel et al. 2021; Kannan et al. 2022; Giovinazzo et al. 2024), galaxy studies (Stark et al. 2010; Pentericci et al. 2011; Bouwens et al. 2015b,a) and the Lyman-α forest (Nasir &D'Aloisio 2020; Qin et al. 2021; Bosman et al. 2022, see also the very recent works of Spina et al. 2024 and Zhu et al. 2024). In recent years the consensus has been shifting towards a "patchy" reionisation that progresses fastest in certain areas and leaves neutral "islands" until after $z = 6$ (Kulkarni et al. 2019; Bosman et al. 2022; Zhu et al. 2022).

It is very possible that these visible, $z > 5$, UV-bright LAEs are an additional sign of this inhomogeneous reionisation, where early LAEs become visible due to reionised areas of the Universe allowing Lyman-α photons to redshift out of resonance and continue, unabsorbed.

It is likely then, that we will keep finding these high-redshift LAEs as it is clearly possible

for massive, UV-bright galaxies to form even at very early times (Donnan et al. 2023; Arrabal Haro et al. 2023b; Chemerynska et al. 2023; Ferrara et al. 2023), as well as protoclusters and overdensities (Laporte et al. 2022; Morishita et al. 2023; Saxena et al. 2023), from which Lyman-α emission could escape. In theory, the fraction of these galaxies which intrinsically exhibit Lyman-α emission could also rise due to intense star formation at early times (i.e. many of young, hot O and B stars ionising neutral hydrogen). Hence LAEs are an extremely valuable, and visible [2] probe of galaxy evolution even at the earliest times.

In order to understand their role in reionisation further, it is crucial to better understand the escape of Lyman-α photons from the galaxies themselves. This is the subject of the next chapter.

2. I warn here that not all LAEs will be visible, only UV-bright LAEs or those situated in reionised overdensities. Therefore there will be an intrinsic bias when studying this population that we must be aware of.

5 Charting the escape of Lyman-α photons in the range $2.9 < z < 6.7$

"If we knew what it was we were doing, it would not be called research, would it ?"

— *A. Einstein*

Author's note on content : *This chapter is based on the third project of my thesis, focusing on the Lyman-α escape fraction, $f_{esc,Ly\alpha}$ (Goovaerts, Thai et al., submitted). The paper on which this is based was written by myself, with significant input from my colleague Thai Tran, which I gratefully acknowledge. $f_{esc,Ly\alpha}$ is difficult to measure, as one needs some measure of the intrinsic star formation rate of a galaxy to compare to the star formation rate derived from Lyman-α. I attack this problem using two methods, an object-per-object investigation using MUSE-detected Lyman-α emitters with HST and JWST photometry, and a comparison of two state of the art luminosity functions, that of lensed Lyman-α emitters and that of lensed UV-selected galaxies. I then comment on the validity of these methods and what the results tell us about Lyman-α emitters and their contribution to reionisation.*

Author's note on context : *This third project of the thesis was a very natural progression of the work, given the importance of the Lyman-α escape fraction and the newly available JWST data and luminosity functions. This one took time to get right, many aspects of the galaxy selection and comparison of luminosity functions were highly non-trivial, not to mention the intrinsic complication of the Lyman-α escape fraction. I went through multiple realisations about the selections and the physics during this process, so I think my supervisor and co-authors for bearing with me. I enjoyed the journey of writing this paper hugely, I think it brought me very close to the actual physics, which is something that doesn't always happen when you're wading through mountains of data.*

5.1 Introduction : Lyman-α escape

In Section 1.4 I presented the complications associated with the escape of Lyman-α photons from a galaxy. Many physical properties of a galaxy affect this escape : dust content (Atek et al. 2008; Verhamme et al. 2008; Finkelstein et al. 2009; Hayes et al. 2011, 2013; Runnholm et al. 2020), movement in the ISM and CGM, i.e. inflows and outflows (Hansen &Oh 2006; Gronke &Dijkstra 2016; Stark et al. 2017; Mason et al. 2018a; Ferrara

2023), viewing angle and geometry (Blaizot et al. 2023; Giovinazzo et al. 2024) and the (neutral or ionised) IGM surrounding the galaxy (Stark et al. 2010, 2011; Pentericci et al. 2011, 2018).

Understanding the escape of Lyman-α photons is critical to understanding their impact on the IGM during reionisation, as well as characterising the galaxies and the specifics of Lyman-α emission themselves. A further interest is to be found in the connection between Lyman-α emission and escape and Lyman Continuum (LyC) emission and escape (Verhamme et al. 2015, 2017; Liu et al. 2023b; Hu et al. 2023; Kerutt et al. 2024; Pahl et al. 2024; Yuan et al. 2024; Choustikov et al. 2024a). LyC photons are the photons bluewards of 912 Å responsible for reionising neutral hydrogen, and as such, the escape of these photons from galaxies is an operative quantity in their impact on the surrounding IGM. LyC photons are impossible to observe directly above $z \sim 6$ due to the intervening neutral IGM which absorbs them. Indirect tracers, such as Lyman-α observables (FWHM, line separation) and escape are therefore invaluable probes, if a strong connection can be found, of LyC escape. Going forward, Lyman-α escape will be denoted as $f_{esc,Ly\alpha}$ and LyC escape as $f_{esc,LyC}$.

Much effort has been dedicated towards better understanding of Lyman-α escape, which requires an estimate of the intrinsic star formation of a galaxy, in order to compare the expected production of Lyman-α photons with the observed Lyman-α luminosity. There are inevitably assumptions associated with these estimates of a galaxy's intrinsic SFR, as well as significant intrinsic scatter expected within the LAE population, due to the wide range of galaxy physical properties. Both of these issues add to the complication of determining $f_{esc,Ly\alpha}$. An alternative approach seen in the literature is the comparison of the LAE luminosity function (LF) with the UV LF, assumed to be the LF of the entire galaxy population. This method offers a different outlook, effectively measuring the escape of Lyman-α photons in a given survey volume. Measuring $f_{esc,Ly\alpha}$ with both methods is valuable, as well as the comparison between the two.

Strides have been made in recent years toward quantifying $f_{esc,Ly\alpha}$ and its evolution with redshift. Blanc et al. (2011), henceforth B11, studied the evolution of dust properties and $f_{esc,Ly\alpha}$ across a sample of ~ 100 blank-field LAEs in the range $1.9 < z < 3.8$, as well as comparing star formation rate densities, SFRDs, derived from LAE and UV luminosity functions (henceforth LFs) in order to quantify the evolution of $f_{esc,Ly\alpha}$ with redshift. They found a sample median of $\sim 29\%$ when considering their LAEs individually, and negligible redshift evolution.

Hayes et al. (2010) found a significantly lower $f_{esc,Ly\alpha}$, around 5% at $z = 2.2$, using a blind narrowband survey searching for Hα and Lyman-α. The authors made use of the Hα line to estimate un-obscured star formation and compare to the star formation derived from Lyman-α. The Hα line originates from the same process as the Lyman-α line and is less sensitive to dust attenuation, therefore often a more reliable indicator of star formation. One general agreement in the literature is that $f_{esc,Ly\alpha}$ increases with redshift. Low values such as $0 - 5\%$ are found in the aforementioned study as well as Hayes et al. (2013), Verhamme et al. (2017), Sobral et al. (2017), Sobral &Matthee (2019) and Runnholm et al. (2020). Larger values such as $30 - 40\%$ and even higher are found at redshifts towards the epoch of reionisation (B11 ; Hayes et al. 2011; Chen et al. 2023; Witstok et al. 2024; Lin

et al. 2024; Napolitano et al. 2024).
Another general agreement found in the literature relates to sample selection. Samples which are selected by their Lyman-α emission typically display higher values of $f_{esc,Ly\alpha}$ when compared to samples selected by Hα (Song et al. 2014; Trainor et al. 2016; Sobral &Matthee 2019; Matthee et al. 2021).
By contrast, significant scatter in $f_{esc,Ly\alpha}$ is expected in all samples, likely due to the large number of factors which affect Lyman-α photon escape and the differing conditions present in any sample of galaxies. This can be seen in all studies on $f_{esc,Ly\alpha}$, from low redshift (Hayes et al. 2010, 2013; Ciardullo et al. 2014; Matthee et al. 2016b; Runnholm et al. 2020), to the higher redshift such as B11, Chen et al. (2023), Lin et al. (2024) and Napolitano et al. (2024).
Currently the most powerful estimators for determining $f_{esc,Ly\alpha}$ in an indirect manner include $EW_{Ly\alpha}$ (Sobral &Matthee 2019) and Lyman-α line separation (Yang et al. 2017; Matthee et al. 2021). The correlation with Lyman-α line separation is likely due to the presence of outflows, to which the Lyman-α line shape is sensitive (Gronke &Dijkstra 2016; Blaizot et al. 2023). These outflows produce channels of low HI column density in the ISM and CGM which allows for more Lyman-α photons to escape (Hashimoto et al. 2015).
Constraining $f_{esc,Ly\alpha}$ in a global way, using the UV and LAE LFs, gives the escape fraction of Lyman-α photons over a specific survey volume, from the ratio of the SFRDs derived by integrating the respective LFs. Employing this method, Konno et al. (2016), B11 and Hayes et al. (2010) found a gentle evolution over their redshift ranges which can be fitted with a power law of the form : $f_{esc,Ly\alpha} = C \times (1+z)^{\xi}$. Hayes et al. (2011) found that $f_{esc,Ly\alpha}$ reaches unity (i.e. 100%) around $z \sim 11$ and Cassata et al. (2011) found this to be around $z = 6 - 8$. However, previously, such research has been conducted without significant statistics in the Lyman-α luminosity range $\log L_{Ly\alpha}\,[\mathrm{erg/s}] < 41$, hence without the ability to fully constrain the faint part of the LF. In this work, the observations in lensing clusters make it possible to reach $\log L_{Ly\alpha}\,[\mathrm{erg/s}] \sim 39$. This means that it is not necessary to extrapolate the LF when integrating to these faint limits.
I start with a determination of $f_{esc,Ly\alpha}$ for the sample of ~ 100 LAEs behind the A2744 lensing cluster using the HST and JWST photometry which has already been so useful for the earlier work in this thesis, comparing $f_{esc,Ly\alpha}$ to galaxy properties and assessing its redshift evolution in Section 5.2. The NIRCam data, extending to $\sim 5\,\mu m$, allows us to access, for the first time, the rest-frame optical emission of these LAEs and greatly improves the reliability of the properties extracted with SED fitting. The NIRCam imaging notably also covers the entire MUSE field-of-view, meaning the full sample size of MUSE LAEs can be explored. This would not be the case with calculations of SFR from Hα and dust attenuation from the Balmer decrement obtained from spectroscopy, for example from JWST/NIRSpec's MSA mode. This would, in principle, be preferable, due to fewer assumptions needed and the lack of photometric coverage of the infrared for the LAEs. However, samples of LAEs at the redshifts concerned by this study with Balmer line determinations are rare, and not large. Using photometry, one can gain an appreciable sample size using just one cluster, although more would be preferable, and soon possible with current and upcoming JWST observations.

Studies of emission lines with slit spectroscopy for these galaxies (especially lensed LAEs and therefore potentially extended sources, both by lensing and due to the extended nature of Lyman-α haloes) are not without difficulties themselves. Parts of flux can be missed in slits, especially slits as small as JWST/NIRSpec's MSA (0″.2 to 0″.45). (Napolitano et al. (2024) provide a good discussion of these difficulties), and sometimes, flux can be missed altogether, such as in Jiang et al. (2023).
Subsequently I move on to the second method described above, comparing the two state-of-the-art LFs currently available, the LAE LF from Thai et al. (2023) and the UV LF from Bouwens et al. (2022). Section 5.3 details this, starting with a description of the LFs and followed by the redshift evolution of $f_{esc,Ly\alpha}$ as revealed by said LFs. Finally in Section 5.4 I discuss the implications for LAEs and their impact on reionisation, as well as the assumptions made for the LF comparison and their validity as pertains to this study.

5.2 Escape fraction of individual galaxies

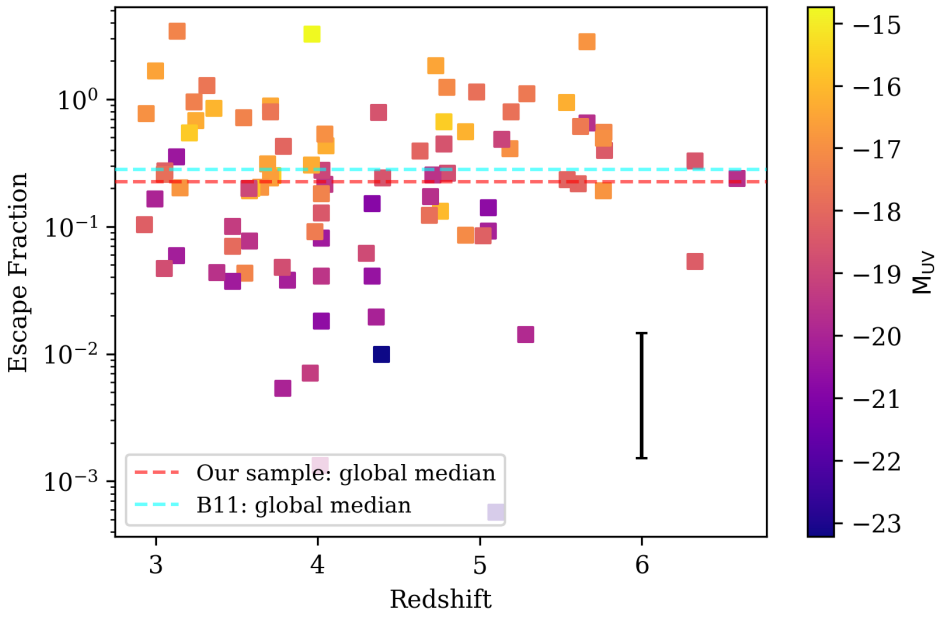

FIGURE 5.1 – Redshift evolution of the escape fraction of Lyman-α photons (where $10^0 = 1 = 100\%$ escape) from LAEs in the A2744 lensing cluster, colour-coded by the absolute UV magnitude of each LAE. The global medians of the sample and that in B11, are shown with red and blue dashed lines respectively. The black error bar is the median uncertainty of the sample ($\sim 18\%$) (note : not the uncertainty on the median). It is shown as if it were at the level of the global median (red line), but offset for clarity.

To calculate the escape fraction on an object-per-object basis for the 96 individual LAEs behind the A2744 lensing cluster, I compared the SFR inferred from the Lyman-α flux to the dust-corrected SFR from the `CIGALE` SED fitting process described in Sect. 3.2.1. The

SFR inferred from the Lyman-α flux was calculated using the prescription in Kennicutt (1998a) and the conversion factor of 8.7 between Hα luminosity and Lyman-α luminosity, using a Case B recombination scenario (Osterbrock 1989).
The ratio of these two SFRs gives the escape fraction of Lyman-α photons, $f_{esc,Ly\alpha}$. The redshift evolution of this quantity is shown in Fig. 5.1. The sample median is shown as the red dashed line and the sample median in B11 is shown as the blue dashed line. They are consistent to within each other's errors, even though B11 use a different prescription for finding $f_{esc,Ly\alpha}$. The median escape fraction error bar of the sample is shown in black. Each LAE is colour-coded by its absolute UV magnitude, calculated from the filter that sees the rest frame 1500 Å emission. One can clearly see that Lyman-α photons escape more easily from UV-fainter objects, a result already remarked upon by Lin et al. (2024), Napolitano et al. (2024). To clarify this further, I fitted a relation between the absolute UV magnitude and $f_{esc,Ly\alpha}$ for each galaxy. This is shown in Fig. 5.2, where the galaxies are now colour-coded by redshift-bin and median error bars for each bin are shown in the corresponding colour. The best-fit to this data is :

$$\log(f_{esc,Ly\alpha}) = (0.27 \pm 0.02)\, M_{UV} + (4.2 \pm 0.5). \tag{5.1}$$

This is clearly a tighter relation than the one shown by redshift vs $f_{esc,Ly\alpha}$, with an uncertainty on the slope and normalisation of about 10 %. These quantities, M_{UV} and $f_{esc,Ly\alpha}$, are not independent as M_{UV} is related to the intrinsic SFR of a galaxy, so this relation is to be expected, but it is nevertheless noticeable that below $M_{UV} = -18$ there are few galaxies with $f_{esc,Ly\alpha}$ values less than 10%. Care must be taken interpreting this result however, as incompleteness can play a role as we start to probe fainter galaxies (towards the right of Fig. 5.2). To better assess this, on Fig. 5.2 I plot three regions where increasing incompleteness is to be expected, as a function of UV magnitude and lensing magnification. This is based on the limiting flux for a MUSE detection (of an LAE). The three magnification regions plotted are $\mu = 1.5$, the minimum magnification included in the sample (the area covered by MUSE observations do not reach the areas with less magnification than this, most of the area has $\mu > 2$), $\mu = 9$, the maximum magnification for an image included in the sample (note that there are LAEs not included and images not included with $\mu > 9$) and $\mu = 137$, the maximum magnification of any LAE image in the A2744 lensing cluster. These three regions delineate the area of this plot where incompleteness, in terms of detecting a faint galaxy with a small $f_{esc,Ly\alpha}$ value with MUSE, may play an increasing role. We can see that this effect likely becomes important towards the faint end of this plot, at $M_{UV} \gtrsim -17$. However at the brighter end of this graph, the incompleteness in unlikely to shape the relation we observe.
There are LAEs undetected in the continuum which might be expected to fill this region of the graph. However they are uniquely objects of high escape fraction (based on upper limits of the UV continuum, and no dust correction). These objects are denoted by the black triangles in Fig. 5.2 : lower limits on $f_{esc,Ly\alpha}$ and upper limits on M_{UV}.
I note also that around this M_{UV} value of -18 that we start to see objects with $f_{esc,Ly\alpha}$ > 100%. $f_{esc,Ly\alpha} > 100\%$ means that we are seeing more Lyman-α emission than we should, given the standard conversions between Lyman-α and UV luminosities and SFR detailed above. Reasons for this may include the assumptions inherent in making those conversions,

such as constant SFH, ages greater than ~ 50 Myr and the case B recombination scenario (Osterbrock 1989), becoming less valid. This may point concurrently to the models failing to correctly estimate the dust content of these galaxies and thereby underestimating the intrinsic SFR. However this would mean that some property of these galaxies is heavily attenuating the UV emission, but not attenuating the Lyman-α emission accordingly. Atek et al. (2008) postulate that geometry or the presence of large outflows may play a role in disconnecting Lyman-α emission and dust, such that one may see a high $f_{esc,Ly\alpha}$ from a heavily dust-attenuated system.

We also see LAEs for which the continuum is completely undetected in the deepest photometry to date (Bacon et al. 2015; Maseda et al. 2020a; de La Vieuville et al. 2020; Goovaerts et al. 2023; Maseda et al. 2023), and $f_{esc,Ly\alpha}$ for these galaxies is, naturally, very high, often greater than 100% (as calculated from 2σ upper limits on the UV continuum). This suggests that there is more than simply model inadequacy at play here. I discuss these objects further in Section 5.4.3.

Unlike M_{UV}, we see no significant evolution of $f_{esc,Ly\alpha}$ with redshift, although there are relatively few objects at redshifts higher than 6. It is clear from Fig. 5.1 that the results are affected by missed objects above $z = 6$, both in the high-$f_{esc,Ly\alpha}$ regime (as these objects have low M_{UV}) and the low-escape fraction regime, as objects with low $f_{esc,Ly\alpha}$ are harder to detect at higher redshifts.

The comparison to the results in B11 suggest that $f_{esc,Ly\alpha}$ does not evolve significantly over the redshift range $1.8 < z < 6$. This is in tension with certain literature results such as Hayes et al. (2011), who find that $f_{esc,Ly\alpha}$ increases with redshift ($0.6 < z < 6$). However, this study was performed in a similar way to the global analysis of $f_{esc,Ly\alpha}$ that I present in the following sections. Hence I return to this point having taken both methods into consideration.

The scatter in the individual results shown in Fig. 5.1 is to be expected, given the wide variety of conditions within galaxies, even LAEs, expected to be mostly young and highly star-forming. Dust content of these galaxies likely varies, which plays a significant role in the escape of Lyman-α photons (Verhamme et al. 2008). Additionally and as mentioned, geometry and line-of-sight effects are also expected to have a hand in the amount of Lyman-α photons which reach the observer (Verhamme et al. 2012; Dijkstra &Kramer 2012; Gronke &Dijkstra 2016; Blaizot et al. 2023; Giovinazzo et al. 2024).

While there is consistency between the sample medians of B11 and this work, the offset, as well as the smaller scatter of the results in this work is to be expected based on the differing methods for finding $f_{esc,Ly\alpha}$. B11 assumed an intrinsic UV slope of -2.23 in order to calculate the dust reddening $E(B-V)$. As this UV slope likely depends on factors other than dust, such as metallicity, age and mass of the stellar population (Buat et al. 2012; Wilkins et al. 2013; Bouwens et al. 2016; Reddy et al. 2018; Topping et al. 2022), and as there is evidence for slopes bluer than this value (De Barros et al. 2017; Naidu et al. 2022; Goovaerts et al. 2023; Iani et al. 2023; Nanayakkara et al. 2023; Napolitano et al. 2024; Austin et al. 2024), I preferred not to use this assumption. If there are bluer intrinsic slopes than this, we would expect the corresponding $E(B-V)$ values from B11 to be higher, therefore the intrinsic SFR to be higher and the calculated escape fractions lower. This is what we see in the results. There is also less scatter in $f_{esc,Ly\alpha}$ as the results

do not depend on estimations of the UV slope which are known to have significant scatter (and uncertainty).
The sample median, 22.5 %, agrees with determinations at slightly lower redshift from Sobral et al. (2017); Matthee et al. (2021), who both quote escape fractions of ~ 30 % for LAEs. Most recently, also using JWST, Chen et al. (2023) find a sample median of 28 % for 10 LAEs at $5 < z < 8$.
However, I note that the scatter on individual determinations of $f_{esc,Ly\alpha}$ remains a very significant consideration when assessing samples of the kind in Fig. 5.1. It is therefore unlikely that we will be able to specify a precise fraction for Lyman-α escape at any given redshift. It is clear that the trend of $f_{esc,Ly\alpha}$ with M_{UV} is more useful.
I note also that while individual $f_{esc,Ly\alpha}$ values are better determined using Hα fluxes and the Balmer decrement, the intrinsic scatter seen remains similar, with values ranging from < 1% escape to 100% (see, for example, Chen et al. 2023; Napolitano et al. 2024). For the sample, we can take additional encouragement from the fact that the dust content of these low-mass LAEs, at these redshifts, is both expected to be, and observed to be, very low. I therefore do not expect many cases where the SED fitting significantly underestimates the dust attenuation of a galaxy.
Both methods of determining $f_{esc,Ly\alpha}$ are valuable then, and a more detailed comparison between them for the same sample of galaxies is desirable.

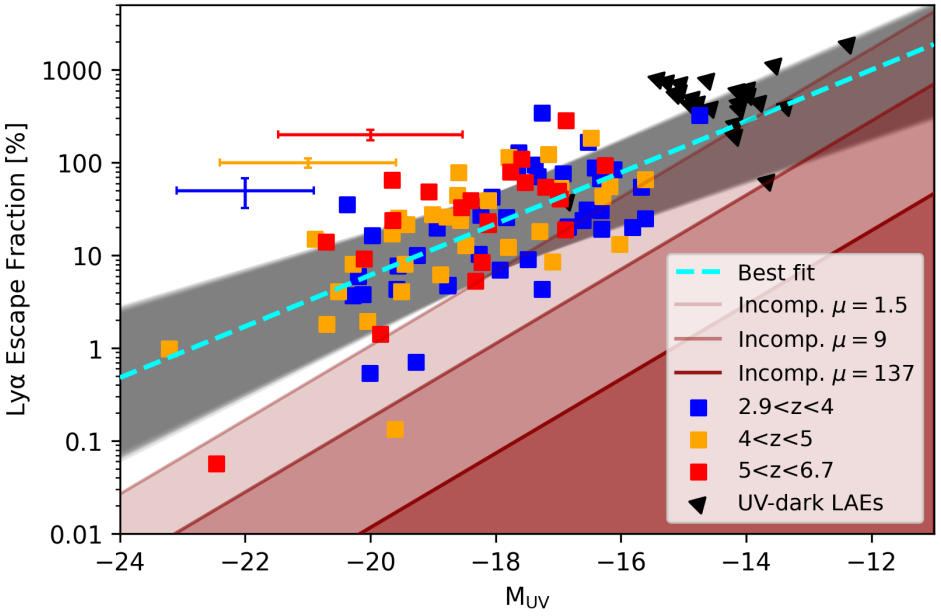

FIGURE 5.2 – The evolution of $f_{esc,Ly\alpha}$ with absolute UV magnitude M_{UV}. Photometrically-detected galaxies are split into three redshift bins to stress the lack of evolution in this sense, while the evolution with M_{UV} is fit by the relation in cyan (details in text). Median error bars for the three redshift bins are shown in the corresponding colour and $f_{esc,Ly\alpha}$ error bars are also listed here for clarity : $2.9 < z < 4 = 0.18$, $4 < z < 5 = 0.12$ and $5 < z < 6.7 = 0.25$. Absolute magnitude values and their errors are adjusted for magnification. Black triangles denote continuum-undetected LAEs. M_{UV} values are upper limits and escape fraction values are lower limits. These objects are not included in the fit. Red shaded areas denote regions of incompleteness based on MUSE line-detections : a darker colour representing increasing lensing magnification (see text).

5.3 Global Escape fraction

One can derive estimates of $f_{esc,Ly\alpha}$ in a global manner by comparing the LF of LAEs and that of the 'total' galaxy population. Integrating both of these LFs gives the Lyman-α luminosity density $\rho_{Ly\alpha}$ and the total luminosity density ρ_{total}. From this one can derive the respective SFRDs. Then taking the ratio of these SFRDs gives $f_{esc,Ly\alpha}$ (Hayes et al. 2010; Blanc et al. 2011; Zheng et al. 2013; Konno et al. 2016). In order to perform this calculation, I started from the two state-of-the-art LFs in lensing fields, the LAE LF from Thai et al. (2023) and the UV LF from Bouwens et al. (2022), assumed here to be the 'total' galaxy population. This assumption and its consequences for the results of this study are discussed in detail in Sect. 5.4.3.
Before presenting the derivation of $f_{esc,Ly\alpha}$, I briefly detail both LFs used, starting with the LAE LF from Thai et al. (2023).

5.3.1 LAE and UV LFs

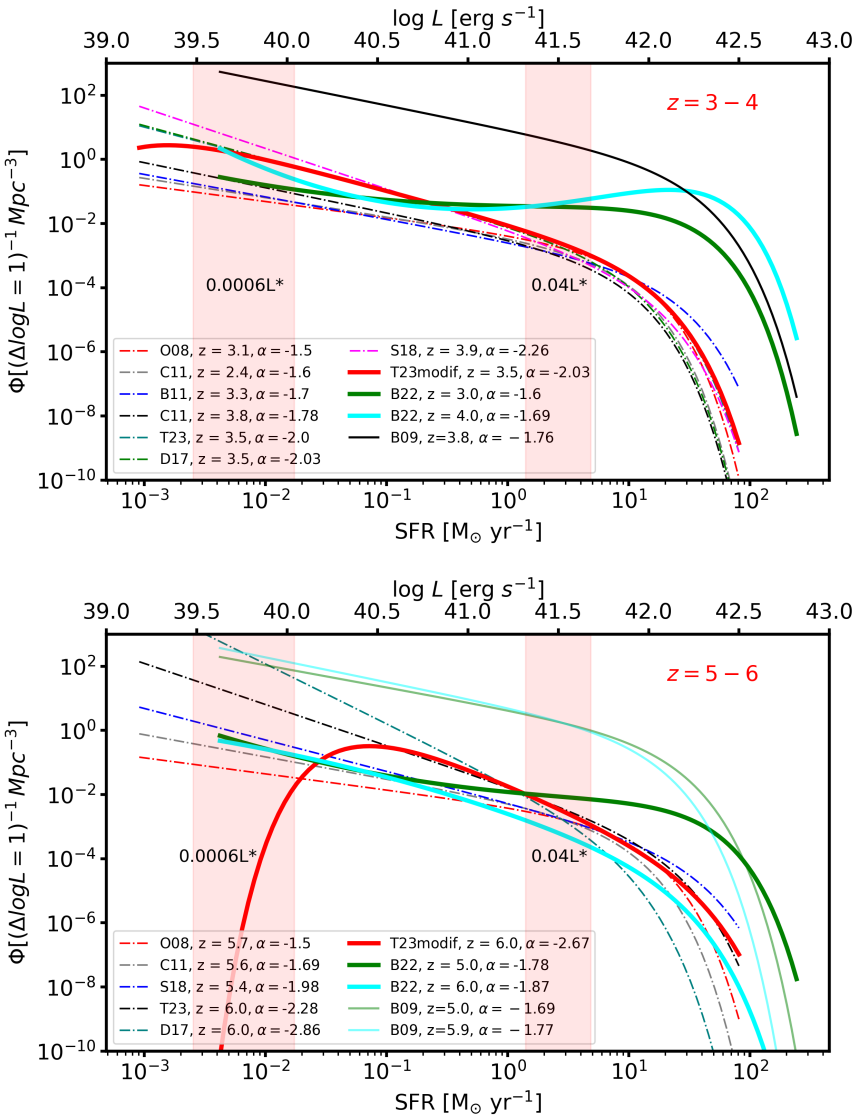

FIGURE 5.3 – UV and LAE LFs included in the analysis, on a common x-axis of SFR. The LFs of Bouwens et al. (2022) and Thai et al. (2023) are shown in bold and the literature LFs are shown in coloured dash-dotted lines. The LF integration limits in terms of $L*$ that are used throughout this work are denoted by the pink shaded regions. *Upper panel :* results from the redshift range 3 to 4. *Lower panel :* results from the redshift range 5 to 6. The literature LFs in the graph are shown in shorthand in the caption and here in full, in order : Ouchi et al. (2008); Cassata et al. (2011); Sobral et al. (2018); Drake et al. (2017); Bouwens et al. (2022); Bouwens et al. (2009).

The LAE LF from Thai et al. (2023) includes 600 LAEs behind 17 lensing clusters observed by MUSE, identified with highly secure redshifts ($zconf = 2, 3$, meaning high

Lyman-α line SNR, clearly asymmetric line profile, etc) as defined in Richard et al. (2021). The LAEs cover four orders of magnitude in luminosity $39 < \log L[\mathrm{erg\ s^{-1}}] < 43$ and is described best by a modified Schechter function, appropriate for an LF with a turnover. The modified Schechter function takes the form :

$$\Phi(L)e^{-(L_T/L)^m} = \frac{\Phi^*}{L^*}\left(\frac{L}{L^*}\right)^{\alpha} e^{-L/L^*} e^{-(L_T/L)^m} \tag{5.2}$$

where Φ^*, L^* and α are the three traditional Schechter function parameters : the normalisation parameter, the characteristic luminosity (the point at which the power law changes to an exponential) and the faint end slope. $\Phi(L)$ is the number density of galaxies in a given logarithmic luminosity interval. L_T and m are the new parameters of the modified function, the luminosity at the turnover point and a power index of about unity.

In the analysis I also included results for the LAE LF at different redshift intervals from literature studies to build a general picture, and provide brief descriptions of these works here. de La Vieuville et al. (2019) studied the LF evolution of ~ 120 LAEs behind four lensing clusters observed by MUSE, with the same redshift range as Thai et al. (2023). Using blank field observations, Ouchi et al. (2008); Blanc et al. (2011); Cassata et al. (2011); Drake et al. (2017); Konno et al. (2016) presented the LF evolution with redshift of LAEs with luminosities greater than $\log L\,[\mathrm{erg/s}] = 41$. Due to lacking data at faint luminosities, Ouchi et al. (2008) fixed the slope value of the Schechter function at $\alpha = -1.5$ ($z = 3.1, 3.7, 5.7$). B11 fixed this parameter at $\alpha = -1.7$ ($z = 1.9 - 3.8$), while Cassata et al. (2011) found $\alpha = -1.6^{+0.12}_{-0.12}$, $-1.78^{+0.10}_{-0.12}$, -1.69 (fixed) at $z = 2-3, 3-4.5, 4.5-6.5$, respectively. However, at a higher redshift and a higher luminosity range, this value has been found to be much steeper, varying from -2.26 to -2.56 at redshift $z = 5.7$, and from -1.86 to -2.5 at redshift $z = 6.6$ (Konno et al. 2016) ; or ~ -1.98 at redshift $z = 5.4 \pm 0.4$ (Sobral et al. 2018), depending on the luminosity limitations used for fitting.

Bouwens et al. (2022) presented a new derivation of the UV LF in the redshift range $2.0 < z < 9.0$ including over 2500 lensed galaxies behind the HFF clusters using HST observations from the HFF (Lotz et al. 2017), GLASS (Treu et al. 2015) and CLASH (Postman et al. 2012) programmes. This LF probes down to $\mathrm{M_{UV}} < -16$ over the full redshift range considered in this study. A smooth flattening of α was found, from $\alpha = -2.28 \pm 0.10$ at redshift $z = 9$ to $\alpha = -1.53 \pm 0.03$ at redshift $z = 2$. Over the redshift range probed, $3 \lesssim z \lesssim 7$, the faint-end slope is found to evolve from $\alpha \sim -1.60$ to $\alpha \sim 2.05$. The shape of the LF and its evolution agrees well with other results in the literature, including determinations from blank fields (see Parsa et al. 2016, as well as other references in Bouwens et al. 2022).

I treated this LF as the LF of the total "parent" population in order to calculate the total SFRD. In this way, inclusive of completeness corrections, I assumed that both LFs represent the "total" of their respective populations within the quoted Lyman-α luminosity and absolute UV magnitude limits. This is an assumption that I return to and discuss in Section 5.4.3. When taking the ratio of $\rho_{\mathrm{Ly}\alpha}$ to ρ_{total}, this LF gives ρ_{total} for all the different values of $\rho_{\mathrm{Ly}\alpha}$ used (see Fig. 5.4). All these LFs are shown on a common scale of SFR in Fig. 5.3 with the LFs of Thai et al. (2023) and Bouwens et al. (2022) highlighted in thicker solid lines.

5.3.2 Global Escape Fraction Results

The results from the Lyman-α LF in each redshift interval were integrated with luminosity to map out the evolution of Lyman-α luminosity density with redshift :

$$\rho_{Ly\alpha} = \int L_{Ly\alpha}\, \phi_{Ly\alpha}\, dL_{Ly\alpha}. \tag{5.3}$$

This was then converted to the Lyman-α SFRD based on the calibration of Kennicutt (1998a), assuming the factor of 8.7 between intrinsic Lyman-α and Hα flux, and a case B recombination (Osterbrock 1989) :

$$\mathrm{SFRD_{Ly\alpha}\,[M_\odot yr^{-1}Mpc^{-3}]} = 7.9 \times 10^{42} \times \rho_{\mathrm{Ly\alpha}}/8.7. \tag{5.4}$$

The UV luminosity density was converted into the equivalent SFRD using the form SFRD $= \kappa \times \rho_{UV}$ (Madau &Dickinson 2014), in which κ is the conversion factor, sensitive to the recent SFH, metal-enrichment history and the IMF. ρ_{UV} is the UV luminosity density which is expressed in units of erg s^{-1}Hz^{-1}, estimated by integration the UV LF with M_{UV}. The widely used value of the conversion factor from Kennicutt (1998b) is $\kappa = 1.4 \times 10^{-28}$, where a Salpeter IMF (Salpeter 1955) is assumed. Bouwens et al. (2022) used a Chabrier IMF Chabrier (2003) for this conversion, so I corrected for this, using a factor of 1.96. Going forward, the SFRD obtained from UV LF is treated as the total SFRD of the entire galaxy population. I estimated the total UV SFRD down to $M_{UV} = -13$ at redshifts $z = 2, 3, 4, 5, 6, 7$ (see Table 5.1 for the values used, after correction to the Salpeter IMF). Subsequently I interpolated the SFRD to redshifts $z = 2.5, 3.1, 3.5, 3.7, 4.5, 4.7, 5.4, 5.7$ to adapt to redshift bins used in the literature studies. The ratio between the LAE SFRD and the total, dust-corrected SFRD in a given redshift interval gives the global Lyman-α escape fraction. This definition was applied in the works of Hayes et al. (2011), Cassata et al. (2011), B11, Zheng et al. (2013) and Konno et al. (2016). The results for the global escape fraction derived in this work are shown in Figs 5.4 and 5.5. The results are compared to the literature derived using several LAE LFs, for which I adopted an identical approach to that described above (Ouchi et al. 2008; Blanc et al. 2011; Cassata et al. 2011; de La Vieuville et al. 2019; Thai et al. 2023; Sobral et al. 2018). The same UV LF was used for each comparison.

TABLE 5.1 – UV SFRD used to calculate $f_{esc,Ly\alpha}$.

Redshift	SFRD unobscured	SFRD obscured	SFRD total
		$\log_{10}[M_\odot\,Mpc^{-3}\,yr^{-1}]$	
$z = 2.0$	-1.28 ± 0.03	-0.8 ± 0.1	0.220 ± 0.043
$z = 3.0$	-1.11 ± 0.07	-1.1 ± 0.1	0.163 ± 0.026
$z = 4.0$	-1.12 ± 0.12	-1.2 ± 0.1	0.14 ± 0.03
$z = 5.0$	-1.33 ± 0.09	-1.5 ± 0.1	0.0772 ± 0.0134
$z = 6.0$	-1.46 ± 0.05	-2.0 ± 0.1	0.045 ± 0.005
$z = 7.0$	-1.56 ± 0.06	-2.6 ± 0.1	0.0299 ± 0.0041

Notes. Values adapted from (Bouwens et al. 2022), adjusted for the conversion from the Chabrier IMF to the Salpeter IMF. Each value was calculated with an integration limit of $M_{UV} = -13$.

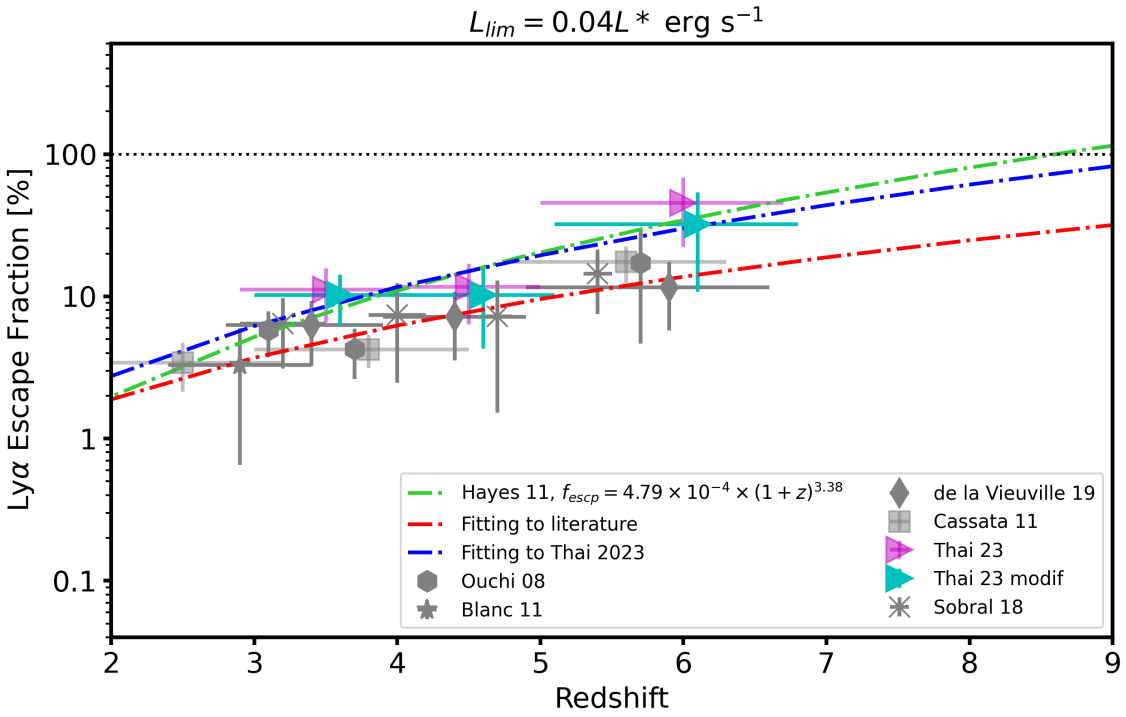

FIGURE 5.4 – Global redshift evolution of $f_{esc,Ly\alpha}$ with an integration limit on both LFs of $0.04L*$. The results, using the LFs from Thai et al. (2023) are shown in cyan for the modified Schechter function and pink for the general Schechter function. The dotted horizontal line denotes $f_{esc} = 100\%$. The dash-dotted green curve is from Hayes et al. (2011) in the redshift range of $2.2-6.6$ and calculated with the integration limit $0.04L*$. The red dash-dotted curve is the best fit to all the data shown and the blue dash-dotted curve fits just the data of Thai et al. (2023) (cyan points : modified Schechter function).

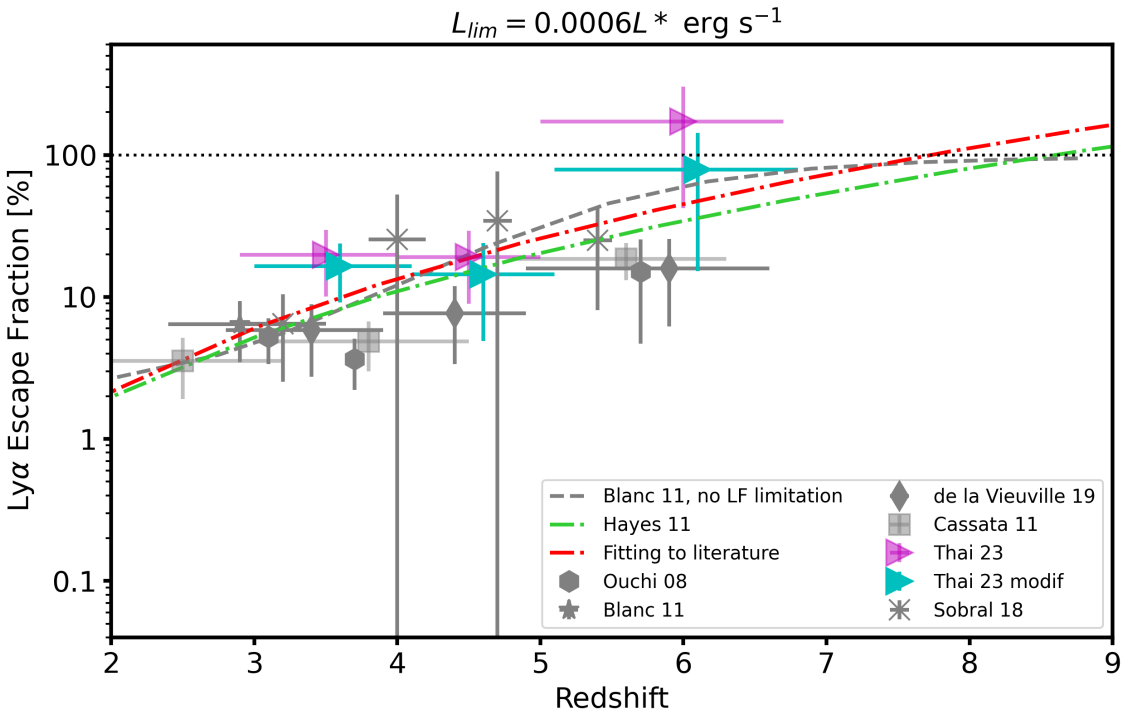

FIGURE 5.5 – Global redshift evolution of $f_{esc,Ly\alpha}$ with an integration limit on both LFs of $0.0006L*$. Results from this study are shown by cyan (modified Schechter function) and pink (general Schechter function) points. Power-law fits from the literature are shown in grey and green (B11, Hayes et al. 2011) and the equivalent fit to all the data is shown in red. The fit from Hayes et al. (2011) is derived from results integrated to $0.04L*$, and the fit from B11 from results integrated to 0.

The lower limits of the respective LF integrations are worth noting. I used two different limits, the first was $0.04L*$ and the second was $0.0006L*$ (where $L*$ is the characteristic galaxy luminosity of the Schechter function). The first limit, as suggested in Hayes et al. (2011) was designed to compare this study to previous results using brighter galaxies. It corresponds to limits of $\log L_{Ly\alpha}[\mathrm{erg\,s^{-1}}] \sim 41$ and $M_{UV} \sim -17$ respectively. The results for $f_{esc,Ly\alpha}$ calculated with this limit are shown in Fig. 5.4. The second limit, $0.0006L*$, corresponds to the faint regimes that are reached with the LAE and UV LFs ($\log L_{Ly\alpha}[\mathrm{erg\,s^{-1}}] \sim 39.5$ and $M_{UV} \sim -13$) and is shown in Fig. 5.5. The vertical error bars are estimated from published uncertainty values in $\phi*$, α, $L*$ (LAE LFs) and $\phi*$, α, $M*$ (UV LF). The horizontal error bars display the redshift intervals of each survey. As de La Vieuville et al. (2019) and Thai et al. (2023) probed the LAE LF at the same redshift intervals, the data points derived from the LF of de La Vieuville et al. (2019) have been shifted by 0.1 in redshift. Table 5.2 presents the results for each study using this integration limit, as well as the SFRD value derived. By comparing the results obtained with the different limits it is possible to assess the impact of the faint galaxies that are observed with the latest LAE and UV LFs.
To investigate the global evolution of escape fraction with redshift, I used the power-law

form that was proposed by B11 and Hayes et al. (2011) : $f_{escp}^{Ly\alpha} = C \times (1+z)^{\xi}$. The coefficient C is constrained strongly by the evolution of escape fraction at low redshift while the exponent ξ is defined by the evolution at high redshift. In Fig. 5.4, the best fits calculated for this work are shown as red and blue dash-dotted lines, fitting all the points in the graph and only those of Thai et al. (2023), respectively. In Fig. 5.5, the red fit is to all the data.
The green dashed line shows the fit from Hayes et al. (2011), which used the UV LF obtained from Ouchi et al. (2004); Reddy et al. (2008); Bouwens et al. (2009) and an LF integration down to $0.04L*$ (fitted to data over the range $2 < z < 6$). I leave this fit in both plots to guide the eye as to the difference when integrating to a fainter limit. B11 use the results of Bouwens et al. (2010) and an integration limit of 0. The fit of B11 is shown in Fig. 5.5 to provide the comparison to earlier results which have been integrated to 0.
I find $C = 14.3 \pm 14.0 \times 10^{-4}$ and $\xi = 2.3 \pm 0.6$ when fitting to all the literature and $C = 12 \pm 43 \times 10^{-4}$ and $\xi = 2.8 \pm 2.1$ when only fitting the results from Thai et al. (2023) with the integration limit at $0.04L*$. With the lower integration limit of $0.0006L*$, I find $C = 4.1 \pm 7.7 \times 10^{-4}$ and $\xi = 3.6 \pm 1.2$ when fitting the results together with all the ancillary data in Fig. 5.5. Because the other studies included in this graph do not probe the faint regime that the LFs I used do (equivalent to the integration limit of $0.0006L*$) and therefore require an extrapolation outside the limits of the datasets used, during this fitting process I set the weight of each point equal to the weight of the equivalent point from our study (i.e. the cyan point in the same redshift bin). This relation is qualitatively consistent with the equivalent relation derived in Hayes et al. (2011) (green dashed line, noting that this relation is derived using a different UV LF and a brighter integration limit) and suggests that $f_{esc,Ly\alpha}$ will reach 100% around $z = 8$.

TABLE 5.2 – LAE luminosity density and its SFRD.

z	Ref.	α	log $L*$	log $0.0006L*$	$\rho_{Ly\alpha}$ (10^{39})	LAE SFRD (10^{-3})	f_{escp} [%]
$z = 3.1$	O08	-1.5	42.8	39.5	9.2 ± 2.9	8.4 ± 2.6	5.2 ± 1.9
$z = 3.7$	O08	-1.5	43.0	39.8	6.0 ± 2.1	5.4 ± 1.9	3.7 ± 1.4
$z = 5.7$	O08	-1.5	42.8	39.6	9.0 ± 6.1	8.2 ± 5.6	15.1 ± 10.4
$z = 1.95 - 3$	C11	-1.6	42.7	39.5	7.5 ± 3.2	6.8 ± 2.9	3.6 ± 1.6
$z = 3 - 4.5$	C11	-1.78	42.8	39.6	7.9 ± 2.6	7.1 ± 2.4	4.9 ± 1.9
$z = 4.5 - 6.6$	C11	-1.69	43.0	39.8	12.4 ± 3.1	11.3 ± 2.8	18.5 ± 5.4
$z = 1.9 - 3.8$	B11	-1.7	43.1	39.9	7.0 ± 5.2	6.3 ± 4.7	6.4 ± 3.0
$z = 3.1 \pm 0.3$	S18	-1.63	42.8	39.6	11.4 ± 6.7	10.4 ± 6.1	6.5 ± 4.0
$z = 3.9 \pm 0.2$	S18	-2.26	42.9	39.7	40.6 ± 42.6	36.8 ± 38.7	25.4 ± 27.2
$z = 4.7 \pm 0.1$	S18	-2.35	43.3	40.1	36.8 ± 44.4	33.4 ± 40.4	34.5 ± 42.1
$z = 5.4 \pm 0.4$	S18	-1.98	43.3	40.1	17.8 ± 11.8	16.1 ± 10.7	25.1 ± 17.1
$z = 3.5$	dLV19	-1.58	42.8	39.6	9.8 ± 4.9	8.9 ± 4.4	5.8 ± 3.1
$z = 4.5$	dLV19	-1.72	43.0	39.7	9.3 ± 4.9	8.4 ± 4.4	7.7 ± 4.3
$z = 6.0$	dLV19	-1.87	43.2	39.9	9.5 ± 5.7	8.6 ± 5.1	15.9 ± 9.7
$z = 3.5$	T23	-2.0	42.9	39.7	33.3 ± 15.2	30.3 ± 13.8	19.8 ± 9.7
$z = 3.5$	T23 (mSF)	-2.03	42.9	39.7	27.7 ± 11.2	25.2 ± 10.2	16.5 ± 7.3
$z = 4.5$	T23	-1.97	43.0	39.8	23.2 ± 11.4	21.0 ± 10.4	19.1 ± 10.2
$z = 4.5$	T23 (mSF)	-2.06	43.0	39.8	17.5 ± 11.0	15.9 ± 10.0	14.4 ± 9.5
$z = 6.0$	T23	-2.28	43.0	39.8	103.2 ± 76.5	93.7 ± 69.5	171.9 ± 129.6
$z = 6.0$	T23 (mSF)	-2.67	43.3	40.0	47.3 ± 37.6	43.0 ± 34.2	78.8 ± 63.6

Table 5.2 Notes. SFRD calculated by integrating each LF to $0.0006L*$. The references are, in order : Ouchi et al. (2008); Cassata et al. (2011); Blanc et al. (2011); Sobral et al. (2018); de La Vieuville et al. (2019); Thai et al. (2023). The acronym "mSF" refers to instances where the modified Schechter function was used. The units of $\rho_{Ly\alpha}$ and the LAE SFRD are erg s^{-1}Mpc^{-3} and M$_\odot$yr^{-1}Mpc^{-3} respectively and the units of $L*$ are erg s^{-1}.

5.4 Discussion

With the individual and global results now in hand, we can interpret them, compare them and consider what they can tell us about $f_{esc,Ly\alpha}$ and its evolution. I will also discuss the validity of the assumption that these LFs show us the same population and finally I will assess the impact these results have on the LAE contribution to cosmic reionisation at $z = 6$.

5.4.1 The global evolution of $f_{esc,Ly\alpha}$

Fig. 5.4 shows the determination of $f_{esc,Ly\alpha}$ using the LF integration limit $0.04L*$. I plot this graph in order to compare to previous literature determinations which used samples of galaxies brighter than this work, and, in comparison, to assess the impact of the bright ($M_{UV} < -17$) and faint populations ($M_{UV} < -13$) on the evolution of $f_{esc,Ly\alpha}$. I plot results derived using both the modified (cyan) and the general Schechter (pink) functions, in order to show the difference in these results created by the presence or lack of a turnover in the LAE LF. However, at this integration limit the behaviour of the modified Schechter function is close to that of the traditional Schechter function, so we do not see a significant difference in $SFRD_{Ly\alpha}$. As the current best derivations of the LF come from the modified Schechter functions, going forth I discuss the results related to these (cyan points).
There is a good agreement at all redshifts between the results derived in this work and the results from the literature. We see little evolution between $z \sim 3.5$ and $z \sim 4.5$, followed by a jump in $f_{esc,Ly\alpha}$ at $z \sim 6$, but at each redshift, our results agree well with the established literature. When fitting our data (blue line) compared to all the results (red line), we see an enhancement of $f_{esc,Ly\alpha}$, likely due to the constraints placed by the literature in the redshift range $2 < z < 4$. Our points do lie systematically above the points from the literature, indicating a greater SFRD based on the latest LAE LF of Thai et al. (2023). I note however that the LAE LFs of Konno et al. (2016) and Drake et al. (2017) have not been included in Figures 5.4 and 5.5 due to large uncertainties, especially at the highest redshifts and faint luminosities. These uncertainties contribute to unrealistically high (and poorly constrained) escape fractions based on these LFs.
Additionally, the choice of completeness cut has an impact. In Thai et al. (2023), a completeness cut of 1% was chosen (i.e. LAEs with completeness values $< 1\%$ are not taken into account in the LF determination), in order to maximise the sample size, while still negating the effect of the most incomplete and therefore uncertain sources. Studies have typically chosen different completeness cuts, or none at all. For example, de La Vieuville et al. (2019) chose 10%, rejecting a larger number of sources. In order to

check the effect this has, I recomputed $f_{esc,Ly\alpha}$ using the LF cut at 10% completeness. This yielded values similar to those seen in the literature : $10-15\%$ escape. Therefore I consider the results of this study completely consistent with what has been found previously, when considering a brighter integration limit ($0.04L*$).
The green dashed fit of Hayes et al. (2011) lies slightly higher than the literature data. I attribute this to the significant update in the UV LF since the publishing of that study (the UV LFs of Bouwens et al. (2009) and Reddy et al. (2008) were used for this fit). This emphasises the importance of the UV LF in these calculations and the value of the latest determination from Bouwens et al. (2022). The values used in this work, inclusive of dust and IMF correction are shown in Table 5.1.
The values I derived for $f_{esc,Ly\alpha}$ are considerably higher when I extend the LF integrations down to $0.0006L*$, particularly for the highest redshift bin, $z \sim 6$, where we see an increase of 0.4 dex with respect to the $0.04L*$ integration. In fact, this point is consistent with the fit to the data in B11 which is integrated to 0, i.e. taking into account the full population by assuming the validity of the two LFs down to 0. This large escape fraction value is unsurprising, as we see a high number density of faint galaxies in the LAE LF, and these populations typically have higher $f_{esc,Ly\alpha}$ (see Fig. 5.2, as well as Goovaerts et al. 2023; Chen et al. 2023; Goovaerts et al. 2024; Napolitano et al. 2024). In the $z \sim 6$ bin, $f_{esc,Ly\alpha}$ is consistent with 100%, i.e. a similar SFRD derived from LAEs as from the UV-selected population. While still consistent at 1σ with the fit derived by B11 (using an LF integration to 0), the point derived in this work lies above points from the literature. Note that no other studies have had access to the faint regime of LAEs used in this study and as such, the literature LFs I compare to are integrated beyond the limits of their samples to create this graph. Reasons for this enhanced $f_{esc,Ly\alpha}$ value for faint LAEs at $z \sim 6$ include the effect of the LAE incompleteness treatment, which acts most strongly for faint objects at the highest redshifts. Effectively, this would mean that there are, counted in the LAE LF, a significant number of faint LAEs not seen in the continuum.
This result may also point to a general scenario where faint galaxies (i.e. $M_{UV} \sim -13$) generally see an extremely high escape fraction of Lyman-α photons. This appears to be a clear effect when integrating down to the $L*$ limit our sample reaches : faint galaxies experience a higher escape of Lyman-α photons, especially at higher redshifts. This result is also in agreement with the results presented in Fig. 5.2 as in this plot, between $M_{UV} \sim -17$ and $M_{UV} \sim -13$, we see LAEs with exclusively high escape fractions (almost all above 10% and many around 100%). This result implies that at $z \sim 6$ and beyond, faint galaxies tend to be highly star-forming and chemically unevolved, which should allow high escape fractions. On the other hand, seen in the uncertainties in the faint end of the LAE LF, it is clear that there is still a large intrinsic scatter in the populations (once more in agreement with the results in Section 5.2).
It is worth noting, however, that if the IMF of these faint, reionisation-era LAEs is top-heavy with respect to the assumed Salpeter IMF, this may also explain an elevated $f_{esc,Ly\alpha}$. Such an IMF would increase the number of ionising photons, from massive stars, which would in turn increase the Lyman-α emission of the galaxy. A higher ionising photon production efficiency, ξ_{ion} has been observed for some LAEs (Matthee et al. 2021; Saxena et al. 2024, see also Simmonds et al. 2023) although there is no firm consensus

on how much higher. If ξ_{ion} were indeed to be $25.5 - 25.6$, this would mean a factor of $2 - 3$ more ionising photons produced. This would in turn mean more Lyman-α photons produced and an overestimation of $f_{esc,Ly\alpha}$ in our results by a similar factor (note that this would apply to all the results in Figs. 5.4 and 5.5). This is an important dependance on the high-mass slope of the IMF and the production of ionising photons, and could be particularly relevant to the faintest galaxies towards the epoch of reionisation, which are more likely to host exotic stellar populations.
In summary, I find that the LAE SFRD matches the UV SFRD during the final stages of reionisation, and is $\sim 20\%$ of it at redshifts between 3 and 5. For both bright and faint integration limits, we see this jump in the highest redshift bin ($z \sim 6$) compared to little evolution between redshifts of 3 and 5. This reflects a significant evolution of the LAE LF in this redshift bin, suggesting therefore that the LAE population evolves significantly between the end of reionisation ($z \sim 6$) and later times ($z \sim 4.5$). Although it is worth noting the uncertainty on the $z \sim 6$ result, I attribute this to a combination of several factors : a lower dust content in galaxies at this redshift and above combined with higher specific star formation rates in our sample of faint galaxies. As mentioned, the completeness correction for the LAE LF acts most strongly on the faint, high-redshift LAEs, making this a possible additional contributor.

5.4.2 Comparison of the global and individual $f_{esc,Ly\alpha}$ evolutions

It is immediately clear that the global evolution of $f_{esc,Ly\alpha}$ shows a more significant trend than the individual evolution, despite significant uncertainties, especially in the highest redshift bin. This becomes additionally clear when incorporating the agreement in the literature for the global evolution.
For the datasets presented here, this is likely due at least in part to the far greater sample size used in the global evolution : 2500 UV-selected galaxies and 600 LAEs, compared to ~ 100 LAEs for which $f_{esc,Ly\alpha}$ is calculated (Fig. 5.1). For a smaller sample such as the one used for the individual tracking of $f_{esc,Ly\alpha}$, particularly considering the lack of sufficient galaxies at redshifts greater than 6, any redshift evolution is washed out by the scatter in individual results. The results of B11 display a similar lack of evolution over $1.9 < z < 3.8$ when taking into account the significant scatter of individual galaxies. The same is even true for the more recent studies of Chen et al. (2023) and Napolitano et al. (2024), using Balmer decrements to calculate $f_{esc,Ly\alpha}$, albeit with smaller sample sizes. The intrinsic variety of escape scenarios for Lyman-α photons from different galaxies (even bearing in mind that all these systems are selected as LAEs) is evident.
The trend seen in the global redshift evolution of $f_{esc,Ly\alpha}$ (integration limit $0.0006L*$), towards $f_{esc,Ly\alpha} \sim 80\%$ around $z = 6$, is not seen in the individual results. Likely this is at least in part due to the incompleteness of the sample used to calculate $f_{esc,Ly\alpha}$ for individual galaxies at this redshift, as both LAEs with very small escape fractions and LAEs with very large escape fractions are harder to observe. For the LAEs with large escape fractions this difficulty comes from the faintness of the associated continuum : the galaxies with the highest $f_{esc,Ly\alpha}$ values tend to be faint in terms of UV magnitude (Fig. 5.2). This incompleteness should be accounted for in the two LFs used, so I do not expect this to play a significant role for the global $f_{esc,Ly\alpha}$ evolution.

Contrasting these two results, global and individual, it is clear to see that a large sample size, as well as considered completeness corrections, are necessary to observe any significant redshift evolution of $f_{esc,Ly\alpha}$. Indeed, further exploration of the faintest regimes of LAEs (and UV-selected galaxies) would be desirable in order to better constrain the faint end of the LFs and reduce the uncertainties on the highest-redshift points. For example, it is still very challenging to observe more than a few galaxies with $\log L_{Ly\alpha} < 40$ at $z > 5.5$ (see, for example, Fig. 3 of Thai et al. 2023).

I note also that the global comparison is effectively the Lyman-α escape fraction of a given volume of the Universe, bounded by the luminosity and redshift limits of the surveys used. This calculation takes into account all galaxies, not just those actually selected as LAEs, as is the case for the individual results. We might therefore reasonably expect to see a smaller escape fraction due to the inclusion of galaxies not selected as LAEs. In the lower and intermediate redshift bins, the results are consistent with the sample median shown by the red dashed line in Fig. 5.1, however in the highest redshift bin, the global calculation of $f_{esc,Ly\alpha}$ appears to yield a larger value. Taking the median of the galaxies from Fig. 5.1 above $z = 5$ would yield a higher result (36% escape), and it is likely that the data simply do not detect enough LAEs of high escape fraction at higher redshifts in the limited sample behind A2744. As this is just one cluster, extending these measurements to other clusters efficient in lensing galaxies above $z = 5$ is very desirable. The galaxies detected by their Lyman-α emission but not in the continuum (the black triangles in Fig. 5.2) naturally all have high escape fractions and are counted in the LAE LF, so this may go some way towards explaining the discrepancy we observe between our different methods of calculating $f_{esc,Ly\alpha}$. Additionally, and as mentioned, the completeness correction added to the LAE LF acts strongly in the faint, high-redshift regime so I also expect this to play a role. The results in Fig. 5.5 suggest that this may be a stronger role than the equivalent completeness correction added to the UV LF.

Contrary to the lack of similarity in redshift evolution in the global and individual $f_{esc,Ly\alpha}$ results, there is a similar trend in terms of an evolution with the UV magnitude of the host galaxy. In Sect.5.2 this is established as a much more significant trend and the results when comparing LFs support this. When integrating to fainter limits we see significantly higher values of $f_{esc,Ly\alpha}$ across the redshift range probed.

5.4.3 Overlap of the UV and LAE LFs

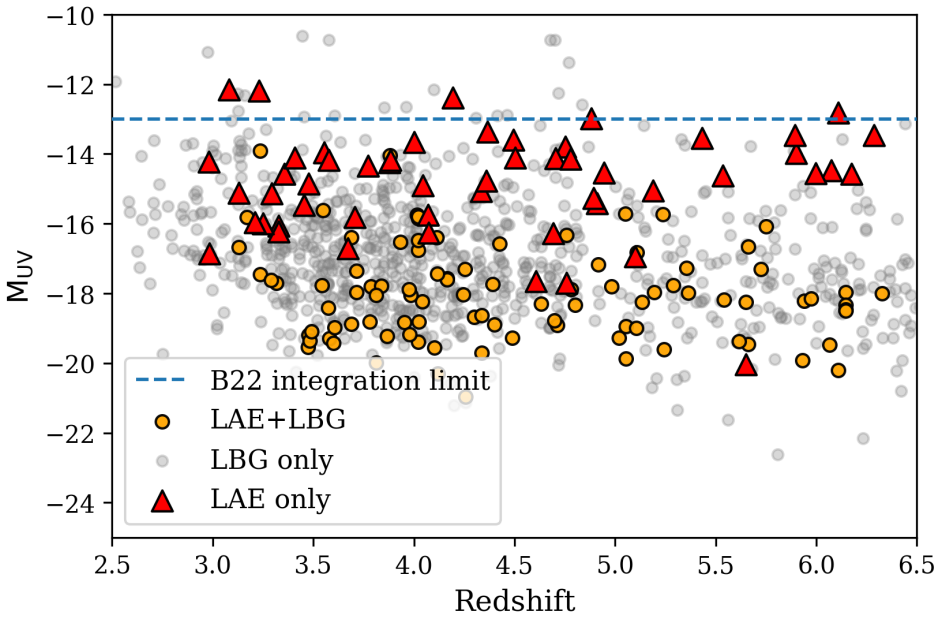

FIGURE 5.6 – Redshift and M_{UV} distribution of LAE and Lyman Break Galaxies (UV-selected galaxies, LBGs) from the sample in Goovaerts et al. (2023). Grey points denote LBGs, so are analogous to the UV-selected sample. Orange points denote objects that were selected as LBGs and LAEs and upward facing triangles indicate LAEs that were not detected at all in the HST imaging (Shipley et al. 2018). 2σ upper limits for the continuum of these objects have been estimated using the local noise in the region where they would have been detected in the HST image which would see the 1500 Å emission. The horizontal dashed line denotes the integration limit for the ρ_{total} calculation in Bouwens et al. (2022).

Here I revisit the assumption made in order to compare the two LFs using single integration limits in terms of $L*$ and treat them as representative of their respective "total" populations. This, in principle, is troublesome as there is no direct mapping between Lyman-α luminosity and UV magnitude ; for every given Lyman-α luminosity bin, there are a range of UV magnitudes that galaxies display. In fact, this encodes exactly what we want to measure, the escape of Lyman-α photons. It is clearly invalid to compare a LF based on just the brightest LAEs to the complete UV LF, including the faintest sources. Therefore, in order to make the comparison discussed above and shown in Figs. 5.4 and 5.5, we have to assume that the "total" populations are adequately represented with both LFs, within the UV and Lyman-α luminosity integration limits used. This approach is discussed at length in Hayes et al. (2011) and B11 and I revisit this in the context of the dataset used in this work.
That the LFs adequately represent both Lyman-α and UV populations is reasonably evident for the brightest objects, they are certain to be included in their respective surveys.

This is less evident for the fainter regimes explored. For example, are the faintest LAEs included in the LAE LF adequately represented by the faint end of the UV luminosity function ? In order to assess this, we can look at the faintest LAEs and compare them to the UV magnitude regimes included in the UV LF of Bouwens et al. (2022).
It is by now well established that certain LAEs remain undetected in even the deepest photometric searches to date (see, for example, Bacon et al. 2015; Maseda et al. 2018; Sobral &Matthee 2019; Maseda et al. 2020a; de La Vieuville et al. 2020; Goovaerts et al. 2023). Additionally, some LAEs display faint continuum that would not pass the criteria for many UV-based selections, be they based on colour-colour cuts (Stark et al. 2010; Pentericci et al. 2011, 2018) or photometric redshifts (Caruana et al. 2018; Kusakabe et al. 2020; Goovaerts et al. 2023). I note that preliminary searches conducted by JWST/NIRCam in lensing clusters yields almost exactly the same number of undetected LAEs (see Goovaerts et al. 2024 and Chapter 3). On the other hand, nebular lines are detected in these systems, so they are likely to be real detections (Maseda et al. 2023). With future, deep JWST (and HST) surveys, we will be able to shed more light on this issue.
This raises concerns as to whether the UV LF truly represents the entirety of the galaxy population, or whether there are a significant number of 'UV-dark' LAEs which are counted in the LAE LF but not in the UV LF. This is important to consider given the high values of $f_{esc,Ly\alpha}$ I derive when integrating to $0.0006L*$ (Fig. 5.5).
A way in which we can assess which of these two cases is closer to reality is to compare the UV magnitude regime where these HST-dark LAEs are expected to lie to the regime covered by the UV LF in Bouwens et al. (2022) and the integration limits used. Upper limits on the UV magnitude of these LAEs can be calculated by manually extracting the continuum level from the HST images, as in Goovaerts et al. (2023) and throughout this work. These objects, denoted by upward-pointing arrows to indicate upper limits on M_{UV}, are displayed on Fig. 5.6. This shows that for the clusters considered by the UV LF in question, and for the photometry in question, the UV-dark LAEs would be expected to appear around $M_{UV} = -16$, with many residing between this and $M_{UV} = -14$, and some down to $M_{UV} \sim -12$.
The UV LF in Bouwens et al. (2022), inclusive of the correction for selection incompleteness, extends past $M_{UV} = -16$ at all redshifts relevant for this work, and extends past $M_{UV} = -14$ at $z \sim 3$ and $z \sim 6$, and close to it at $z \sim 4$ and $z \sim 5$. At $z \sim 3$, the coverage extends all the way to $M_{UV} = -12$. The integration limit ($0.0006L*$) used for the calculation of ρ_{total} from the UV LF corresponds to $M_{UV} = -13$, as denoted by the horizontal dashed line in Fig. 5.6.
There are four LAEs estimated to have upper UV magnitude limits fainter than this in the sample of four lensing clusters in Goovaerts et al. (2023). As the non-detection of these LAEs likely depends at least in part on the relative depths of the spectroscopy and photometry, it is difficult to estimate what effect this has across the sample, but we can reasonably expect this to have a minor effect, considering the small number of LAEs in this position in comparison to the sample size used for the two LFs.
We can additionally reassure ourselves by comparing what the UV luminosities should be from the faintest LAEs assuming different levels of Lyman-α escape. The faintest LAEs included in the LAE LF are no fainter than $L_{Ly\alpha} = 10^{39}\,\text{erg}\,\text{s}^{-1}$, which equates to an

absolute UV magnitude of $M_{UV} \sim -10.4$ assuming 100% Lyman-α escape (meaning this value is a lower (faint) limit on the absolute UV magnitude). If we assume a more likely $f_{esc,Ly\alpha}$ value of our sample median from Section 5.2 of 22.5%, this UV magnitude becomes $M_{UV} = -12.2$. This is very faint compared to the reach of the UV LF I used, below the integration limit of $M_{UV} = -13$. However, using this integration limit and an escape fraction of 22.5%, I recover a value $L_{Ly\alpha} = 2.4 \times 10^{39}\,erg\,s^{-1}$. There is only one LAE in the sample close to this luminosity (see Figure 3 of Thai et al. 2023). On the other hand, following this analysis shows that faint LAEs with $L_{Ly\alpha} < 10^{40}\,erg\,s^{-1}$ are not accounted for in the UV LF with its integration limit set at $0.0006L*$ as in Fig. 5.5 if they have $f_{esc,Ly\alpha} > 95\%$. Across the board, this effect will bias the results for $f_{esc,Ly\alpha}$ low.

We can perform the same exercise in an inverse manner, to assess whether we are likely to see the Lyman-α emission from the faintest UV objects included in the UV LF. The LAE luminosity expected from a galaxy of $M_{UV} = -12$ is $10^{39.6}\,erg\,s^{-1}$, assuming 100% Lyman-α escape. Assuming 22.5% escape, this value will be $10^{39.0}\,erg\,s^{-1}$. So for galaxies of this absolute magnitude, we can expect to account for all the LAEs in the population (when taking into account the completeness correction). However the escape fraction can be lower (down to 0%), meaning that the objects of very low UV magnitude and very low Lyman-α escape will be missed. Unlike missing objects in the UV selection, this biases our results towards high Lyman-α escape values. This counter-bias can alleviate the bias introduced by missing UV-faint objects as described in the previous paragraph, and indeed this is the motivation behind choosing one value of $L_\star$ down to which both LF integrations are calculated.

In summary, and in light of the high values for $f_{esc,Ly\alpha}$ found in Fig. 5.5, for these results to be overestimated, a large population of continuum-undetected LAEs must be playing a role (together with the effects introduced by their incompleteness) in the LAE LF, which are not accounted for in the UV LF, even with the completeness treatment described in Bouwens et al. (2022). This potential effect is important for studies looking to evaluate the total SFRD of the Universe.

Alternatively, if we assume that this effect is negligible and the high $f_{esc,Ly\alpha}$ value derived at $z \sim 6$ when including the whole faint sample from this work is reflecting a real similarity between $SFRD_{Ly\alpha}$ and $SFRD_{UV}$, this indicates that galaxies at $z \gtrsim 6$ are emitting significantly higher amounts of Lyman-α photons than later in the Universe. This supports a picture of galaxies towards reionisation as chemically unevolved and highly star-forming ; creating a lot of Lyman-α emission and allowing it to escape.

5.4.4 The LAE contribution to reionisation

Seeing as the escape of Lyman-α photons is a crucial quantity for the assessment of the LAE contribution to cosmic reionisation, I can now revisit this in light of the results for $f_{esc,Ly\alpha}$. There is significant debate in the literature about the relative contribution of the LAE population to reionisation, (see, for example Cassata et al. 2011; Drake et al. 2017; de La Vieuville et al. 2019; Matthee et al. 2022; Thai et al. 2023). All of these results are, naturally, dependent on the $f_{esc,Ly\alpha}$ values assumed in the various studies. The $f_{esc,Ly\alpha}$ value used to calculate this contribution is often pivotal in its classification. I can now recalculate the LAE contribution taking into account the results of this study.

TABLE 5.3 – The LAE contribution to reionisation.

Key	$\rho_{Ly\alpha}$ (10^{39})[erg s^{-1} Mpc^{-3}]	$f_{esc,Ly\alpha}$ [%]	Contribution [%] ($f_{esc,LyC} = 0.4\%$)	Contribution [%] ($f_{esc,LyC} = 10\%$)
T23, median	47.31 ± 37.63	22.5	9^{+16}_{-7}	260^{+210}_{-50}
T23, $z > 5$	47.31 ± 37.63	36	6^{+10}_{-4}	160^{+130}_{-30}
dLV19, median	9.52 ± 5.65	22.5	$1.9^{+1.1}_{-0.8}$	52^{+31}_{-21}
dLV19, $z > 5$	9.52 ± 5.65	36	$1.2^{+0.7}_{-0.4}$	52^{+31}_{-21}
T23 GSF, median	103.2 ± 76.5	22.5	20^{+15}_{-5}	560^{+420}_{-150}

Notes. The key indicates the provenance of the values used in columns 2 and 3, in the order they appear in the table. GSF indicates where the general Schechter function was used rather than the modified Schechter function. Values of $\rho_{Ly\alpha}$ come from the LAE LF integrated to $0.0006L*$ ($\log L_{Ly\alpha} \sim 39$). T23, dLV19 refer to Thai et al. (2023) and de La Vieuville et al. (2019) respectively.

I start by considering the ionizing emissivity from star forming galaxies, using the following formalism (e.g., Madau et al. 1999; Robertson et al. 2013; Duncan &Conselice 2015) :

$$\dot{n}_{ion}(z) = \rho_{UV}(z)\, \xi_{ion}\, f_{esc,LyC} \tag{5.5}$$

where $\dot{n}_{ion}$ is expressed as the product of the UV luminosity density $\rho_{UV}(z)$, global UV luminosity to ionizing photon conversion factor ξ_{ion} (Matthee et al. 2016a; Lam et al. 2019) and the ionising photon escape fraction $f_{esc,LyC}$. I reformulate Eq. 5.5 as we are interested in the quantity $\dot{n}_{ion}(z)$ for the LAE population only :

$$\dot{n}_{ion,Ly\alpha}(z) = \rho_{Ly\alpha}(z)\, \xi_{ion}^{Ly\alpha}\, f_{esc,LyC} \tag{5.6}$$

where $\rho_{Ly\alpha}$ is the Lyman-α luminosity density, $\xi_{ion}^{Ly\alpha}$ is the conversion factor of the observed Lyman-α luminosity to the number of ionising photons and $f_{esc,LyC}$ is the Lyman continuum escape fraction of the LAEs. Ignoring collisionally excited emission and using Case B recombination (Brocklehurst 1971; Osterbrock &Ferland 2006, see also Matthee et al. 2021) as well as the intrinsic flux ratio between Lyman-α and $H\alpha$ of 8.7, the ionizing emissivity of LAEs, corrected for $f_{esc,Ly\alpha}$, is written as :

$$\dot{n}_{ion,Ly\alpha}(z) = \frac{\rho_{Ly\alpha}(z) \times f_{esc,LyC}}{8.7\, c_{H\alpha} \times f_{esc,Ly\alpha}\, (1 - f_{esc,LyC})} \tag{5.7}$$

where $c_{H\alpha}$ is the coefficient factor of the $H\alpha$ emission line, $\sim 1.25 - 1.35 \times 10^{-12}$ for Case B recombination. It remains to estimate the individual parameters appearing in the above function.

- The LAE luminosity density ($\rho_{Ly\alpha}$) : this parameter was presented in Sect. 5.3.2.

- The escape fraction of Lyman-α photons, $f_{esc,Ly\alpha}$. I cannot correct $\rho_{Ly\alpha}$ by the escape fraction derived in Sect. 5.3.2 as this, by construction, corrects $\rho_{Ly\alpha}$ to the total value of

the parent population (ρ_{total}) which I took from Bouwens et al. (2022). I can, however, use the value derived in Sect. 5.2. I discuss both the sample median, $f_{esc,Ly\alpha} = 22.5\%$ and the sample median for the LAEs at $z > 5$, $f_{esc,Ly\alpha} = 36\%$.

- LyC escape fraction, $f_{esc,LyC}$: This parameter is poorly understood, in particular at high redshift, due to the increasing IGM neutrality which absorbs Lyman continuum photons along the light of sight. However, recent progress has been made in local galaxies (high-redshift analogues) (Flury et al. 2022; Izotov et al. 2024) and in LAEs up to $z \sim 3$ (Liu et al. 2023b; Kerutt et al. 2024; Pahl et al. 2024; Jung et al. 2024). However, results from these studies, as well as simulations (Choustikov et al. 2024a; Yuan et al. 2024), suggest that there is a significant scatter in the $f_{esc,LyC}$ across the LAE population. Therefore placing one value on $f_{esc,LyC}$, like $f_{esc,Ly\alpha}$, is a simplification. Many observational studies point to values between 10% and 15% : Kerutt et al. (2024) derive an underlying population value of 12%, Jung et al. (2024) obtain values between 3% and 15%, Liu et al. (2023b) give an upper limit of 16% and Izotov et al. (2024) find values between 1% and 34%, with most of their galaxies having $f_{esc,LyC} < 15\%$. Based on the SPHINX simulations (Garel et al. 2021) and the model for Lyman continuum escape developed by Rosdahl et al. (2022), $f_{esc,LyC}$ is $1.17\%, 0.4\%$ at $M_{UV} = -17, -13$ (noting that this last result is for all galaxies, not just those selected as LAEs).

The ability to turn Eq. 5.7 into a summation, with each LAE contributing its own $\rho_{Ly\alpha}$, $f_{esc,Ly\alpha}$ and with $f_{esc,LyC}$ consequently following a relation such as those presented in Rosdahl et al. (2022), Choustikov et al. (2024a) or Izotov et al. (2024) would be an improvement. Increased statistics, especially for faint LAEs and at redshifts greater than 5 would be necessary to make this approach feasible. This is within reach for JWST in the coming years, as observed samples increase in size and more faint galaxies are uncovered. A very recent approach by Choustikov et al. (2024b) attempts this individual approach for a large sample of JWST/NIRCam-observed galaxies (not just LAEs) (observed by the JADES programme, Eisenstein et al. 2023). The authors conclude that faint galaxies ($M_{UV} \geq -18.5$) are potentially responsible for $\sim 80\%$ of the reionisation budget. The majority of our sample of LAEs fall within this bracket (see, e.g. Fig. 5.6).

With $\dot{n}_{ion,Ly\alpha}$, at $z = 6$, from Eq. 5.7, I can compare this value to the ionising emissivity required for reionisation as derived by Bouwens et al. (2015a), $\dot{n}_{ion,crit} = 50.92$ (noting that this value uses a fiducial clumping factor $C_{HII=3}$). In Table 5.3, I show the range of results, applying different values for $\rho_{Ly\alpha}$, $f_{esc,Ly\alpha}$ and $f_{esc,LyC}$. For $\rho_{Ly\alpha}$ derived from our results, (the LF of Thai et al. 2023) I find LAE contributions ranging from minor (5-10%) for a low $f_{esc,LyC}$, 0.4% to dominant $> 100\%$ for $f_{esc,LyC} = 10\%$. Changing $f_{esc,Ly\alpha}$ between the sample median and $z > 5$ median does not qualitatively change the outcome. As $f_{esc,LyC}$ changes more significantly depending on the chosen value, this represents the main effect on the outcome. In several cases we see unrealistic contributions ($> 100\%$) for LAEs based on $f_{esc,LyC} = 10\%$, suggesting that this value may be too high and not representative of our whole sample. Crucial work remains to correlate $f_{esc,LyC}$ with observable parameters (such as Lyman-α parameters) at higher redshifts and constrain the escape of ionising photons for the LAE population at $z \sim 6$ and above.

I investigate the effect on the LAE reionisation contribution in the case of a completeness cut in the calculation of the LAE LF at 10%. I take the results of de La Vieuville et al.

(2019) as emblematic of this scenario (as mentioned, the LF of Thai et al. (2023) is consistent with that of de La Vieuville et al. (2019) if this cut is applied). In this case, the contribution to reionisation derived for the LAE population is significantly less ($1-2\%$ for $f_{esc,LyC} = 0.4\%$ and $30-50\%$ for $f_{esc,LyC} = 10\%$). This emphasises the sensitivity of these results to the completeness treatment applied for the LAE population.
I additionally show the difference between the modified Schechter function which I have chosen to adopt throughout this study and the general Schechter function (noted GSF in Table 5.3). Using the general Schechter function roughly doubles the LAE contribution to reionisation.
Highlighting the effects of both the function chosen to fit the LAE LF and the completeness cut applied serves to reinforce the need for a larger sample at $z > 5$ and for faint galaxies. Better statistics in this parameter space will constrain the faint end of the LF more strongly, discriminating between the modified and general Schechter functions. With deeper observations of faint galaxies, the completeness for the faint LAEs will also improve (i.e. the sample will be more complete at a given Lyman-α luminosity) and the chosen cut will become a less important factor.
The chosen value of $f_{esc,LyC}$ is clearly determinant in this calculation with LAEs contributing very little for small values of $f_{esc,LyC}$ and providing the dominant contribution for reasonable values of $f_{esc,LyC}$ observed in many lower-redshift LAEs and low-mass galaxies acting as high-redshift analogs. Using the $\rho_{Ly\alpha}$ from Thai et al. (2023) and $f_{esc,Ly\alpha} = 36\%$, a sample average $f_{esc,LyC}$ of just 6.5% would be enough for LAEs to provide all the necessary ionising photons at $z = 6$. If the values of $f_{esc,LyC}$ observed in these low-redshift LAEs are maintained across the LAE population into reionisation, it is certainly conceivable that these galaxies could have been responsible for reionisation in its entirety. I note that the results in this study do not constrain the reionisation scenario beyond $z = 6.7$ and that LAE LFs at $z \geq 7$ are needed to track the contribution of LAEs further into the EoR.

To end this chapter, I add a brief word on the future prospects for this type of study. At the moment, it is challenging to improve the two LFs used in this work, as they already use the full extent of deep observations in lensing clusters from HFF and MUSE. Further clusters to be included in this sample are desirable, particularly to better constrain the high-redshift ($z \sim 6$), faint end of the LAE LF. This will be made possible through further MUSE-observed lensing clusters, such as those presented in Claeyssens et al. (in prep). This will also help to bin the results in smaller redshift bins to better constrain the precise evolution in the range $3 < z < 6$. Observations of LAEs at higher redshift, from JWST, such as Chen et al. (2023); Tang et al. (2024); Lin et al. (2024); Witstok et al. (2024); Nakane et al. (2023) are starting to build larger sample sizes but not yet of the quantity of LAEs and UV-selected galaxies used for the results in this work. Particularly intrinsically faint galaxies have poor statistics, although this can be improved with the continuing observations of lensing clusters by JWST/NIRCam and JWST/NIRSpec.
On the other hand, it is possible, with further JWST observations, photometry and spectroscopy, to improve the $f_{esc,Ly\alpha}$ determinations for individual galaxies. The Balmer decrement provides accurate estimations of dust attenuation along with SED fitting utilising a greater number of photometric bands and a more extended coverage. Studying

these systems in more detail will reveal the range of different escape scenarios leading to the varied $f_{esc,Ly\alpha}$ values that are observed. This can, in turn, lead to better understanding of galaxy evolution around the epoch of reionisation and how LAEs affect this process.

6 Conclusions, prospects and the future of the field

"The history of astronomy is a history of receding horizons."

— *E. Hubble.*

Author's note on content : *In this final chapter, I will summarise the work done in the thesis and the conclusions reached therewith. I offer prospects based on the work and the current state of this rapidly evolving field with the hope that this evolution does not render them obsolete within a few months. Finally I will detail the progress I hope to make on the outstanding areas of interest touched on by this thesis and how these tie into the current state of the field.*

Author's note on context : *I find, as I write this in June of 2024, exactly three months from the end of my thesis, that I could keep going for another three years. Every day new results in my areas of interest and those covered by this thesis appear online, with barely enough time to read them all, let alone investigate as much as one would like. I am fortunate enough to be able to continue my research at the Space Telescope Science Institute in Baltimore, Maryland, starting from October of this year. I hope to continue addressing the areas of interest of this thesis as well as others connected to Lyman-α physics and reionisation-era galaxy evolution.*

6.1 Summary and key results

In the previous three chapters, the results from my doctoral research have been outlined, and I summarise them as such :

Chapter 3 :

— LAEs are on average more highly star-forming, with bluer UV slopes than the UV-selected population at the same redshifts ($2.9 < z < 6.7$).
— We extend the general trend for stronger LAEs (those of higher $EW_{Ly\alpha}$) being UV-fainter and having steeper UV-slopes.
— When considering the stellar mass of the LAE sample, a slightly enhanced star-forming MS is seen compared to a similar UV-selected sample, however the two are within 1σ uncertainty for our sample.

— However, a significant difference is observed between our low-mass sample and MS fits derived from higher-mass galaxies (at the same redshifts). This suggests an enhanced sSFR and therefore an enhanced role in reionisation for low-mass galaxies, but no special place for LAEs in this process.

Chapter 4 :

— The results for the LAE fraction, $X_{\rm LAE}$, agree with the literature on the subject, showing an increase in IGM neutrality towards $z \sim 6$. The results suggest that the IGM becomes neutral more rapidly than some similar studies, however there is a lot of scatter in the data.
— In addition to the scatter in the data, it is vitally important to take into account sample selection effects and completeness treatments while considering $X_{\rm LAE}$. Samples selected using different observing techniques can yield different results.
— In assessing the evolution of $X_{\rm LAE}$ with UV magnitude and $\rm EW_{Ly\alpha}$, a greater LAE fraction than expected is seen among UV-faint galaxies with small $\rm EW_{Ly\alpha}$.
— This result is most stark close to the EoR ($z \sim 6$), and is suggestive of a result seen in individual LAEs within the EoR : UV-bright galaxies are capable of ionising a bubble in the neutral IGM, allowing Lyman-α emission to escape, albeit at low $\rm EW_{Ly\alpha}$ values.

Chapter 5 :

— When estimating $\rm f_{esc,Ly\alpha}$ values from individual galaxies, we see no significant evolution with redshift, although we lack sufficient statistics at the highest redshifts ($z \sim 6$). This is however not surprising given the results in the literature and the scatter of the individual data points.
— A much tighter correlation is observed between $\rm f_{esc,Ly\alpha}$ and UV magnitude. This evolution is fit by the relation : $\log(\rm f_{esc,Ly\alpha}) = (0.28 \pm 0.03)\, M_{UV} + (4.3 \pm 0.6)$, although it is possibly impacted by MUSE line-incompleteness effects at $\rm M_{UV} \gtrsim -17$.
— When assessing $\rm f_{esc,Ly\alpha}$ using the LAE and UV LFs, a more significant evolution is seen, in agreement with other derivations in the literature when integrating the LFs to a bright limit, $0.04L*$.
— When integrating down to the faint limit the LAE and UV samples reach, $0.0006L*$, $\rm f_{esc,Ly\alpha}$ becomes consistent with 100% around $z \sim 6$. When fitting to all the data, $\rm f_{esc,Ly\alpha}$ is consistent with 100% around $z \sim 8$.
— Considering the LAE contribution to reionisation in light of these results, I found that for small ionising photon escape fractions ($\rm f_{esc,LyC} < 1\%$) the LAE contribution must necessarily be small ($< 20\%$, and in most cases, $< 10\%$).
— However, for larger values of $\rm f_{esc,LyC}$, such as have been observed in LAEs and in other high-redshift analogues, of around 10%, the LAE population could have contributed enough ionising photons to keep the Universe reionised at $z = 6$.
— The value of $\rm f_{esc,LyC}$ chosen is determinant in this calculation, and the chosen form of the LAE LF (modified or general Schechter function), as well as the completeness cut chosen also play a major role.

In order to round off the key points of this thesis, I give what I consider to be the "take-home messages" from each chapter : the most important results. In Chapter 3, LAEs are found to not be so different from UV-selected galaxies at the redshifts considered. Rather it is the low-mass range probed by this study that sets these galaxies apart.
Chapter 4 found a statistical signature of UV-bright LAEs finding it easier to ionise bubbles and therefore allowing Lyman-α photons to escape. Around the same time as this was published, the first high-redshift LAEs were published using JWST data and were indeed UV-bright galaxies showing weak Lyman-α emission.
Chapter 5 found a much stronger trend for $f_{esc,Ly\alpha}$ with the UV magnitude of the host galaxy rather than the redshift. All our results point to the faint LAE population having much higher escape fractions of Lyman-α photons than the bright population. Using the derived value for $f_{esc,Ly\alpha}$ from our sample, LAEs could provide all of the ionising photons for reionisation for values of $f_{esc,LyC}$ which have been observed in lower-redshift LAEs (as low as 6.5% could be enough, values around $10-20\%$ have been observed in several cases).

6.2 Perspectives and the near future

Given the incredible success of the JWST in many fields of reionisation-era observational astrophysics, further enquiry with this telescope represents a natural progression of the investigation into the redshift regimes I have explored during my doctoral studies. LAEs and Lyman-α emission have been a hot topic in and around the epoch of reionisation with many objects showing Lyman-α emission in an increasingly neutral Universe (e.g. Bunker et al. 2023; Witten et al. 2023; Witstok et al. 2023; Whitler et al. 2023b; Chen et al. 2023).
Progress is being made all the way from low redshift studies aiming to constrain details of Lyman-α escape and correlations with complex galaxy physical parameters (e.g. Izotov et al. 2020; Hayes et al. 2023; Izotov et al. 2024), through medium redshift studies ($1 < z < 6$) looking at large samples of LAEs (Kerutt, J. et al. 2022; Kerutt et al. 2024; Tang et al. 2024; Choustikov et al. 2024a; Napolitano et al. 2024) to studies of Lyman-α emission in the highest-redshift objects hitherto observed (Endsley et al. 2022; Tang et al. 2023; Saxena et al. 2023; Bunker et al. 2023; Nakane et al. 2023; Witstok et al. 2024).
Exploring all of these types of study, and redshift ranges, is crucially important in order to bring about a comprehensive understanding of LAEs and the role they play in reionisation. At the redshifts concerned by this thesis, where large samples are possible, but we are still effectively looking at the populations responsible for reionisation, JWST can help us make huge strides, with the measurement of rest-optical properties.
As in Chapter 3, NIRCam data can help us improve SED fitting and derive accurate stellar masses. NIRSpec has the potential to be even more useful, as it gives us access to the informative Balmer series lines, Hα and Hβ, as well as the OIII emission line.
These emission lines offer information about several key galaxy properties, such as the SFR from the Hα line flux, dust attenuation from the Hα/Hβ ratio and the gas-phase metallicity from usual diagnostics, such as the OIII/Hβ and NII/Hα line ratios. Accurately estimating the dust attenuation of these galaxies from the Balmer decrement is especially interesting,

as with dust-corrected SFRs, one can derive very accurate values of $f_{esc,Ly\alpha}$ (Chen et al. 2023; Lin et al. 2024; Napolitano et al. 2024). This may help us to constrain any redshift evolution of $f_{esc,Ly\alpha}$, more than the results in Chapter 5, which have considerable uncertainties on $f_{esc,Ly\alpha}$ for individual galaxies as well as population scatter. The considerable interest of constraining dust content in LAEs is expanded upon in the following section.

The lensed, low-mass LAE population is additionally a good place to perform studies of low-metallicity galaxies, (Maseda et al. 2023; Roberts-Borsani et al. 2024), as well as searching for ultra-low metallicity galaxies, i.e. populations of stars forming from pristine (or near-pristine) gas (e.g. Vanzella et al. 2023, a lensed LAE at $z = 6.6$ hosting an extremely low-metallicity population - OIII/H$\beta = 0.55 \pm 0.15$). Being able to estimate the metallicity of these galaxies allows us to correlate this with Lyman-α emission and other galaxy parameters, as well as pre-select any interesting low-metallicity sources for potential follow-up. These low-metallicity, highly star-forming sources are ideal sources to further the understanding of galaxy properties in the very early Universe. They make excellent laboratories to study the ionisation conditions, star-formation and ISM conditions at early times. This sort of analysis, with consequences for high-redshift galaxy evolution, is already performed on low-redshift, resolved sources (e.g. Berg et al. 2022; Mingozzi et al. 2022; Hayes et al. 2023; Mingozzi et al. 2024), and can be extended to higher redshifts with high-quality, deep JWST data from NIRSpec and NIRCam.

NIRCam has already proven extremely helpful in the characterisation of the rest frame optical properties of reionisation era LAEs, as in Chapters 3 and 5, applied to LAEs, as well as Chen et al. (2023), Tang et al. (2023), Iani et al. (2023), Tang et al. (2024), Lin et al. (2024), Napolitano et al. (2024). These results are especially interesting when considering intrinsically faint LAEs, such as those accessed with observations of lensing clusters. For this reason, the GLIMPSE survey (PI : H. Atek) represents a huge leap forward in deep lensing cluster imaging [1]. GLIMPSE will obtain ~ 120 hours of exposure time across 9 NIRCam filters, aiming to reach an intrinsic depth of 33-35 mag (AB). The previous limits from JWST programs (and the HFF) was around 31 mag. These observations will push the detections of faint galaxies in and around the EoR further, below the faintest objects detected so far (see, for example, Fig. 3.11 and the faintest LAEs detected by UNCOVER around stellar masses of $10^6 - 10^8\,M_\odot$). Exploring these mass regimes at redshifts relevant to reionisation represents one of the most intriguing challenges of the coming years. Massive galaxies and bright objects, so-called "low-hanging fruit" are always the first to receive attention in new data, however these populations of low-mass galaxies are far more numerous and likely far more important for global processes such as reionisation.

A further effort will take place in the Abell 1689 (A1689) lensing cluster, a lower-redshift cluster than the HFF, meaning maximum magnification efficiency occurs at intermediate redshifts ($1 < z < 4.5$), rather than higher redshifts like the HFF ($z > 6$). At $z = 2$ however, there is a large area of magnification $\mu > 5$ ($3.8\,\mathrm{armin}^2$), several times greater than the HFF clusters which have been the focus of this thesis and of the majority of JWST observations so far. This means that at these redshifts, a large number of highly

1. There are a huge number of science goals and potential avenues for exploration in the GLIMPSE project but I focus here on the interests for myself and the community working on faint LAEs in particular.

magnified galaxies will become accessible with the combination of MUSE and JWST observations (PI : A. Claeyssens, Programme IDs : 0111.B-0296(A) and 5782). For MUSE LAEs in the redshift range $2.9 < z < 4.5$, observing this cluster becomes very intriguing, simply due to the number of faint galaxies expected, and the impact this could have on the LAE LF, such as the LF from Thai et al. (2023) used in Chapter 5. Increased statistics in the faint bins of these LFs, and equally in the low-mass regions of plots like Fig. 3.11, are of paramount importance for our understanding of low-mass galaxies beyond the local universe. Intermediate redshifts are the ideal place to explore these populations as they are not yet observable in the high-redshift universe [2] hence, if we can construct statistically meaningful samples of low mass galaxies ($\sim 10^6 M_\odot$) they can give insights into the main contributors to reionisation at redshifts greater than 6, where direct observations are much more challenging.

For LAE science this type of observation is equally important. It is to be expected that in the intermediate-to-high redshift universe, low-mass, star-forming galaxies would exhibit Lyman-α emission, however is this the case ? With these very deep observations of lensing clusters, and JWST/NIRCam data, it will be possible (with decent statistics) to explore the fraction of LAEs per galaxy stellar mass bin. This would give insights into both the evolution of the LAE population and their expected effect on reionisation. We saw in Chapter 4 that towards reionisation we see more bright galaxies (in this case $M_{UV} < -18$ exhibiting Lyman-α emission, especially with small $EW_{Ly\alpha}$. The question of relative contribution to reionisation remains then : on one hand the UV-bright galaxies clearing ionised bubbles, allowing Lyman-α radiation to escape, and on the other hand the more numerous population of low-mass galaxies, which may not be observable by their Lyman-α radiation above $z = 6$, but through investigation at intermediate redshift, could be shown to have a significant impact. If these galaxies all lie above the typical MS fits, as is suggested by the results in Chapter 3, and if a high fraction of LAEs is seen in low-mass bins at intermediate redshift, we can infer that these populations are likely having a significant impact at $z > 6$, despite the difficulty in observing them. The study of the star-formation in these low-mass populations is then by no means concluded.

The study of faint LAEs contains further avenues for exploration, for example, if we consider the inverse scenario to that detailed above. Instead of the faint galaxies that may not be exhibiting Lyman-α emission at higher redshifts, what can we say about the faint LAEs that are not seen in the UV continuum ?

6.2.1 UV-dark LAEs, observations and explanations

A recurring theme throughout Chapters 3, 4 and 5 has been LAEs observed with MUSE which are undetected by the imaging we are using to complement the IFU spectroscopy. This limits what we can discover about these galaxies, as we have only a Lyman-α detection (although we know these are likely to be real as nebular lines have been detected in these systems such as in Maseda et al. 2023). It also limits therefore what we can know about the whole population of LAEs as in any analysis we do based on the continuum of these galaxies, these undetected LAEs are missed out. These LAEs may have different

2. Let's see what GLIMPSE can do about this. Exciting times ahead.

properties to those we observe, and it's important to explore avenues as to why we do not detect these galaxies in the continuum.
An easy answer is that the photometry is not deep enough. If the MUSE observations are very deep (i.e. a very long exposure time) it stands to reason that in shallow photometry, not all LAEs will be detected. Certainly, in some instances, this is the case.
On the other hand, this study uses the HFF, the deepest available photometry of lensing clusters, and while some MUSE observations are deep (10+ hours, see Richard et al. 2021), some are much shallower, such as AS1063, which has only 3 hours of MUSE exposure. Despite this, AS1063 still has continuum-undetected LAEs.
Another possible answer lies in the interplay of stellar emission (emitted in the UV), Lyman-α emission, which traces the hydrogen in a galaxy, and the far infrared emission (FIR) which traces the dust content in a galaxy. If, for example, the dust content of a galaxy obscures much of the stellar light, but the Lyman-α emission manages to escape through radiative transfer in an extended hydrogen cloud, it is possible that the UV continuum from the galaxy would be very faint (so faint as to make it undetectable with a reasonable exposure time), and the Lyman-α emission much brighter. We generally think of LAEs as dust-poor galaxies, but this may be an observational bias based on the fact that we would not observe the continuum for this type of LAE where the dust strongly attenuates the UV continuum [3].
There are several avenues of exploration available to support/disfavour this option. One is observations of LAEs in the FIR and radio parts of the spectrum. This can trace the dust content of the LAEs, and give estimates of the SFR which has been absorbed and re-emitted by dust. Additionally, targeting lines like the CII emission line can give us an independent measure of the total SFR of the galaxy, to be compared to the Lyman-α and dust emission.
These observations would require interferometers like the Atacama Large Millimetre Array (ALMA) or the Northern Extended Millimetre Array (NOEMA), which can observe at micron and millimeter wavelengths. This is required to target the peak of the dust continuum ($50-150\,\mu m$ rest frame) (Blain &Phillips 2002; Casey 2012; Casey et al. 2014). It is however extremely challenging to observe intrinsically faint galaxies at reionisation-era redshifts with these telescopes, as sufficient sensitivity for a detection usually requires an unfeasible exposure time. Certain efforts have been undertaken on brighter galaxies, such as the ALPINE survey (Le Fèvre et al. 2020), the REBELS survey (Dayal et al. 2022) and a gravitationally-lensed $z = 6$ galaxy from the ALC Survey (Valentino et al. 2024).
Observing the HST-dark LAEs considered by this thesis is not possible with instruments like ALMA within reasonable exposure time. It is more fruitful to consider a proxy, for example a galaxy for which the continuum is detected but for which $\mathrm{SFR}_{\mathrm{Ly}\alpha} > \mathrm{SFR}_{\mathrm{UV}}$. Such a proxy would allow us to choose a relatively brighter galaxy, making observations easier. Fig. 6.1 shows the best two candidates from the four HFF clusters used in Chapter 3, henceforth denoted 1063z6 and 2744z4 after their parent clusters and redshifts. Also on this plot are shown the (continuum-) detected and undetected LAEs in these four lensing

3. Note also that if the UV continuum is undetectable, it is impossible to detect Lyman-α emission from this source in a survey that follows up continuum detections with spectroscopy. Only in blind searches like those made possible by MUSE's IFU spectroscopy would these sources show up.

clusters, emphasising the significant presence of the undetected population : $\sim 20\%$ of the total LAEs.

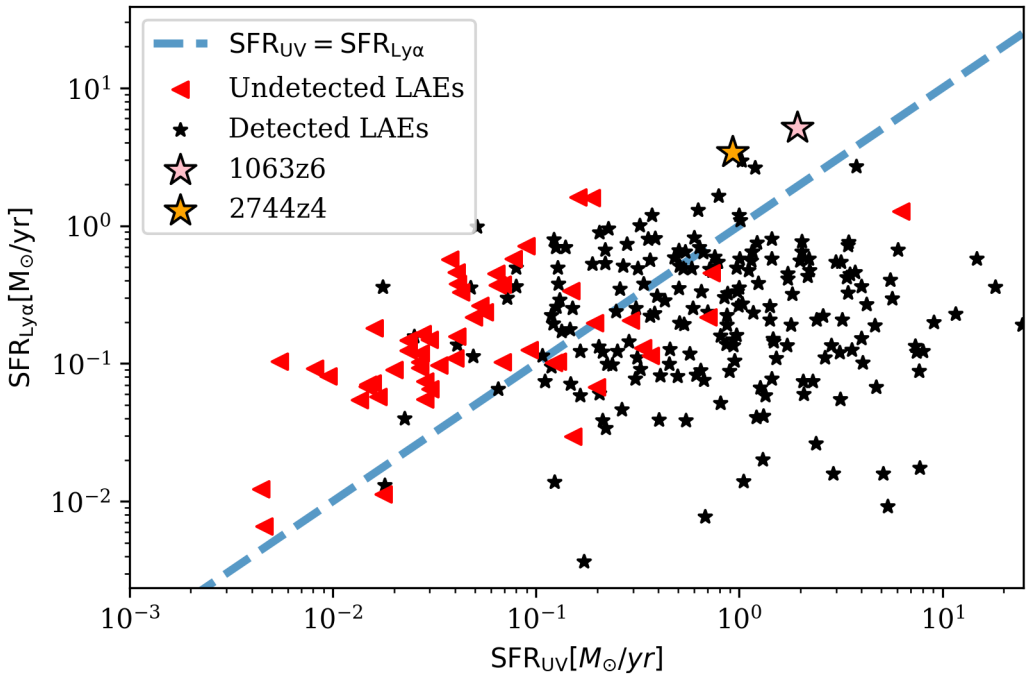

FIGURE 6.1 – Lensed MUSE-detected LAEs shown in the SFR$_{Ly\alpha}$ SFR$_{UV}$ plane. The line of equal SFR is shown in blue, continuum-detected LAEs in black and upper limits on continuum-undetected LAEs in red. 1063z6 is shown by the pink star and 2744z4 by the orange star.

In Fig. 6.2 I show the contours of Lyman-α emission superimposed on UV emission for 1063z6 and 2744z4. Already here, we can see compact UV emission and an extended Lyman-α halo around both galaxies. If the dust were to strongly attenuate the compact stellar emission, and allow the Lyman-α to escape through clear channels and an extended distribution of hydrogen, we could expect a picture like this.

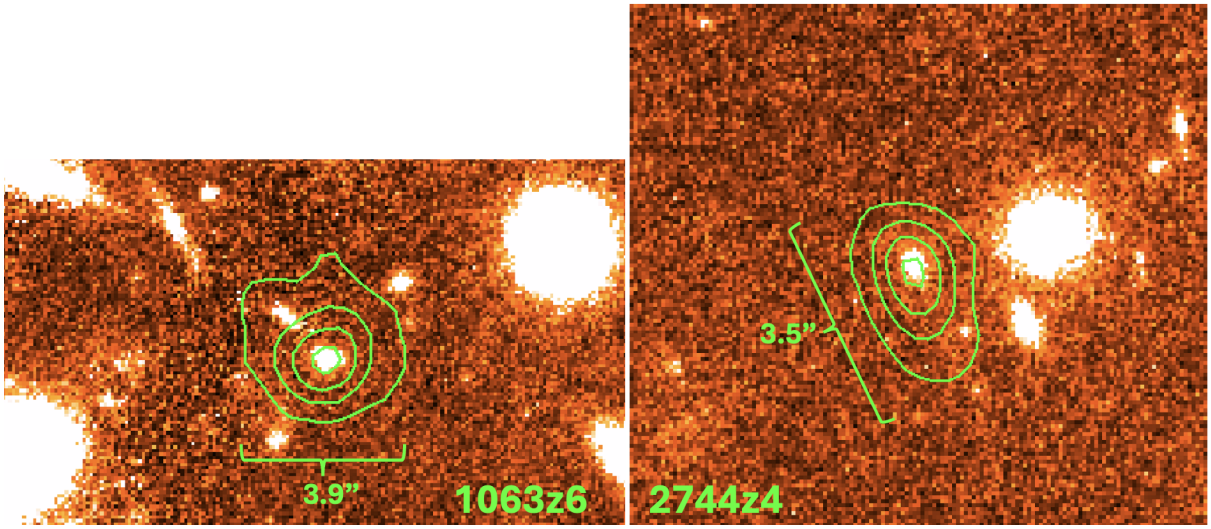

FIGURE 6.2 – Continuum-subtracted contours of Lyman-α emission detected by MUSE superimposed on UV (stellar) emission. The spatial extent of the Lyman-α emission is noted in green. *Left :* 1063-z6 - F814W HST filter. *Right :* 2744-z4 - F606W HST filter.

Unfortunately, the peaks of the dust continua of 1063z6 and 2744z4 would still take > 1 day to observe with ALMA. These observations are therefore too expensive, especially if one looks to build a sample size adequate to draw conclusions about this population of HST-dark LAEs.
There are other options. Another way to estimate the dust attenuation in a galaxy is the Balmer decrement, mentioned already as an important next step for the MUSE LAEs. Galaxies like 1063z6 and 2744z4, and potentially even fainter galaxies, could be observed with the NIRSpec IFU, giving access not only to the Hα and Hβ emission lines, but also to OIII and the spatial distribution of each of these lines. This, like ALMA observations, would not lead to a large sample size, but instead, with a very detailed study, would give insight into the physical conditions in the galaxies that give rise to Lyman-α photons escaping better than UV photons and creating $\mathrm{SFR_{Ly\alpha}} > \mathrm{SFR_{UV}}$.
However this would not let us directly map the dust. Another potential avenue would be photometric observations at longer wavelength, such as with JWST/MIRI (5 to 28 microns). Deep MIRI observations, combined with deep observations in many other bands from NIRCam and HST, would enable very reliable SED fitting which would be able to distinguish many dust-absorption scenarios (see Fig. 6.3). The peak of the dust emission would not be observed at redshifts towards reionisation, but dust emission bluewards of the peak could be mapped, especially at $z \sim 2 - 3$.
1063z6 and 2744z4, for example, already have excellent photometric coverage from HST and JWST/NIRCam and the A2744 lensing cluster will benefit from MIRI observations in Cycle 3 (ID : 5578, PI : E. Iani). A range of deep observations like this allows us to map Lyman-α (MUSE), UV (HST), optical (JWST/NIRCam) and NIR (JWST/MIRI) emission for MUSE LAEs. These emissions trace hydrogen, young stars, old stars, and dust respectively, so covering each one for the same objects would offer a unique window into

the properties of mid-to-high redshift galaxies. The regions allowing Lyman-α emission to escape could be mapped in relation to the stars forming in the galaxy and the areas of high dust attenuation. Pushing this kind of coverage for large samples of galaxies from the local universe, through $z \sim 1-2$ (see, for example, Shivaei et al. 2024), all the way to the EoR is essential to understand the evolution of galaxy properties, culminating in the galaxies responsible for reionisation.

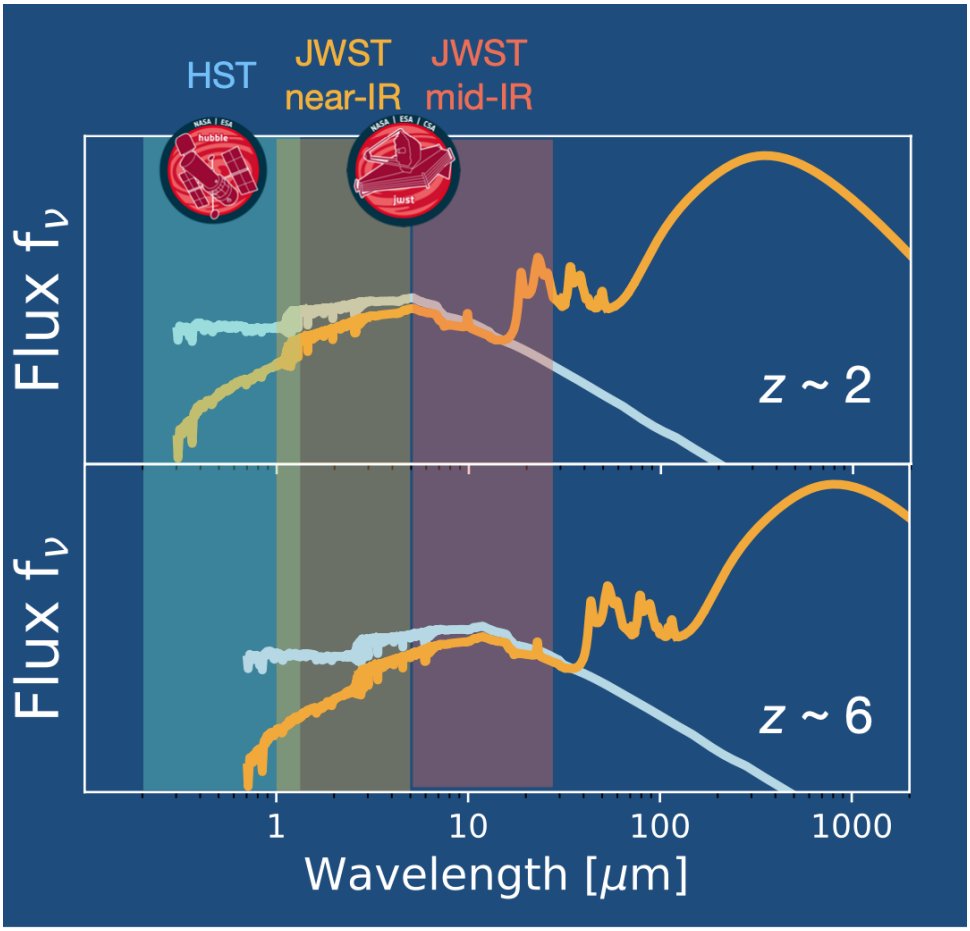

FIGURE 6.3 – A graphic showing the coverage of HST, JWST/NIRCam and JWST/MIRI on two galaxy SEDs, one heavily dust-attenuated (yellow) and one without significant dust attenuation (blue). Credit : I. Shivaei, Hubble and Webb VII conference.

In summary, NIRSpec IFU and MIRI observations are two possible directions towards better understanding UV-dark LAEs and more generally, LAEs that exhibit $\mathrm{SFR}_{\mathrm{Ly}\alpha} > \mathrm{SFR}_{\mathrm{UV}}$. As mentioned these observations would come with a huge range of other science goals and interests for galaxy evolution. In the following section, I give more details of an upcoming project pertinent to mapping these different emission areas of galaxies, starting with UV and Lyman-α.

6.2.2 CLASS and UV-morphology of LAEs

There remains much detail to be understood in the landscape of LAEs and their relation to the UV emission of the host galaxy. Fig. 6.2 showcases two examples of compact UV emission surrounded by an extended Lyman-α halo, but we also see instances where the Lyman-α emission is not centred on the UV emission (e.g. Shibuya et al. 2014; Hoag et al. 2019; Lemaux et al. 2021; Claeyssens et al. 2022). We understand that the hydrogen in a galaxy can be spatially decoupled from the stellar population, creating these effects, but more complicated scenarios remain mysterious, for example, the HST-dark LAEs. The precise effects of viewing angle, dust content and distribution and outflows/inflows can create very particular cases, where there remains progress to be made in connecting the Lyman-α emission with the properties of the host galaxy.

There are a host of simulations treating the expected observed Lyman-α properties based on the aforementioned effects (Verhamme et al. 2008; Verhamme et al. 2012; Rosdahl &Blaizot 2012; Mitchell et al. 2021; Smith et al. 2022; Blaizot et al. 2023). Being able to compare a large sample of LAEs with the results from these simulations will make it possible to connect the internal physics treated by the simulations with the observed Lyman-α line shape and make conclusions about the LAE population. Assessing a high number of individual scenarios will give greater detail in terms of Lyman-α properties and their connection to the host galaxy, as more of the simulated behaviours will be observed (with good statistics, not just a few galaxies).

The Characterizing Lyman-Alpha emitters with Snapshot Survey (CLASS) project (PI : R. Dutta) is a snapshot program which aims to obtain HST imaging (F160W filter) for 100 archival MUSE fields, with the goal of connecting MUSE-detected LAEs with their continuum counterparts and assessing the properties of the continuum. While the study comprises only one filter [4], the number of LAEs that will be observed (~ 1000 at $z \sim 3.5$) makes this an excellent opportunity to study the connection between UV morphology and the morphology and line-shape of Lyman-α emission. The statistical power this number of LAEs will achieve means conclusions about population properties are possible, as well as in-depth study of particular systems. An additional advantage is that, at this redshift, the emerging Lyman-α line will not be affected by IGM attenuation, so we can expect to observe the full range of Lyman-α profiles (see Sect. 1.4 and Blaizot et al. 2023).

My goal as part of this effort will be to connect the UV morphology of the galaxies with their Lyman-α emission, including emission centroids and offsets, extents and connections to Lyman-α line shape. I will also investigate the presence and reasons for non-detections of the LAEs that do not appear in the F160W images. I will study the Lyman-α line-shape of these galaxies and the effects of MUSE depth on their appearance. This last point will be made possible with CLASS' homogeneous photometry over a huge number of LAEs with different MUSE depths. Future surveys combining MUSE (or any IFU) data and photometry can benefit from estimates of how many LAEs will be undetected in the continuum based on spectroscopic and photometric depth.

In fields with ancillary data, such as the MUSE Extremely and Ultra Deep Fields, it will also be possible to study the stellar mass function (SMF) of the LAEs. Accurate stellar masses require as many photometric bands as possible, covering the rest-frame

4. Note that many of the archival fields involved have existing HST and JWST data

optical emission of the galaxy, and where this is available, the LAE SMF can be derived (see e.g. Santos et al. 2020b). This function gives insight into what kinds of galaxies (by stellar mass) exhibit Lyman-α emission. One can investigate the relative evolution of the SMF for brighter and fainter LAEs as well as how stellar mass evolves with other galaxy properties such as the morphological parameters mentioned above.
Is it challenging to perform this type of analysis on large sample of spectroscopically detected LAEs, and only made possible through a parallel survey of a large number of archival MUSE fields, some of which contain many LAEs in their own right, combined with deep photometry in many bands. As such, the CLASS programme has the ability to cover a large range of Lyman-α luminosities and stellar masses, as well as morphological types, at $z \sim 3$, with good statistics. Large-scale programmes such as this are necessary to understand population-wide trends, rather than the peculiar properties of individual galaxies.

6.3 Further in the future...

I devote a small section of this chapter to an overview of future instruments, for which high-redshift galaxy evolution is a key goal, and which I anticipate having a significant impact on the field [5].

– **ELT/MOSAIC :** the Extremely Large Telescope (ELT) is currently under construction in Cerro Armazones, Chile, scheduled for first light towards the end of the decade. All of its instruments will see applications in high-redshift galaxy evolution, but MOSAIC especially will have a big impact. MOSAIC is a multi-object spectrograph with 200 fibres and 8 mini IFUs. It will observe in low and high spectral resolution modes (R $\sim 5,000$ and R $\sim 20,000$) between 0.39 and 1.8 μm. Designed with high survey speed and multiplex in mind, it will serve as a highly efficient follow-up machine for low-surface brightness sources, such as high-redshift galaxies. Notably, even the low-resolution mode will be higher than the highest-resolution NIRSpec mode, allowing the Lyman-α line shape to be studied in greater detail. In low-resolution NIRSpec spectra, occasionally the Lyman-α line can even be missed altogether (Bunker et al. 2023).
MOSAIC will be capable of detected the Lyman-α line in the redshift range $2.7 < z < 13.8$; from just before Cosmic Noon to just after Cosmic Dawn. This will enable the community to track galaxy properties related to Lyman-α emission, as well as other important UV lines such as high-ionisation carbon, nitrogen, silicon lines, and HeII, across a vast range of redshifts. This range spans from the earliest populations observed so far to the fully developed galaxy zoo, capturing significant changes in galaxy properties over time. MOSAIC will perform particularly strongly when it comes to follow-up exercises, with 200 objects observable at once in the fibres, and more in the IFUs which can observe simultaneously. This last ability will prove crucial for observing extended objects, such as lensing arcs, protoclusters, and complicated systems such as GN-z11 (Bunker et al. 2023), LAP1 (Vanzella et al. 2023) or high-redshift mergers. In just five hours of exposure, thanks to the 39m mirror of the ELT, MOSAIC will be able to detect the continuum of

5. This is by no means an exhaustive list, merely a list of those which will have the greatest impact on my areas of interest and those I have encountered in the context of my thesis work.

sources down to 27 magnitudes. This is completely beyond the capabilities of the premier telescopes available today. For a pertinent example related to this thesis, I mention that when observing LAEs with VLT/MUSE, the continuum is almost never detected, even for the bright objects.

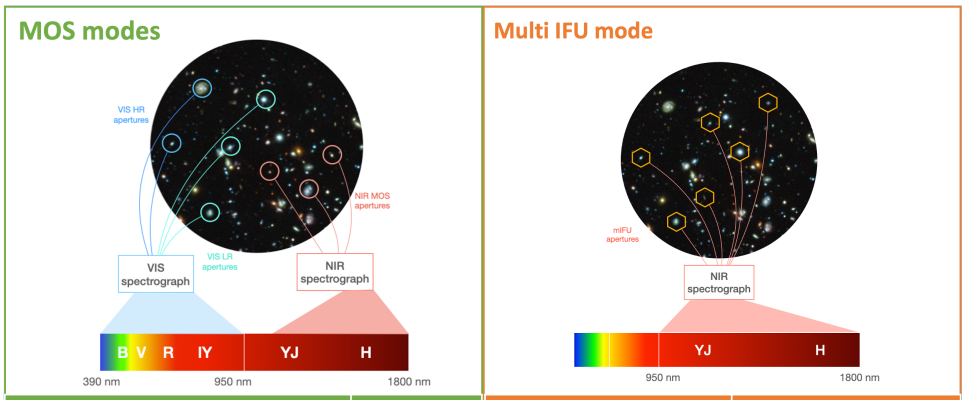

MOS mode	Multiplex
Visible Low resolution (R=4 000)	140
Visible High resolution (R=19 000)	85
NIR Low and High resolution	180

mIFU properties	Values
Multiplex	8
Field of view	2.2 arcsec (hexagonal)
Spaxel	150 mas

FIGURE 6.4 – A graphic of the properties of the MOSAIC instrument's MOS and IFU modes. Credit : MOSAIC Consortium (http://www.mosaic-elt.eu/).

MOSAIC will therefore be able to deliver huge amounts of UV, and at lower redshifts also optical, information for many galaxies at a time, making it an ideal follow-up option for the huge numbers of high-redshift galaxies detected by JWST/NIRCam and in the coming years also the Euclid space telescope.

– **VLT/MOONS :** the third generation VLT instrument, MOONS (Multi-Object Optical and Near-infrared Spectrograph) (Cirasuolo et al. 2014) can bridge the gap between the present day and the arrival of MOSAIC, with the GTO starting in 2025. It is also a fibre spectrograph intended largely for follow-up science, observing between 0.65 and 1.75 μm with moderate spectral resolution ($R \sim 4000 - 6600$) and 0.76 and 1.64 μm with high spectral resolution ($R \sim 4000 - 18000$). As MOONS will be installed on the VLT, with its 8m mirror, it will not be capable of the same sensitivity as MOSAIC, and it will not be possible to position the fibres closer to each other than 10″. However, its spectral coverage and resolution makes it a leap forward from MUSE in terms of detecting LAEs into the EoR as well as studying the Lyman-α line shape. MOONS' follow up and fast survey capabilities will play an important role in garnering the maximum benefit from large scale surveys such as Euclid Wide and Deep (Scaramella et al. 2022; Euclid Collaboration et al. 2024), and those carried out by the Large Synoptic Survey Telescope (LSST) (Ivezić et al. 2019) and the future Nancy Grace Roman Space Telescope (Spergel et al. 2015).

– **SKA :** the Square Kilometer Array is two radio telescopes, currently under construction, in Australia and South Africa. SKA-Low, in Australia, will observe between 50 and 350 MHz (85-600 cm) with 512 stations of 256 antennas, giving an effective collecting area of 419,000 m^2. SKA-Mid, in South Africa, will observe from 350 MHz to 15.4 GHz (1.9-85 cm) with a total collecting area of 33,000 m^2. Both arrays represent a large increase in sensitivity compared to current radio telescopes due to their huge collecting area. SKA-Low in particular is aimed at 21cm science. This area of research uses the 21cm (rest frame) emission line to map neutral hydrogen. This emission lines originates from a hyperfine transition (spin-flip transition) in neutral hydrogen, which can be observed up to the limit of the Universe's neutral state (380,000 years after the Big Bang, see Sect. 1.1). This makes it possible to describe the conditions of the Universe before any starlight was emitted (or could propagate in the neutral hydrogen). Therefore we can probe the state of the Universe before the first stars and galaxies. SKA-Low aims to directly quantify the emergence of the ionised bubbles in the IGM at Cosmic Dawn. In particular, tomographic imaging [6] will allow the SKA to provide size measurements of these growing ionised bubbles (Giri et al. 2018). Science with SKA will directly complement and serve as a cross-check for the effort to investigate Cosmic Dawn with galaxy observations from JWST. SKA will also be able to trace emissions from hydrogen until after the EoR, $z < 6$, in order to characterise the evolution of the IGM throughout this period.

6.4 Conclusions

This thesis has taken place in an extraordinary time for the field of galaxy evolution, with early results from the JWST rapidly changing our understanding of the landscape of high-redshift galaxies. The work has taken advantage of deep photometry and spectroscopy of lensing fields from three different observatories in order to create the largest lensed sample of LAEs and LBGs for the purpose of elucidating their properties and assessing their impact on cosmic reionisation.

The work has highlighted the potential of combining VLT/MUSE, HST and JWST observations to make detailed studies of galaxy evolution from redshifts near cosmic noon to the epoch of reionisation. I have studied the properties of intrinsically faint LAEs compared to UV-selected galaxies and assessed their contribution to reionisation in several ways. As the number of lensing clusters with adequate depth (both spectroscopic and photometric depth) remains relatively low, expanding the datasets with which we conduct this type of analysis is a central goal for astronomy in the coming years. This is exemplified by the emphasis placed on lensing cluster observations in current and recent JWST and VLT/MUSE observing cycles.

These observations are useful both for accessing low-mass regimes at redshifts between cosmic noon and reionisation and for studying the highest-redshift galaxies, which may be intrinsically bright, but appear faint due to distance. In the near future I will work on data which allows both of these regimes to be accessed, with the goal in both to be further

6. Tomography uses 2D slices to build up a 3D picture. For SKA-Low this will be in the form of a lightcone formed by slices at different observing frequencies, corresponding to different redshifts.

characterisation of the contributors to reionisation. These projects will continue to seek the maximum exploitation of HST, JWST and MUSE data, be it through the CLASS project using HST and MUSE to investigate 1000s of LAEs, the GLIMPSE programme, aimed at imaging the faintest galaxies possible towards and into the EoR, the effort on the A1689 lensing cluster which will unveil faint populations between $1.5 < z < 5$ or future proposals for observing time with JWST instruments.

Outstanding problems which arose during the thesis include the nature of UV-dark LAEs. I have given a number of routes towards better characterisation of these galaxies and hope to pursue them in the near future. Understanding this population is crucial to several areas of astrophysics, including but not limited to an appreciation of what type of galaxies are missed in UV-selected samples, the nature of Lyman-α emission from galaxies and the interplay of stellar, Lyman-α and dust emission.

Further data from JWST instruments, primarily NIRSpec and MIRI, would also illuminate several outstanding issues, such as helping to constrain dust attenuation from these faint galaxies and therewith accurate Lyman-α escape fractions. The correlation of Lyman-α emission can also be correlated with other parameters at high redshift such as metallicity and ionisation state in order to better elucidate the properties of Lyman-α emitters and reionisation-era galaxies in general.

Multi-wavelength observations, even as far redwards as the wavelengths of ALMA, contingent upon adequate signal-to-noise, can go great lengths in connecting Lyman-α emission to different morphological parameters. Future projects in the near and mid-term count this as a key science goal. In the coming years, across all fields of astrophysics, it will be important to fully explore the synergy of HST, JWST, ground-based data such as VLT/MUSE and ALMA, not only to bring the stunning early results from the JWST to full maturity but also to prepare for the next generation of telescopes, such as the Extremely Large Telescope, currently undergoing construction in Chile. The science of LAEs and reionisation-era galaxies stands to benefit greatly from these efforts and will likely remain an important and active field of research for the foreseeable future.

Bibliography

Acebron, A., Cibirka, N., Zitrin, A., et al. 2018, Astrophysical Journal, 858, 42

Acebron, A., Jullo, E., Limousin, M., et al. 2017, Monthly Notices of the RAS, 470, 1809

Adams, N., Conselice, C., Ferreira, L., et al. 2023, Monthly Notices of the Royal Astronomical Society, 518, 4755

Adams, N. J., Conselice, C. J., Austin, D., et al. 2024, Astrophysical Journal, 965, 169

Alam, S., Albareti, F. D., Prieto, C. A., et al. 2015, The Astrophysical Journal Supplement Series, 219, 12

Ando, M., Ohta, K., Iwata, I., et al. 2006, The Astrophysical Journal, 645, L9

Arrabal Haro, P., Dickinson, M., Finkelstein, S. L., et al. 2023a, Astrophysical Journal, Letters, 951, L22

Arrabal Haro, P., Dickinson, M., Finkelstein, S. L., et al. 2023b, Nature, 622, 707

Arrabal Haro, P., Rodríguez Espinosa, J., Muñoz-Tuñón, C., et al. 2018, Monthly Notices of the Royal Astronomical Society, 478, 3740

Assef, R. J., Frank, S., Grier, C. J., et al. 2012, Astrophysical Journal, Letters, 753, L2

Atek, H., Kunth, D., Hayes, M., Östlin, G., & Mas-Hesse, J. M. 2008, Astronomy and Astrophysics, 488, 491

Atek, H., Labbé, I., Furtak, L. J., et al. 2024, Nature, 626, 975

Atek, H., Labbé, I., Furtak, L. J., et al. 2023 [Arxiv :2308.08540v1]

Atek, H., Shuntov, M., Furtak, L. J., et al. 2023, Monthly Notices of the RAS, 519, 1201

Austin, D., Conselice, C. J., Adams, N. J., et al. 2024, arXiv e-prints, arXiv :2404.10751

Bacon, R., Accardo, M., Adjali, L., et al. 2010, in Society of Photo-Optical Instrumentation Engineers (SPIE) Conference Series, Vol. 7735, Ground-based and Airborne Instrumentation for Astronomy III, ed. I. S. McLean, S. K. Ramsay, & H. Takami, 773508

Bacon, R., Brinchmann, J., Conseil, S., et al. 2023, Astronomy and Astrophysics, 670, A4

Bacon, R., Brinchmann, J., Richard, J., et al. 2015, Astronomy and Astrophysics, 575, A75

Beauchesne, B., Clément, B., Hibon, P., et al. 2024, Monthly Notices of the RAS, 527, 3246

Begley, R., Cullen, F., McLure, R., et al. 2024, Monthly Notices of the Royal Astronomical Society, 527, 4040

Berg, D. A., James, B. L., King, T., et al. 2022, Astrophysical Journal, Supplement, 261, 31

Bertin, E. & Arnouts, S. 1996, Astronomy and astrophysics supplement series, 117, 393

Bezanson, R., Labbe, I., Whitaker, K. E., et al. 2022, arXiv e-prints, arXiv :2212.04026

Blain, A. W. & Phillips, T. G. 2002, Monthly Notices of the RAS, 333, 222

Blaizot, J., Garel, T., Verhamme, A., et al. 2023, Monthly Notices of the RAS, 523, 3749

Blanc, G. A., Adams, J. J., Gebhardt, K., et al. 2011, The Astrophysical Journal, 736, 31

Bolzonella, M., Kovač, K., Pozzetti, L., et al. 2010, Astronomy and Astrophysics, 524, A76

Bolzonella, M., Miralles, J.-M., & Pelló, R. 2000, Arxiv preprint astro-ph/0003380

Boogaard, L. A., Brinchmann, J., Bouché, N., et al. 2018, Astronomy & Astrophysics, 619, A27

Boquien, M., Burgarella, D., Roehlly, Y., et al. 2019, Astronomy & Astrophysics, 622, A103

Bosman, S. E. I., Davies, F. B., Becker, G. D., et al. 2022, Monthly Notices of the RAS, 514, 55

Bouwens, R., González-López, J., Aravena, M., et al. 2020, The Astrophysical Journal, 902, 112

Bouwens, R., Illingworth, G., Ellis, R., Oesch, P., & Stefanon, M. 2022, The Astrophysical Journal, 940, 55

Bouwens, R., Oesch, P., Stefanon, M., et al. 2021, The Astronomical Journal, 162, 47

Bouwens, R. J., Aravena, M., Decarli, R., et al. 2016, The Astrophysical Journal, 833, 72

Bouwens, R. J., Illingworth, G., Oesch, P., et al. 2015a, The Astrophysical Journal, 803, 34

Bouwens, R. J., Illingworth, G. D., Franx, M., et al. 2009, Astrophysical Journal, 705, 936

Bouwens, R. J., Illingworth, G. D., Oesch, P. A., et al. 2015b, The Astrophysical Journal, 811, 140

Bouwens, R. J., Illingworth, G. D., Oesch, P. A., et al. 2010, Astrophysical Journal, Letters, 709, L133

Bouwens, R. J., Illingworth, G. D., van Dokkum, P. G., et al. 2022a, Astrophysical Journal, 927, 81

Bouwens, R. J., Smit, R., Schouws, S., et al. 2022b, Astrophysical Journal, 931, 160

Brammer, G. B., Marchesini, D., Labbé, I., et al. 2016, The Astrophysical Journal Supplement Series, 226, 6

Brinchmann, J. 2023, Monthly Notices of the Royal Astronomical Society, stad1704

Brinchmann, J., Charlot, S., White, S. D., et al. 2004, Monthly notices of the royal astronomical society, 351, 1151

Brocklehurst, M. 1971, Monthly Notices of the RAS, 153, 471

Bruzual, G. & Charlot, S. 2003, Monthly Notices of the Royal Astronomical Society, 344, 1000

Buat, V., Heinis, S., Boquien, M., et al. 2014, Astronomy & Astrophysics, 561, A39

Buat, V., Noll, S., Burgarella, D., et al. 2012, Astronomy & Astrophysics, 545, A141

Bunker, A. J., Saxena, A., Cameron, A. J., et al. 2023, arXiv preprint arXiv :2302.07256

Calura, F., Pozzi, F., Cresci, G., et al. 2017, Monthly Notices of the RAS, 465, 54

Calzetti, D., Armus, L., Bohlin, R. C., et al. 2000, The Astrophysical Journal, 533, 682

Cameron, A. J., Katz, H., Witten, C., et al. 2023, arXiv e-prints, arXiv :2311.02051

Carniani, S., Hainline, K., D'Eugenio, F., et al. 2024 [Arxiv :2405.18485v1]

Caruana, J., Bunker, A. J., Wilkins, S. M., et al. 2014, Monthly Notices of the Royal Astronomical Society, 443, 2831

Caruana, J., Wisotzki, L., Herenz, E. C., et al. 2018, Monthly Notices of the Royal Astronomical Society, 473, 30

Casey, C. M. 2012, Monthly Notices of the Royal Astronomical Society, 425, 3094

Casey, C. M., Narayanan, D., & Cooray, A. 2014, Physics Reports, 541, 45

Cassata, P., Le Fèvre, O., Garilli, B., et al. 2011, Astronomy and Astrophysics, 525, A143

Cassata, P., Tasca, L., Le Fèvre, O., et al. 2015, Astronomy & Astrophysics, 573, A24

Castellano, M., Fontana, A., Grazian, A., et al. 2012, Astronomy & Astrophysics, 540, A39

Chabrier, G. 2003, Publications of the Astronomical Society of the Pacific, 115, 763

Chemerynska, I., Atek, H., Furtak, L. J., et al. 2023, arXiv e-prints, arXiv :2312.05030

Chen, Y.-M., Tremonti, C. A., Heckman, T. M., et al. 2010, The Astronomical Journal, 140, 445

Chen, Z., Stark, D. P., Mason, C., et al. 2023 [Arxiv :2311.13683v1]

Choustikov, N., Katz, H., Saxena, A., et al. 2024a [Arxiv :2401.09557v1]

Choustikov, N., Stiskalek, R., Saxena, A., et al. 2024b [Arxiv :2405.09720v1]

Ciardullo, R., Zeimann, G. R., Gronwall, C., et al. 2014, The Astrophysical Journal, 796, 64

Ciesla, L., Elbaz, D., & Fensch, J. 2017, Astronomy & Astrophysics, 608, A41

Ciesla, L., Elbaz, D., Ilbert, O., et al. 2023, arXiv e-prints, arXiv :2309.15720

Cirasuolo, M., Afonso, J., Carollo, M., et al. 2014, in Ground-based and airborne instrumentation for astronomy V, Vol. 9147, SPIE, 202–214

Claeyssens, A., Adamo, A., Richard, J., et al. 2023, Monthly Notices of the RAS, 520, 2180

Claeyssens, A., Richard, J., Blaizot, J., et al. 2022, Astronomy and Astrophysics, 666, A78

Coleman, G., Wu, C.-C., & Weedman, D. 1980, Astrophysical Journal Supplement Series, vol. 43, July 1980, p. 393-416. Research sponsored by the Koninklijke Nederlandse Akademie van Wetenschappen ;, 43, 393

Cowie, L. L., Barger, A. J., & Hu, E. M. 2010, The Astrophysical Journal, 711, 928

Curti, M., d'Eugenio, F., Carniani, S., et al. 2023, Monthly Notices of the Royal Astronomical Society, 518, 425

Curtis-Lake, E., Carniani, S., Cameron, A., et al. 2023, Nature Astronomy, 7, 622

Curtis-Lake, E., McLure, R., Pearce, H., et al. 2012, Monthly Notices of the Royal Astronomical Society, 422, 1425

Daddi, E., Dickinson, M., Morrison, G., et al. 2007, The Astrophysical Journal, 670, 156

Dayal, P. & Ferrara, A. 2018, Physics Reports, 780, 1

Dayal, P., Ferrara, A., & Saro, A. 2010, Monthly Notices of the RAS, 402, 1449

Dayal, P., Ferrara, A., Sommovigo, L., et al. 2022, Monthly Notices of the RAS, 512, 989

Dayal, P., Maselli, A., & Ferrara, A. 2011, Monthly Notices of the Royal Astronomical Society, 410, 830

Dayal, P., Volonteri, M., Greene, J. E., et al. 2024 [Arxiv :2401.11242v1]

De Barros, S., Pentericci, L., Vanzella, E., et al. 2017, Astronomy & Astrophysics, 608, A123

de La Vieuville, G., Bina, D., Pello, R., et al. 2019, Astronomy & Astrophysics, 628, A3

de La Vieuville, G., Pelló, R., Richard, J., et al. 2020, Astronomy & Astrophysics, 644, A39

Dekel, A., Sarkar, K. C., Birnboim, Y., Mandelker, N., & Li, Z. 2023, Monthly Notices of the RAS, 523, 3201

Dey, A., Spinrad, H., Stern, D., Graham, J. R., & Chaffee, F. H. 1998, The Astrophysical Journal, 498, L93

Dijkstra, M. 2014, Publications of the Astronomical Society of Australia, 31, e040

Dijkstra, M. 2016, Understanding the Epoch of Cosmic Reionization : Challenges and Progress, 145

Dijkstra, M. & Kramer, R. 2012, Monthly Notices of the RAS, 424, 1672

Donevski, D., Lapi, A., Małek, K., et al. 2020, Astronomy and Astrophysics, 644, A144

Donnan, C., McLure, R., Dunlop, J., et al. 2024, arXiv preprint arXiv :2403.03171

Donnan, C. T., McLeod, D. J., Dunlop, J. S., et al. 2023, Monthly Notices of the RAS, 518, 6011

Drake, A.-B., Garel, T., Wisotzki, L., et al. 2017, Astronomy & Astrophysics, 608, A6

Dressler, A., Henry, A., Martin, C. L., et al. 2015, Astrophysical Journal, 806, 19

Duncan, K. & Conselice, C. J. 2015, Monthly Notices of the Royal Astronomical Society, 451, 2030

Duncan, K., Conselice, C. J., Mortlock, A., et al. 2014, Monthly Notices of the Royal Astronomical Society, 444, 2960

Eisenstein, D. J., Willott, C., Alberts, S., et al. 2023, arXiv e-prints, arXiv :2306.02465

Elbaz, D., Daddi, E., Le Borgne, D., et al. 2007, Astronomy & Astrophysics, 468, 33

Elbaz, D., Dickinson, M., Hwang, H., et al. 2011, Astronomy & Astrophysics, 533, A119

Endsley, R., Stark, D. P., Bouwens, R. J., et al. 2022, Monthly Notices of the RAS, 517, 5642

Euclid Collaboration, Mellier, Y., Abdurro'uf, & Acevedo Barroso. 2024, arXiv e-prints, arXiv :2405.13491

Feltre, A., Charlot, S., & Gutkin, J. 2016, Monthly Notices of the RAS, 456, 3354

Ferland, G. J., Chatzikos, M., Guzmán, F., et al. 2017, Revista Mexicana de Astronomia y Astrofisica, 53, 385

Ferrara, A. 2023, arXiv e-prints, arXiv :2310.12197

Ferrara, A., Pallottini, A., & Dayal, P. 2023, Monthly Notices of the RAS, 522, 3986

Finkelstein, S. L., Bagley, M. B., Arrabal Haro, P., et al. 2022, Astrophysical Journal, Letters, 940, L55

Finkelstein, S. L., Bagley, M. B., Ferguson, H. C., et al. 2023, Astrophysical Journal, Letters, 946, L13

Finkelstein, S. L., Malhotra, S., Rhoads, J. E., Hathi, N. P., & Pirzkal, N. 2009, Monthly Notices of the Royal Astronomical Society, 393, 1174

Finkelstein, S. L., Ryan, R. E., Papovich, C., et al. 2015, The Astrophysical Journal, 810, 71

Flury, S. R., Jaskot, A. E., Ferguson, H. C., et al. 2022, Astrophysical Journal, Supplement, 260, 1

Foreman-Mackey, D., Hogg, D. W., Lang, D., & Goodman, J. 2013, Publications of the Astronomical Society of the Pacific, 125, 306

Fujimoto, S., Finkelstein, S. L., Burgarella, D., et al. 2023, Astrophysical Journal, 955, 130

Fuller, S., Lemaux, B., Bradač, M., et al. 2020, The Astrophysical Journal, 896, 156

Furtak, L. J., Atek, H., Lehnert, M. D., Chevallard, J., & Charlot, S. 2021, Monthly Notices of the RAS, 501, 1568

Garel, T., Blaizot, J., Rosdahl, J., et al. 2021, Monthly Notices of the RAS, 504, 1902

Garn, T. & Best, P. N. 2010, Monthly Notices of the Royal Astronomical Society, 409, 421

Gaskell, C. M. 2009, New Astronomy Reviews, 53, 140

Giovinazzo, E., Trebitsch, M., Mauerhofer, V., Dayal, P., & Oesch, P. A. 2024 [Arxiv :2402.17635v1]

Giri, S. K., Mellema, G., Dixon, K. L., & Iliev, I. T. 2018, Monthly Notices of the RAS, 473, 2949

Goovaerts, I., Pello, R., Burgarella, D., et al. 2024, Astronomy and Astrophysics, 683, A184

Goovaerts, I., Pello, R., Thai, T., et al. 2023, Astronomy & Astrophysics, 678, A174

Grazian, A., Giallongo, E., Boutsia, K., et al. 2022, The Astrophysical Journal, 924, 62

Grazian, A., Giallongo, E., Boutsia, K., et al. 2018, Astronomy & Astrophysics, 613, A44

Gronke, M., Bull, P., & Dijkstra, M. 2015, Astrophysical Journal, 812, 123

Gronke, M. & Dijkstra, M. 2016, The Astrophysical Journal, 826, 14

Gronke, M., Ocvirk, P., Mason, C., et al. 2021, Monthly Notices of the Royal Astronomical Society, 508, 3697

Hansen, M. & Oh, S. P. 2006, Monthly Notices of the Royal Astronomical Society, 367, 979

Harikane, Y., Nakajima, K., Ouchi, M., et al. 2024, Astrophysical Journal, 960, 56

Harikane, Y., Ouchi, M., Oguri, M., et al. 2023a, Astrophysical Journal, Supplement, 265, 5

Harikane, Y., Zhang, Y., Nakajima, K., et al. 2023b, Astrophysical Journal, 959, 39

Hartwig, T., Yoshida, N., Magg, M., et al. 2018, Monthly Notices of the RAS, 478, 1795

Hashimoto, T., Garel, T., Guiderdoni, B., et al. 2017, Astronomy and Astrophysics, 608, A10

Hashimoto, T., Verhamme, A., Ouchi, M., et al. 2015, The Astrophysical Journal, 812, 157

Hayes, M. 2015, Publications of the Astronomical Society of Australia, 32, e027

Hayes, M., Östlin, G., Duval, F., et al. 2014, The Astrophysical Journal, 782, 6

Hayes, M., Östlin, G., Schaerer, D., et al. 2010, Nature, 464, 562

Hayes, M., Östlin, G., Schaerer, D., et al. 2013, The Astrophysical Journal Letters, 765, L27

Hayes, M., Schaerer, D., Östlin, G., et al. 2011, The Astrophysical Journal, 730, 8

Hayes, M. J., Runnholm, A., Scarlata, C., Gronke, M., & Rivera-Thorsen, T. E. 2023, Monthly Notices of the RAS, 520, 5903

Hayes, M. J. & Scarlata, C. 2023, Astrophysical Journal, Letters, 954, L14

Herenz, E. C., Wisotzki, L., Saust, R., et al. 2019, Astronomy & Astrophysics, 621, A107

Hoag, A., Treu, T., Pentericci, L., et al. 2019, Monthly Notices of the Royal Astronomical Society, 488, 706

Hu, W., Martin, C. L., Gronke, M., et al. 2023, Astrophysical Journal, 956, 39

Iani, E., Caputi, K. I., Rinaldi, P., et al. 2023 [Arxiv :2309.08515v1]

Ivezić, Ž., Kahn, S. M., Tyson, J. A., et al. 2019, Astrophysical Journal, 873, 111

Izotov, Y. I., Schaerer, D., Worseck, G., et al. 2020, Monthly Notices of the RAS, 491, 468

Izotov, Y. I., Thuan, T. X., Guseva, N. G., et al. 2024, Monthly Notices of the RAS, 527, 281

Jaskot, A. E., Silveyra, A. C., Plantinga, A., et al. 2024 [Arxiv :2406.10171v1]

Jiang, H., Wang, X., Cheng, C., et al. 2023, arXiv e-prints, arXiv :2312.04151

Jiang, L., Egami, E., Fan, X., et al. 2013, Astrophysical Journal, 773, 153

Jiang, L., Ning, Y., Fan, X., et al. 2022, Nature Astronomy, 6, 850

Jullo, E. & Kneib, J.-P. 2009, Monthly Notices of the Royal Astronomical Society, 395, 1319

Jullo, E., Kneib, J.-P., Limousin, M., et al. 2007, New Journal of Physics, 9, 447

Jung, I., Ferguson, H. C., Hayes, M. J., et al. 2024 [Arxiv :2403.02388v1]

Kannan, R., Garaldi, E., Smith, A., et al. 2022, Monthly Notices of the RAS, 511, 4005

Karman, W., Caputi, K., Caminha, G., et al. 2017, Astronomy & Astrophysics, 599, A28

Kennicutt, R. C. 1998a, The astrophysical journal, 498, 541

Kennicutt, R. C. 1998b, Annual Review of Astronomy and Astrophysics, 36, 189

Kerutt, J., Oesch, P. A., Wisotzki, L., et al. 2024, Astronomy and Astrophysics, 684, A42

Kerutt, J., Wisotzki, L., Verhamme, A., et al. 2022, AA, 659, A183

Kneib, J.-P., Bonnet, H., Golse, G., et al. 2011, Astrophysics Source Code Library, ascl

Kneib, J.-P., Ellis, R. S., Smail, I., Couch, W., & Sharples, R. 1996, The Astrophysical Journal, 471, 643

Kneib, J.-P. & Natarajan, P. 2011, The Astronomy and Astrophysics Review, 19, 1

Kokorev, V., Brammer, G., Fujimoto, S., et al. 2022, Astrophysical Journal, Supplement, 263, 38

Kokorev, V., Fujimoto, S., Labbe, I., et al. 2023, Astrophysical Journal, Letters, 957, L7

Konno, A., Ouchi, M., Nakajima, K., et al. 2016, The Astrophysical Journal, 823, 20

Kroupa, P. 2001, Monthly Notices of the RAS, 322, 231

Kulkarni, G., Keating, L. C., Haehnelt, M. G., et al. 2019, Monthly Notices of the Royal Astronomical Society : Letters, 485, L24

Kusakabe, H., Blaizot, J., Garel, T., et al. 2020, Astronomy & Astrophysics, 638, A12

Lam, Bouwens, Rychard J., Labbé, Ivo, et al. 2019, AA, 627, A164

Lapi, A., Boco, L., Gandolfi, G., et al. 2024 [Arxiv :2403.07401v1]

Laporte, N., Ellis, R. S., Boone, F., et al. 2017, Astrophysical Journal, Letters, 837, L21

Laporte, N., Streblyanska, A., Kim, S., et al. 2015, Astronomy & Astrophysics, 575, A92

Laporte, N., Zitrin, A., Dole, H., et al. 2022, Astronomy & Astrophysics, 667, L3

Larson, R. L., Finkelstein, S. L., Hutchison, T. A., et al. 2022, The Astrophysical Journal, 930, 104

Le Fèvre, O., Béthermin, M., Faisst, A., et al. 2020, Astronomy and Astrophysics, 643, A1

Leclercq, F., Bacon, R., Wisotzki, L., et al. 2017, Astronomy & Astrophysics, 608, A8

Lee, S.-K., Ferguson, H. C., Somerville, R. S., Wiklind, T., & Giavalisco, M. 2010, The Astrophysical Journal, 725, 1644

Leitherer, C., Schaerer, D., Goldader, J. D., et al. 1999, The Astrophysical Journal Supplement Series, 123, 3

Lemaux, B. C., Fuller, S., Bradač, M., et al. 2021, Monthly Notices of the RAS, 504, 3662

Limousin, M., Richard, J., Jullo, E., et al. 2007, Astrophysical Journal, 668, 643

Lin, X., Cai, Z., Wu, Y., et al. 2024 [Arxiv :2401.09532v1]

Liu, Y., Dai, Y. S., Wuyts, S., Huang, J.-S., & Jiang, L. 2023a, arXiv e-prints, arXiv :2309.11559

Liu, Y., Jiang, L., Windhorst, R. A., Guo, Y., & Zheng, Z.-Y. 2023b, Astrophysical Journal, 958, 22

Livermore, R. C., Finkelstein, S. L., & Lotz, J. M. 2017, The Astrophysical Journal, 835, 113

Looser, T. J., D'Eugenio, F., Maiolino, R., et al. 2023, arXiv e-prints, arXiv :2306.02470

Lotz, J. e., Koekemoer, A., Coe, D., et al. 2017, The Astrophysical Journal, 837, 97

Lu, T.-Y., Goto, T., Hashimoto, T., et al. 2022, Monthly Notices of the Royal Astronomical Society, 517, 1264

Madau, P. & Dickinson, M. 2014, Annual Review of Astron and Astrophys, 52, 415

Madau, P. & Dickinson, M. 2014, Annual Review of Astronomy and Astrophysics, 52, 415–486

Madau, P., Haardt, F., & Rees, M. J. 1999, The Astrophysical Journal, 514, 648

Madau, P., Pozzetti, L., & Dickinson, M. 1998, Astrophysical Journal, 498, 106

Małek, K., Buat, V., Roehlly, Y., et al. 2018, Astronomy & Astrophysics, 620, A50

Maseda, M. V., Bacon, R., Franx, M., et al. 2018, Astrophysical Journal, Letters, 865, L1

Maseda, M. V., Bacon, R., Lam, D., et al. 2020a, Monthly Notices of the RAS, 493, 5120

Maseda, M. V., Bacon, R., Lam, D., et al. 2020b, Monthly Notices of the RAS, 493, 5120

Maseda, M. V., Lewis, Z., Matthee, J., et al. 2023, arXiv e-prints, arXiv :2304.08511

Mason, C. A., Fontana, A., Treu, T., et al. 2019, Monthly Notices of the Royal Astronomical Society, 485, 3947

Mason, C. A., Trenti, M., & Treu, T. 2023, Monthly Notices of the RAS, 521, 497

Mason, C. A., Treu, T., De Barros, S., et al. 2018a, The Astrophysical Journal Letters, 857, L11

Mason, C. A., Treu, T., Dijkstra, M., et al. 2018b, The Astrophysical Journal, 856, 2

Matthee, J., Mackenzie, R., Simcoe, R. A., et al. 2023, Astrophysical Journal, 950, 67

Matthee, J., Naidu, R. P., Pezzulli, G., et al. 2022, Monthly Notices of the Royal Astronomical Society, 512, 5960

Matthee, J., Sobral, D., Best, P., et al. 2016a, Monthly Notices of the Royal Astronomical Society, 465, 3637

Matthee, J., Sobral, D., Hayes, M., et al. 2021, Monthly Notices of the RAS, 505, 1382

Matthee, J., Sobral, D., Hayes, M., et al. 2021, Monthly Notices of the Royal Astronomical Society, 505, 1382

Matthee, J., Sobral, D., Oteo, I., et al. 2016b, Monthly Notices of the Royal Astronomical Society, 458, 449

Matthee, J., Sobral, D., Santos, S., et al. 2015, Monthly Notices of the RAS, 451, 400

Mauerhofer, V. & Dayal, P. 2023, Monthly Notices of the Royal Astronomical Society, 526, 2196

McGreer, I. D., Mesinger, A., & D'Odorico, V. 2015, Monthly Notices of the Royal Astronomical Society, 447, 499

Meneghetti, M., Natarajan, P., Coe, D., et al. 2017, Monthly Notices of the RAS, 472, 3177

Mercier, W., Epinat, B., Contini, T., et al. 2022, Astronomy & Astrophysics, 665, A54

Mingozzi, M., James, B. L., Arellano-Córdova, K. Z., et al. 2022, Astrophysical Journal, 939, 110

Mingozzi, M., James, B. L., Berg, D. A., et al. 2024, Astrophysical Journal, 962, 95

Mitchell, P. D., Blaizot, J., Cadiou, C., et al. 2021, Monthly Notices of the RAS, 501, 5757

Morishita, T., Roberts-Borsani, G., Treu, T., et al. 2023, The Astrophysical Journal Letters, 947, L24

Morishita, T., Stiavelli, M., Grillo, C., et al. 2024 [Arxiv :2402.14084v1]

Nagao, T., Maiolino, R., & Marconi, A. 2006, Astronomy & Astrophysics, 459, 85

Naidu, R. P., Oesch, P. A., van Dokkum, P., et al. 2022, Astrophysical Journal, Letters, 940, L14

Naidu, R. P., Tacchella, S., Mason, C. A., et al. 2020, The Astrophysical Journal, 892, 109

Nakane, M., Ouchi, M., Nakajima, K., et al. 2023 [Arxiv :2312.06804v1]

Nanayakkara, T., Glazebrook, K., Jacobs, C., et al. 2023, Astrophysical Journal, Letters, 947, L26

Napolitano, L., Pentericci, L., Santini, P., et al. 2024 [Arxiv :2402.11220v1]

Nasir, F. & D'Aloisio, A. 2020, Monthly Notices of the Royal Astronomical Society, 494, 3080

Ocvirk, P., Aubert, D., Sorce, J. G., et al. 2020, Monthly Notices of the RAS, 496, 4087

Oesch, P., Van Dokkum, P., Illingworth, G., et al. 2015, The Astrophysical Journal Letters, 804, L30

Oh, K., Sarzi, M., Schawinski, K., & Sukyoung, K. Y. 2011, The Astrophysical Journal Supplement Series, 195, 13

Osterbrock, D. E. 1989, Astrophysics of gaseous nebulae and active galactic nuclei

Osterbrock, D. E. & Ferland, G. J. 2006, Astrophysics Of Gas Nebulae and Active Galactic Nuclei (University science books)

Ouchi, M., Ono, Y., & Shibuya, T. 2020, Annual Review of Astronomy and Astrophysics, 58, 617

Ouchi, M., Shimasaku, K., Akiyama, M., et al. 2008, Astrophysical Journal, Supplement, 176, 301

Ouchi, M., Shimasaku, K., Okamura, S., et al. 2004, The Astrophysical Journal, 611, 660

Pahl, A. J., Shapley, A. E., Steidel, C. C., et al. 2024 [Arxiv :2401.09526v1]

Parsa, S., Dunlop, J. S., McLure, R. J., & Mortlock, A. 2016, Monthly Notices of the RAS, 456, 3194

Partridge, R. B. & Peebles, P. J. E. 1967, Astrophysical Journal, 148, 377

Pello-Descayre, R., Soucail, G., Sanahuja, B., Mathez, G., & Ojero, E. 1988, Astronomy and Astrophysics, 190, L11

Pentericci, L., Fontana, A., Vanzella, E., et al. 2011, The Astrophysical Journal, 743, 132

Pentericci, L., Vanzella, E., Castellano, M., et al. 2018, Astronomy & Astrophysics, 619, A147

Piqueras, L., Conseil, S., Shepherd, M., et al. 2019, ASP Conf. Ser. Vol. 521, Astronomical Data Analysis Software and Systems XXVI

Planck Collaboration, Ade, P. A. R., Aghanim, N., et al. 2016, Astronomy and Astrophysics, 594, A13

Planck Collaboration, Aghanim, N., Akrami, Y., et al. 2020, A&A, 641, A6

Popesso, P., Concas, A., Cresci, G., et al. 2023, Monthly Notices of the Royal Astronomical Society, 519, 1526

Postman, M., Coe, D., Benítez, N., et al. 2012, Astrophysical Journal, Supplement, 199, 25

Pozzetti, L., Bolzonella, M., Zucca, E., et al. 2010, Astronomy & Astrophysics, 523, A13

Qin, Y., Mesinger, A., Bosman, S. E., & Viel, M. 2021, Monthly Notices of the Royal Astronomical Society, 506, 2390

Reddy, N. A., Oesch, P. A., Bouwens, R. J., et al. 2018, The Astrophysical Journal, 853, 56

Reddy, N. A., Steidel, C. C., Pettini, M., et al. 2008, Astrophysical Journal, Supplement, 175, 48

Reuter, C., Vieira, J. D., Spilker, J. S., et al. 2020, Astrophysical Journal, 902, 78

Richard, J., Claeyssens, A., Lagattuta, D., et al. 2021, Astronomy & Astrophysics, 646, A83

Richard, J., Patricio, V., Martinez, J., et al. 2015, Monthly Notices of the RAS, 446, L16

Roberts-Borsani, G., Treu, T., Shapley, A., et al. 2024 [Arxiv :2403.07103v1]

Robertson, B., Tacchella, S., Johnson, B., et al. 2023, Nature Astronomy, 7, 611

Robertson, B. E., Furlanetto, S. R., Schneider, E., et al. 2013, The Astrophysical Journal, 768, 71

Rosdahl, J. & Blaizot, J. 2012, Monthly Notices of the RAS, 423, 344

Rosdahl, J., Blaizot, J., Katz, H., et al. 2022, Monthly Notices of the Royal Astronomical Society, 515, 2386–2414

Runnholm, A., Gronke, M., & Hayes, M. 2021, Publications of the ASP, 133, 034507

Runnholm, A., Hayes, M., Melinder, J., et al. 2020, Astrophysical Journal, 892, 48

Salpeter, E. E. 1955, The Astrophysical Journal, 121, 161

Santini, P., Fontana, A., Castellano, M., et al. 2017, The Astrophysical Journal, 847, 76

Santini, P., Fontana, A., Castellano, M., et al. 2023, The Astrophysical Journal Letters, 942, L27

Santini, P., Fontana, A., Grazian, A., et al. 2009, Astronomy & Astrophysics, 504, 751

Santos, S., Sobral, D., Butterworth, J., et al. 2021, Monthly Notices of the Royal Astronomical Society, 505, 1117

Santos, S., Sobral, D., Matthee, J., et al. 2020a, Monthly Notices of the Royal Astronomical Society, 493, 141

Santos, S., Sobral, D., Matthee, J., et al. 2020b, Monthly Notices of the Royal Astronomical Society, 493, 141

Saxena, A., Bunker, A. J., Jones, G. C., et al. 2024, JADES : The production and escape of ionizing photons from faint Lyman-alpha emitters in the epoch of reionization

Saxena, A., Robertson, B. E., Bunker, A. J., et al. 2023, Astronomy & Astrophysics, 678, A68

Scaramella, R., Amiaux, J., Mellier, Y., et al. 2022, Astronomy & Astrophysics, 662, A112

Schaerer, D. 2000, in Building Galaxies ; from the Primordial Universe to the Present, ed. F. Hammer, T. X. Thuan, V. Cayatte, B. Guiderdoni, & J. T. Thanh Van, 389

Schaerer, D. 2007, Highlights of Astronomy, 14, 211

Schaerer, D. & de Barros, S. 2010, Astronomy and Astrophysics, 515, A73

Schaerer, D., de Barros, S., & Stark, D. P. 2011, Astronomy & Astrophysics, 536, A72

Schaerer, D., Marques-Chaves, R., Barrufet, L., et al. 2022, Astronomy and Astrophysics, 665, L4

Schaerer, D. & Pelló, R. 2002, Astrophysics and Space Science, 281, 475

Schenker, M. A., Ellis, R. S., Konidaris, N. P., & Stark, D. P. 2014, The Astrophysical Journal, 795, 20

Schneider, P., Ehlers, J., & Falco, E. E. 1992, Derivation of the lens equation (Berlin, Heidelberg : Springer Berlin Heidelberg), 119–155

Shibuya, T., Ouchi, M., Nakajima, K., et al. 2014, Astrophysical Journal, 785, 64

Shipley, H. V., Lange-Vagle, D., Marchesini, D., et al. 2018, The Astrophysical Journal Supplement Series, 235, 14

Shivaei, I., Alberts, S., Florian, M., et al. 2024, arXiv e-prints, arXiv :2402.07989

Simmonds, C., Tacchella, S., Maseda, M., et al. 2023, Monthly Notices of the Royal Astronomical Society, 523, 5468–5486

Smith, A., Kannan, R., Garaldi, E., et al. 2022, Monthly Notices of the Royal Astronomical Society, 512, 3243

Sobral, D., Best, P. N., Smail, I., et al. 2014, Monthly Notices of the Royal Astronomical Society, 437, 3516

Sobral, D. & Matthee, J. 2019, Astronomy & Astrophysics, 623, A157

Sobral, D., Matthee, J., Best, P., et al. 2017, Monthly Notices of the Royal Astronomical Society, 466, 1242

Sobral, D., Santos, S., Matthee, J., et al. 2018, Monthly Notices of the Royal Astronomical Society, 476, 4725

Song, M., Finkelstein, S. L., Gebhardt, K., et al. 2014, The Astrophysical Journal, 791, 3

Soucail, G., Fort, B., Mellier, Y., & Picat, J. P. 1987, Astronomy and Astrophysics, 172, L14

Soucail, G., Mellier, Y., Fort, B., Mathez, G., & Cailloux, M. 1988, Astronomy and Astrophysics, 191, L19

Speagle, J. S., Steinhardt, C. L., Capak, P. L., & Silverman, J. D. 2014, The Astrophysical Journal Supplement Series, 214, 15

Spergel, D., Gehrels, N., Baltay, C., et al. 2015, arXiv e-prints, arXiv :1503.03757

Spina, B., Bosman, S. E. I., Davies, F. B., Gaikwad, P., & Zhu, Y. 2024 [Arxiv :2405.12273v1]

Stark, D. P., Ellis, R. S., Charlot, S., et al. 2017, Monthly Notices of the Royal Astronomical Society, 464, 469

Stark, D. P., Ellis, R. S., Chiu, K., Ouchi, M., & Bunker, A. 2010, Monthly Notices of the Royal Astronomical Society, 408, 1628

Stark, D. P., Ellis, R. S., & Ouchi, M. 2011, The Astrophysical Journal Letters, 728, L2

Steinhardt, C. L., Speagle, J. S., Capak, P., et al. 2014, The Astrophysical journal letters, 791, L25

Tang, M., Stark, D. P., Chen, Z., et al. 2023, Monthly Notices of the RAS, 526, 1657

Tang, M., Stark, D. P., Ellis, R. S., et al. 2024, arXiv e-prints, arXiv :2402.06070

Thai, T. T., Tuan-Anh, P., Pello, R., et al. 2023, Astronomy & Astrophysics, 678, A139

Theulé, P., Burgarella, D., Buat, V., et al. 2024, Astronomy and Astrophysics, 682, A119

Topping, M. W., Stark, D. P., Endsley, R., et al. 2022, Astrophysical Journal, 941, 153

Trainor, R. F., Strom, A. L., Steidel, C. C., & Rudie, G. C. 2016, The Astrophysical Journal, 832, 171

Treu, T., Roberts-Borsani, G., Bradac, M., et al. 2022, The Astrophysical Journal, 935, 110

Treu, T., Schmidt, K., Brammer, G., et al. 2015, The Astrophysical Journal, 812, 114

Valentino, F., Fujimoto, S., Gimnez-Arteaga, C., et al. 2024 [Arxiv :2402.17845v1]

Vanni, I., Salvadori, S., & Skúladóttir, Á. 2023, in Memorie della Societa Astronomica Italiana, Vol. 94, 84

Vanzella, E., Loiacono, F., Bergamini, P., et al. 2023, Astronomy and Astrophysics, 678, A173

Verhamme, A., Dubois, Y., Blaizot, J., et al. 2012, Astronomy and Astrophysics, 546, A111

Verhamme, A., Orlitová, I., Schaerer, D., & Hayes, M. 2015, Astronomy and Astrophysics, 578, A7

Verhamme, A., Orlitová, I., Schaerer, D., et al. 2017, Astronomy and Astrophysics, 597, A13

Verhamme, A., Schaerer, D., Atek, H., & Tapken, C. 2008, Astronomy & Astrophysics, 491, 89

Verhamme, A., Schaerer, D., & Maselli, A. 2006, Astronomy and Astrophysics, 460, 397

Wang, T., Sun, H., Zhou, L., et al. 2024 [Arxiv :2403.02399v1]

Weaver, J. R., Cutler, S. E., Pan, R., et al. 2023, arXiv preprint arXiv :2301.02671

Weilbacher, P. M., Palsa, R., Streicher, O., et al. 2020, Astronomy & Astrophysics, 641, A28

Welch, B., Coe, D., Diego, J. M., et al. 2022, Nature, 603, 815

Whitaker, K. E., Pope, A., Cybulski, R., et al. 2017, The Astrophysical Journal, 850, 208

Whitler, L., Endsley, R., Stark, D. P., et al. 2023a, Monthly Notices of the RAS, 519, 157

Whitler, L., Stark, D. P., Endsley, R., et al. 2023b, arXiv e-prints, arXiv :2305.16670

Wilkins, S. M., Bunker, A., Coulton, W., et al. 2013, Monthly Notices of the Royal Astronomical Society, 430, 2885

Wisotzki, L., Bacon, R., Blaizot, J., et al. 2016, Astronomy & Astrophysics, 587, A98

Witstok, J., Maiolino, R., Smit, R., et al. 2024 [Arxiv :2404.05724v1]

Witstok, J., Smit, R., Saxena, A., et al. 2023 [Arxiv :2306.04627v3]

Witten, C., Laporte, N., Martin-Alvarez, S., et al. 2023 [Arxiv :2303.16225v1]

Yang, H., Malhotra, S., Gronke, M., et al. 2017, The Astrophysical Journal, 844, 171

Yuan, Y., Martin-Alvarez, S., Haehnelt, M. G., Garel, T., & Sijacki, D. 2024 [Arxiv :2401.02572v1]

Zackrisson, E., Hultquist, A., Kordt, A., et al. 2023 [Arxiv :2312.09289v1]

Zahid, H. J., Dima, G. I., Kewley, L. J., Erb, D. K., & Davé, R. 2012, Astrophysical Journal, 757, 54

Zahid, H. J., Yates, R. M., Kewley, L. J., & Kudritzki, R.-P. 2013, The Astrophysical Journal, 763, 92

Zheng, Z., Cen, R., Trac, H., & Miralda-Escudé, J. 2010, The Astrophysical Journal, 716, 574

Zheng, Z.-Y., Finkelstein, S. L., Finkelstein, K., et al. 2013, Monthly Notices of the Royal Astronomical Society, 431, 3589

Zhu, Y., Becker, G. D., Bosman, S. E., et al. 2022, The Astrophysical Journal, 932, 76

Zhu, Y., Becker, G. D., Bosman, S. E. I., et al. 2024 [Arxiv :2405.12275v1]

Zimmerman, D. T., Narayanan, D., Whitaker, K. E., & Davè, R. 2024 [Arxiv :2401.06719v1]

Acknowledgements

There are many people to thank for playing a part in this journey, too many to enumerate a full list, let alone give them all their due. I will attempt to condense into a few paragraphs the most important actors and what their contribution has meant to me.
Firstly, my supervisor Roser Pello, who believed in me when I was a 22-year-old masters student and there wasn't really any reason to do so. You brought me to one of the most exciting fields of astrophysics and guided me with patience, understanding and insight. Your door was always open to me, despite your many duties and busy schedule, for which I can't thank you enough. My PhD experience would have been much poorer without it. You gave me all the tools I needed for a successful PhD and, at the same time, made sure I kept my sanity. If I have a successful career in astronomy it will have been because of you.
I would also like to thank the wider LAM community, the GECO team members, particularly those with whom I had productive discussions and who helped guide me throughout my three years in Marseille. Nicolas Laporte, for many exciting ideas, projects and for always being ready to talk about science. Mat Pieri for many fascinating discussions and weekly football ; it remains a shame that you're a Spurs fan. Denis Burgarella for the advice and help with several of my projects. Tuan-Anh for all your support, interest and ideas during our many projects with MUSE. The support staff at the LAM are also due a big thank you, particularly Mme Maxant, without whom I would have been able to do very little. I hope I didn't try your patience too much.
I'm grateful to my collaborators within the MUSE collaboration, particularly Johan and Adélaïde, for all your help throughout the thesis, but also to Jarle, Jorryt, Leindert and many others for helpful comments and interesting discussions. Lastly, thank you to my thesis jury, for making time to hear about, and even read, my work, and asking thought-provoking questions.
I also owe a great deal to my peers : the other PhDs and postdocs at the LAM as well as those I met on my travels. There are too many names but I will take some time, attempting to think of all of them as a measure of gratitude for enriching my PhD experience : Elena, Alessandro, Simone, Wilfried, JC, Gayathri, Diana, Isabelle, Pia, Michael, Mathilde, Thai, Yohana, Ivanna, Natalie, Viola, Lisa, Mahawa, Callum, Cristian, Nicola, Duarte, Raphael. As you can see from this long list I have been fortunate enough to meet a great many remarkable people. Several among them are due their own thank yous, and hold a special place in my memory of these three years. Meriam, you were the first to make me feel welcome in Marseille and, together with Camille, helped me through the tricky first months of administration and settling in, both turning into amazing friends and people I always loved to spend time with. We had our ups and downs but now, writing this after leaving, I only remember the good. Alexis, Sia, Melanie, a particular thanks must go to you for the many good times we spent together. I'm hoping there are many more to come. Finally the

boys require a special thank you, Juan, who I will always maintain is the best Colombian footballer this side of Bogotá. Martin, thank you for three years spent side-by-side in the trenches, I haven't met many people who can make me laugh like you. Paolo, it occurs to me that as we were in the same office and lived in the same building, we were rarely more than thirty meters from each other for two years. Thanks for being a great office-mate, and for the football, volleyball and the carbonara.
I have to mention a few friends from "home" too, as they always welcomed me back with open arms, no matter how long I stayed away. The Mill Lane girls : Grace, Gemma, Marie, Hayley, I hope you know how much I enjoyed visiting you and seeing you in France. The boys, Charlie B, Charlie D, Hamish, Ed, Sid, Alec and more of my extended London family, Kitty, Viola, Mish and Alex, who deserves his own mention, both because I know it will please him and because any time we spent together was always special. If I've forgotten you, please send me an angry message but be prepared to answer questions about the thesis to prove you've read all the way through it to get to here.
To all of you, I must apologise for leaving once again, but such is my curse : I live somewhere amazing, meet amazing people, have an amazing time and then have to give it all up. Believe me I wish it were different.
Finally it remains to express my gratitude to my family : mum, dad and my sister Noa. Dad you've supported me for my whole life, through all my studies, through all the difficult times, all the moves and all the choices I've made. It was no different during the PhD, I always knew I could count on you for anything I needed. Thanks also for the many visits, I hope I showed you the best of Marseille.
Mum, I know I haven't always made it easy on you, and I know sometimes you must have despaired of my choices. But you always made me feel free to make my own choices and take my own path and the importance of that cannot be overstated.
Noa, I'm constantly inspired by you and your bravery, and can only hope to travel as much as you do. Everyone I've spoken to about you is very upset you're so far away and they can't meet you. I, however, am glad because they might realise you're the real achiever in the family. I hope, maybe one day, you can come to terms with the fact that you're adopted.
There's one more person to thank, which is easy for me to admit but difficult for me to elucidate. But she knows who she is and what she did, and that's enough.